Paleomagnetism of Late Paleozoic Basins of the Moroccan Meseta and the Western High Atlas: The Intra-Pangean Megashear Zone and the Paleogeography of Pangea

Vinzenz Maximilian Weissbrodt

München 2024

Paleomagnetism of Late Paleozoic Basins of the Moroccan Meseta and the Western High Atlas: The Intra-Pangean Megashear Zone and the Paleogeography of Pangea

Vinzenz Maximilian Weissbrodt

Dissertation

zur Erlangung des Doktorgrades

an der Fakultät für Geowissenschaften der

Ludwig-Maximilians-Universität München

vorgelegt von

Vinzenz Maximilian Weissbrodt

aus München

München, den 06.05.2024

Erstgutachter: Prof. Dr. Valerian Bachtadse

Zweitgutachter: Dr. Uwe Kirscher

Tag der mündlichen Prüfung: 25.10.2024

Preamble

This thesis is a monograph summarizing my doctoral work on the paleomagnetism of late Paleozoic igneous and sedimentary rocks of Morocco and its paleogeographic implications. It is written in American English (AE). Chapter 1 summarizes and discusses the paleomagnetic results of the sampling areas of Oued Zat (ZAT) from the Western High Atlas, Koudiat El Hamra-Haiane from the Jebilet massif (JEB), M'Tal (MTA), Nzalt-Lararcha (NL) and Mechraa Ben Abbou (MEC) from the Rehamna Massif and ultimately Chougrane (CHO), El Had Bouhssoussene (BOUH), Khenifra (KHE), Tiddas-Souk Es-Sebt des Ait Ikko (Tsesdai) – in short Tiddas (TID) and Bou Achouch (BOUA) from the Central Massif which has been accepted for publication in 'Earth-Science Reviews'.

V. Weissbrodt, V. Bachtadse, U. Kirscher, H. Saber, Y. Liu and A. Ronchi. Tectonic Imprints in Permian Paleomagnetic Data of Morocco. *Earth-Science Reviews*, Manuscript number: EARTH-D-23-00523.

Chapter 1 represents the manuscript in its accepted form, with the supplementary figures and tables incorporated into the main text for a better readability.

In chapter 2, unpublished paleomagnetic data of the Moroccan field campaigns in the sampling areas of Argana (ARG), Souss (ZIKI and ZAL), Ourika (OUR), Sebt Brikiyne (BRI), Zaer (ZAE), Sidi Kassem (KASS) and Bouterhella (BOUT) are presented together with a short geological summary and age model for each basin. The chapter closes with a brief rock magnetic analysis of the unpublished basins.

Furthermore, data of the anisotropy of magnetic susceptibility (AMS) from BRI, NL, MEC, BOUH, CHO, KHE, TID, BOUT and BOUA is condensed in chapter 3 to complement the estimations of the paleohorizontal in the field.

Finally, chapter 4 merges the findings of previous chapters and puts them in a common frame.

Summary

When reconstructing tectonic plates since the Mesozoic, a central cornerstone within the Earth sciences community has always been the agreement on the classical Wegenerian shape, from which Pangea dispersed into the present-day configuration of continents. The configuration of Pangea in the late Paleozoic, however, has been controversial. The small number and low quality of paleomagnetic data for the late Paleozoic resulted in a significant overlap between Gondwana and Laurasia when keeping the conventional Wegenerian (Pangea A) reconstruction. In the alternative (Pangea B) model Gondwana is positioned some 3000 km further to the east overcoming the problem of continental overlap. However, in order to achieve the Pangea dispersion starting in the Jurassic, a dextral (mega-) shear zone located in the Mediterranean is required to transfer from Pangea B to A.

In such a shear-zone, vertical axis rotations may be the only quantitative means to clarify its still controversial timing and position and act as supportive evidence of Pangea B in addition to existing paleomagnetic, paleoclimatological, paleontological and geochemical arguments. Proponents of Pangea B have complemented the sparse Permian paleomagnetic data set of Gondwana with data from Adria treating Adria as a tectonically coherent African promontory. On the other hand, it has been argued that the overlap might be an artifact caused by inclination shallowing. Thus, the validity of Pangea A or Pangea B decisively depends on selection and filtering criteria making new high-quality late Carboniferous - early Permian data from Gondwana as well as identification of larger patterns of vertical axis rotations for the same time interval indispensable for a substantial progress in the Pangea debate.

In order to contribute to this debate, late Paleozoic continental sediments and well dated intrusive and extrusive rocks of the Moroccan Meseta and Western High Atlas in NW-Africa have been studied paleomagnetically. In total, fifteen late Paleozoic basins and two late Hercynian plutonic massifs were studied and 944 paleomagnetic samples were collected at 152 sites, with age constraints based on absolute and relative dating using geochronological, paleontological and stratigraphical arguments. Rock magnetic studies suggest predominantly magnetite and hematite in various proportions as main carriers of the paleomagnetic signal in the igneous samples whereas hematite is prevalent in the sedimentary samples. Moreover, maghemite is observed within strongly weathered sites.

For five basins, no primary high-stability paleomagnetic component could be determined, potentially due to viscous overprinting by the recent geomagnetic field caused by chemical alteration of the magnetic mineralogy or by an IRM imparted by lightning strikes. Difficult drilling conditions at the two late Hercynian (~ 270 – 280 Ma) massifs restricted the acquisition to a small data set only with preliminary but promising results. Moreover, one basin is interpreted to be pervasively remagnetized in the late Permian as revealed by negative bulk and inclination-only fold tests as well as calculated paleolatitudes.

At the residual basins, positive inclination-only fold tests support the primary character of magnetization, which is also underpinned by the identification of three reversals recorded at the basins of M'Tal, Chougrane and Souk El Had Bouhsoussene, tentatively related to the late-Artinskian CI2n normal magnetochron (281.24 ± 2.3 Ma). A high-stability component of characteristic remanent magnetization could be identified in 76% of the remaining samples with site-mean declinations frequently distributed along a small circle girdle within respective basins. The magnetization is therefore interpreted as syndepositional and rotational movements are argued to have happened concurrently with sedimentation/intrusion in the early Permian.

Resulting VGPs are elongated along a NE-SW trending small circle swath intersecting the late Paleozoic segment of the Gondwanan APWP with a rotation pole located in the sampling area suggesting the presence of vertical axis rotations within the Meseta block which might be related to intra-Pangea shearing. The resulting paleolatitudes yield a position of the Meseta block close to the paleo-equator at ~ 280 Ma irrespective of the underlying lithology (inclination shallowing-resistant volcanics or inclination shallowing-prone sediments) thus widely excluding the influence of inclination shallowing. Comparing data from this study with a combined reference data set of Adria and Gondwana does not support the coherence of Adria and Gondwana. An early Permian Pangea reconstruction based on the data achieved in this study does not result in a significant continental overlap and does not require alternative reconstructions such as Pangea B.

Table of Contents

List of Figures

List of Tables

1 Tectonic Imprints in Permian Paleomagnetic Data of Morocco

*By **V. Weissbrodt, V. Bachtadse, U. Kirscher, H. Saber, Y. Liu and A. Ronchi** accepted for publication in* Earth-Science Reviews.

Abstract

Although Pangea as Earth's youngest supercontinent has continuously served as a pivotal reference mark in paleogeographic reconstructions, its assembly is still a matter of debate. This is mainly due to poor paleomagnetic data coverage for Permian times for Africa, the core element of Pangea. Paleomagnetic data for Adria, thought to be the African promontory in the Permian, yield paleolatitudes which when compared to the European data set result in a significant continental overlap and seem to confirm the original Pangea B concept of Irving (1977). In order to improve the paleomagnetic data base for Africa, volcanic and sedimentary rocks were sampled in the Permo-Carboniferous basins of Morocco yielding a total of 97 sites and 615 samples. Rock magnetic studies are diagnostic for magnetite and hematite in various proportions as main carriers of the paleomagnetic signal. After the removal of low and intermediate coercivity/blocking temperature components a characteristic component of magnetization pointing to the SE with declinations strung out along a small circle from 107° to 182° and with inclinations around -7° after tectonic correction was identified in 76% of the samples. In nine out of the ten basins studied, positive inclination only fold tests support the primary character of magnetization. Furthermore, three reversals were identified at the basins of M'Tal, Chougrane and Souk El Had Bouhsoussene lending further support to our interpretation. VGPs are distributed along a NE-SW trending small circle band intersecting the late Paleozoic segment of the Gondwana APWP with a rotation pole located in the sampling area. The resulting paleolatitudes yield a position of the Meseta block close to the paleo-equator at ~280 Ma. The widespread presence of vertical axis rotations in the Meseta basins on the other hand, could be related to proposed intra-Pangea shear zones and would provide additional constraints on the extent of such shear zones towards the northern margin of Gondwana. However, tectonic models based on vertical axis rotations in this region need to be treated with caution, since the timing of these rotations remains ambiguous with the current data set. Using our paleomagnetic data from the Meseta block as a representative for Gondwana, a large latitudinal overlap between Gondwana and Laurussia is not required.

1.1 Introduction

Since the identification of Pangea, the importance of supercontinents for the geosphere and biosphere in Earth evolution gained increasing attention (Mitchell et al., 2021). As the most recent and therefore likely to be the best understood supercontinent, Pangea plays a key role as a reference point in plate tectonic modelling for post Paleozoic times. However, its geometry and geodynamic evolution are continuously debated and details of its paleogeography for late Paleozoic times are not yet completely agreed on (Channell et al., 2022; Pastor-Galán, 2022; Wu et al., 2021).

While Pangea's break-up process from Jurassic times onward has mostly been deciphered using the large paleomagnetic data set and seafloor data, its paleogeographic evolution remains ambiguous for prior times (e.g., Aubele et al., 2012; Edel et al., 2018; Muttoni et al., 2003; Pohl et al., 2018). High-quality data for the late Paleozoic – especially from Gondwana – is still scarce leading to substantial uncertainties in paleogeographic reconstructions. These uncertainties led some authors to argue for a substantial latitudinal overlap of Laurasia and Gondwana when keeping the general continental assemblage in a conventional Wegenerian or Pangea A configuration for the early Permian (Muttoni et al., 2003; Muttoni et al., 2009). To avoid this misfit Irving (1977) as well as Morel and Irving (1981) introduced an alternative configuration labelled Pangea B. Here, Gondwana is shifted approximately 3000 km to the east with respect to the northern continents (Laurasia) along a constant line of latitude. In order to accomplish the transition of the assumed Pangea B model to the widely approved Pangea A model an early Permian diffuse dextral shear zone was introduced which was located in the Mediterranean and has been related to structural vertical axis rotations of pre-late Permian tectonic blocks (Aubele et al., 2012; Aubele et al., 2014; Bachtadse et al., 2018; Kent and Muttoni, 2020; Muttoni and Kent, 2019) (see next chapter for more details on the Pangea debate).

Since conclusive evidence is still lacking, a variety of explanations for the validity of Pangea B have been controversially discussed (see review and references in Domeier et al. (2012)). Among them, complementing the sparse Permian paleomagnetic information of Gondwana with data from Adria, i.e. treating Adria as a tectonically coherent African promontory, has on the one hand turned out to be one of the main arguments for the presence of the latitudinal misfit, but on the other hand has been criticized in lacking legitimacy (an comprehensive historical treatment is provided by Muttoni and Kent (2019)). Domeier et al. (2021) tackled this procedure by highlighting relative motions between Adria and Africa due

to the opening of the Ionian basin and criticized biasing effects on African paleolatitudes towards higher values (thus favoring Pangea B) when utilizing the relatively high amount of data from Adria as a proxy for Gondwana. Furthermore, their early Permian paleogeographic reconstruction based on Moroccan (i.e. NW African) volcanics showed no latitudinal misfit. In response, Channell et al. (2022) propose a kinematic model that reconciliates Mediterranean tectonism with its effect on paleomagnetic data from Adria shifting Africa towards the north. They further indicate that, due to the general paucity of available data, the validity of Pangea A or Pangea B critically hinges on selection and filtering criteria. Domeier et al. (2012) suppose that especially inclination shallowing-prone sediments from the scarce Gondwanan data set might be responsible for the overlap and that applying a blanket flattening correction factor f of 0.6 (Tauxe, 2005) largely resolves the latitudinal misfit. However, this leads to a significant increase in the scatter of the sedimentary data set and reduces the consistency with data from coeval volcanic rocks (Channell et al., 2022). Hence, obtaining additional high-quality early Permian data from Gondwana becomes indispensable for a substantial progress in the Pangea debate and reconstruction of late Paleozoic paleogeography.

In this context, the Moroccan Meseta (MM) in NW-Africa fits the requirements to play a key role in unravelling the paleogeographic position of the northern margin of Gondwana – and because the relationship of the MM and Africa is much better constrained and minor in its extend compared to the Adria-Africa relationship, also for Gondwana itself – during the late Carboniferous and early Permian and to complement the poor late Paleozoic data set. After the publication of the pioneer studies of Daly and Pozzi (1976), Martin et al. (1978) and Westphal et al. (1979), it took more than four decades until Domeier et al. (2021) presented new paleomagnetic as well as geochronological data providing additional information to determine the early Permian position of Gondwana. They presented a comparably low number of sites (20) from six basins and found some conspicuous features within their results, such as syn-folding or inconclusive (inclination-only) fold tests or NE-SW elongate girdling of the Virtual Geomagnetic Poles (VGPs). The authors explain the syn-folding maximum clustering with either a primary magnetization that was affected by minor tectonic complexities or an actual remagnetized signal related to the terminal phase of the Variscan orogeny at ~275 Ma, which caused the minor tilting in this region. The potential influence of vertical axis rotations is interpreted to have been partially averaged out in the overall magnetic direction but ultimately the authors cannot provide an unambiguous interpretation due to their small data set (Domeier et al., 2021).

In this study, we present a review of the paleomagnetic results presented in the literature for the Moroccan Meseta block incorporating newly collected 615 samples from 97 sites in ten basins representing a combination of red sediments and intercalated volcanic flows allowing for the identification of tectonic attitudes of the volcanic rocks as well as direct testing of inclination shallowing in the sediments. We base the new results on the most recent age estimates using radiometric dating, paleontology and stratigraphy (Domeier et al., 2021) and georeferenced our samples in order to correlate them with given geological and geochronological constraints (Figs. 1.4 – 1.12, Tables 1.1 – 1.10).

1.2 The Pangea Debate

Since the landmark papers of Irving and Morel (1978), Morel and Irving (1981) and Morel et al. (1981) in the late seventies and early eighties, a vivid debate has been triggered, which is still ongoing these days (Channell et al., 2022; Domeier et al., 2021; Irving, 2013; Kent and Muttoni, 2020; Muttoni et al., 2003; Muttoni et al., 2013). Irving (1977) recognized that reconstructing a Permian Pangea in a Wegenerian (Pangea A) constellation and using paleomagnetic data to determine the paleolatitudes of Laurentia's southern and Gondwana's northern margin resulted in a significant overlap of both continents. This overlap can be resolved by shifting Gondwana some 3000 km to the east, thus positioning northwest Africa directly opposite the Donetsk basin (Morel et al., 1981), but simultaneously maintaining its paleolatitude. Since paleolongitudes are undefined using conventional paleomagnetic data, this approach would not violate any principle of paleomagnetic reconstructions. The resulting reconstruction (Pangea B), however, created new problems:

There is no doubt that the opening of the Atlantic Ocean started from within a Pangea A configuration, thus requiring a mega-shear zone, along which Gondwana moved some 3000 km to the west sometimes between the early Permian and the Early Jurassic. The formation of Permian rift basins such as the Oslo-Polish and the eastern Mediterranean basins, as well as the intramontane basins in central Europe, Greenland, northern Africa and northeastern America, can be linked to a right lateral shear zone connecting the Urals and Appalachians as originally proposed by Van Hilten (1964) and subsequently revived by Arthaud and Matte (1977). However, despite the evidence for oblique collision between Gondwana and North America (Becker et al., 2005) the existence of this mega-shear zone, the main prerequisite for any Pangea B type configuration, is still controversial. Despite the paleomagnetic arguments (Muttoni et al., 2003; Torcq et al., 1997) and additional paleoclimatological (Fluteau et al., 2001; Kent and

Muttoni, 2020), paleontological (Silantiev et al., 2022; Vai, 2003) as well as geochemical (Becker et al., 2005) evidence for the realistic possibility of Pangea B configurations, the strongest opposition arises from within the paleomagnetic community itself.

The main arguments being that the continental misfit between Laurentia and Gondwana is an artifact caused by (a) long living quadru- and octupole elements of the Earth's magnetic field (Van der Voo and Torsvik, 2001), (b) incorrect dating and/or correlating Permian rocks from both continents (Rochette and Vandamme, 2001) or (c) inclination shallowing (Domeier et al., 2012), a process affecting the orientation of magnetic minerals during compaction (King, 1955) of the sediment, not uncommon in continental red beds (Kirscher et al., 2014; Tauxe and Badgley, 1984), which form a significant part of the Permian paleomagnetic database for Gondwana and Laurentia. Whereas at least (a) has been discounted recently (Domeier et al., 2012; Evans et al., 2014), (b) and (c) are still options, whereby (c) is the option currently preferred by the majority of the paleomagnetic community. Based on this rationale Domeier et al. (2012) published a set of apparent polar wanders paths (APWP) and paleogeographic reconstructions for Gondwana and Laurentia. Accounting for inclination shallowing, Domeier et al. (2012) applied a blanket flattening factor (Tauxe and Kent, 2004) of f = 0.6 on all paleomagnetic data based on sedimentary rocks, irrespectively whether these rocks were of marine or continental origin, clastic or chemical sediments and thereby eliminating the continental overlap. Whether the application of a blanket correction for inclination shallowing is correct remains a matter of debate. Especially questionable is the basic assumption made by Domeier et al. (2012) that all sediments suffer the same amount of flattening. In fact, it has been demonstrated that inclination shallowing in sedimentary rocks of various ages and different lithologies can actually range from no shallowing (f = 1.0) at all to rather severe shallowing (f = 0.4) where no systematic correlation between rock type and degree of shallowing is observable (Kodama, 2012, pages 54 and 62). It is also noteworthy that Muttoni et al. (2013), by limiting their data selection to volcanic rocks of early Permian age from Africa and the southern Alps and thereby circumventing the problem of inclination shallowing could show that the continental misfit might be real and therefore argue in favor of Pangea B models.

Recently published paleomagnetic results for Permian rocks of Sardinia (Aubele et al., 2012; Aubele et al., 2014; Bachtadse et al., 2018) agree with the existence of an intra-Pangean shear zone which is characterized by complex and differential clockwise (CW) as well as counterclockwise (CCW) block rotations that may have largely occurred during the early Permian, certainly prior to the Jurassic (Kirscher et al., 2011). These rotations have tentatively

been assigned to represent shear stresses caused by a large intra-Pangean dextral transform fault system which is required to transfer Gondwana from a Pangea B into a Pangea A configuration compatible with the Arthaud and Matte (1977) concept but also with a geodynamic interpretation of shear systems within Gondwana (see figure 4 in Visser and Praekelt, 1998). Despite that these rotations are compatible with interpretations of the region as a diffuse plate boundary (sensu Gordon, 1998) caution should be used when interpreting these as the ”smoking gun” supporting the validity of Pangea B.

1.3 Geologic Setting, Sampling and Geochronological Constraints

The Late Paleozoic collision of Laurussia and Gondwana with associated terranes created the Variscan (also Hercynian or Alleghenian) belt extending ~ 8000 km from the Appalachians to the Urals forming the supercontinent of Pangea. The complex geometry of the colliding continents (Guiraud et al., 2005), as well as a time-variable stress pattern (e.g. Chopin et al., 2014; Wernert et al., 2016), defined both a transpressional and transtensional tectonic framework combined with an intracontinental strike-slip shear network (Elter et al., 2020; Hoepffner et al., 2006). The Mauritanide segment of the Variscan orogeny in North Africa is predominantly exposed in Morocco, forms the Moroccan Variscides at the northwestern (NW) margin of Gondwana and can be interpreted as the southwestern (SW) prolongation of its European counterpart (Chopin et al., 2014; Elter et al., 2020; Hmich et al., 2006; Hoepffner et al., 2005; Hoepffner et al., 2006; Michard et al., 2008; Michard et al., 2010a; Michard et al., 2010b; Wernert et al., 2016; Zouicha et al., 2022).

Among the Moroccan Variscides, Pennsylvanian-Permian successions are documented mainly in the Western High Atlas and the Western Moroccan Meseta, an area which is roughly confined by a set of dextral wrench faults: the Rabat-Tiflet Fault zone (RTFZ) to the north, the Middle Meseta Fault Zone (MMFZ) to the east and the South Meseta Fault Zone (SMFZ) to the south (Fig. 1.1; Chopin et al., 2014; Hoepffner et al., 2005; Michard et al., 2010a; Wernert et al., 2016).

The Western High Atlas of Morocco (WHA) displays a northeastern-southwestern (NE-SW) elongated morphology subparallel to the Paleozoic Anti-Atlas mountain range divided by the SMFZ. In contrast to the prevalent Mesozoic layers of the Central High Atlas, the WHA mostly consists of Paleozoic and Precambrian deposits (Fig. 1.1). Since the WHA has been

shaped by a variety of tectonic deformation processes, i.e. the initial compressional stage of the Variscan orogeny along dextral wrenching by the SMFZ, Permian-Jurassic continental rifting, Early Cretaceous inversion and mid-Jurassic to Early Cretaceous uplift as well as ultimate Late Cretaceous-Cenozoic shortening, it can be regarded both an oblique slip-structure and an intracontinental fold-and-thrust belt (e.g. Barbero et al., 2011; Lanari et al., 2020; Perez et al., 2019; Skikra et al., 2021 and references therein).

The Western Meseta (WM) is a tabular domain crossed by the dextral Western Meseta Shear Zone (WMSZ) separating the coastal block to the west from the central zone to the east. Accordingly, Paleozoic massifs of the WM (i.e. Jebilet, Rehamna and Central massif) are split by the WMSZ into segments belonging to the coastal block (Western Jebilet and Western Rehamna) and the central zone (Eastern Jebilet, Eastern Rehamna and the Central massif) (Fig. 1.1; Barbero et al., 2011; Chopin et al., 2014; Delchini et al., 2016; Essaifi and Hibti, 2008; Hoepffner et al., 2005; Hoepffner et al., 2006; Michard et al., 2008; Michard et al., 2010b; Saddiqi et al., 2009).

During the transition from the late Carboniferous to the early Permian, principal compressional stress axes changed from N-S to E-W in the WHA and WM which initiated the final phase of the overthickened Variscan orogenic belt (e.g. Doblas et al., 1998; Hadimi et al., 2021; Michard et al., 2008). Gravitational collapse and simple pure shear low-angle extensional detachments induced by the system of dextral strike-slip faults introduced a transtensional tectonic framework forming a Basin-and-Range-type province. As a consequence, synextensional plutonic bodies were emplaced, metamorphic core domains were unroofed and enhanced calc-alkaline magmatic activity created various volcanic deposits as well as dike/sill swarms. Moreover, continental pull-apart basins were contemporaneously formed during the Stephanian-Autunian (Fig. 1.1; Chopin et al., 2014; Doblas et al., 1998; Hadimi et al., 2021; Hoepffner et al., 2006; Michard et al., 2008). These isolated transtensional, rhomb-(half)graben-like or domino-like intramontane basins are preferably oriented N(N)E-S(S)W parallel to the predominant dextral fault system and are filled with continental sedimentary deposits (e.g. terrestrial red beds and siliciclastic molasses) with potential intercalations of bimodal volcanic lava flows (mainly of basaltic to trachy-andesitic and dacitic to rhyolitic affinity), pyroclastic episodes and assemblages of dikes and sills (Barbero et al., 2011; El Hadi et al., 2014; El Wartiti et al., 1990; Elter et al., 2020; Hadimi et al., 2021; Hoepffner et al., 2006; Michard et al., 2008; Voigt et al., 2011b; Zouicha et al., 2022).

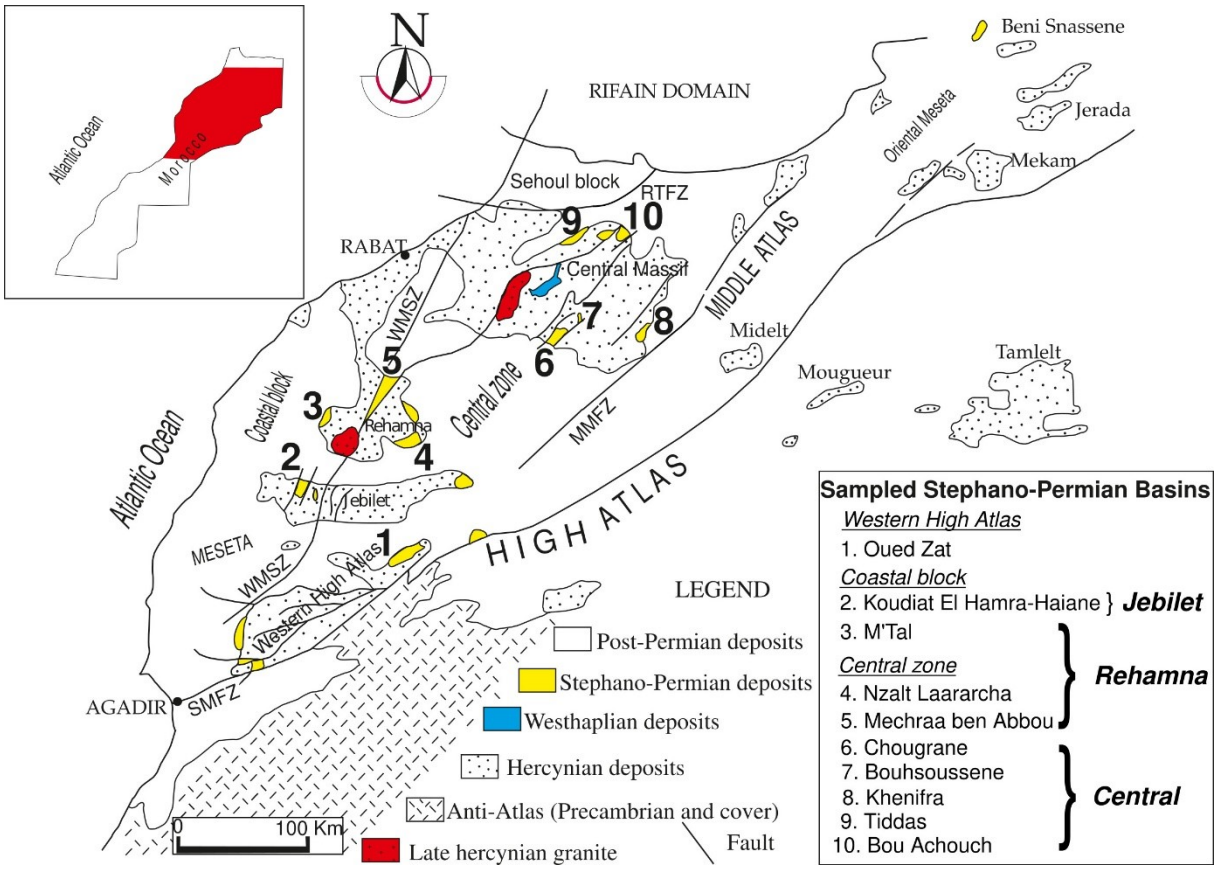

Figure 1.1: Schematic structural and geological map of the sampling area in the Moroccan Variscides. Delimitation of main tectonomorphic domains after Chopin et al. (2014), Hoepffner et al. (2005), Hoepffner et al. (2006), Michard et al. (2008), Michard et al. (2010a) and Michard et al. (2010b). WMSZ: Western Meseta Shear Zone, RTFZ: Rabat-Tiflet Fault Zone, MMSZ: Middle Meseta Fault Zone, SMFZ: South Meseta Fault Zone.

Those pull-apart basins were all created within a setting of major intracontinental strike-slip shear motion (Elter et al., 2020). This broad-scale shear network might function as a geological cornerstone for the mobility between Laurasia and Gondwana and thus for the validity of the Pangea 'B' model. In such a transform fault system, bigger geologic domains are expected to undergo block rotation in ball bearing type setting which can be quantified by variations of the paleomagnetic declination (Aubele et al., 2012; Aubele et al., 2014). Thus, it may be hypothesized that samples from basins close to the boundary of the continental-scale shear zone (i.e., in the north of Morocco) might be significantly more affected by vertical axis rotations than more distant basins (i.e., to the south).

Ten Late Paleozoic basins were studied (Figs. 1.4 – 1.12, Tables 1.1 – 1.10). These are Oued Zat (ZAT) from the Western High Atlas, Koudiat El Hamra-Haiane from the Jebilet massif (JEB), M'Tal (MTA), Nzalt-Lararcha (NL) and Mechraa Ben Abbou (MEC) from the Rehamna Massif and ultimately Chougrane (CHO), El Had Bouhssoussene (BOUH), Khenifra (KHE), Tiddas-Souk Es-Sebt des Ait Ikko (Tsesdai) – in short Tiddas (TID) and Bou Achouch

(BOUA) from the Central Massif where we extracted 615 samples from 97 sites for rock magnetic and paleomagnetic analysis (Fig. 1.1).

Hereafter we briefly summarize the geological, stratigraphic, paleontological and geochronological setting of each individual basin and comment on a possible age model of our samples using available age constraints (Fig. 1.2). Whenever there was comparable data available from literature for the studied basins, we included them in the age model in order to enlarge the data set.

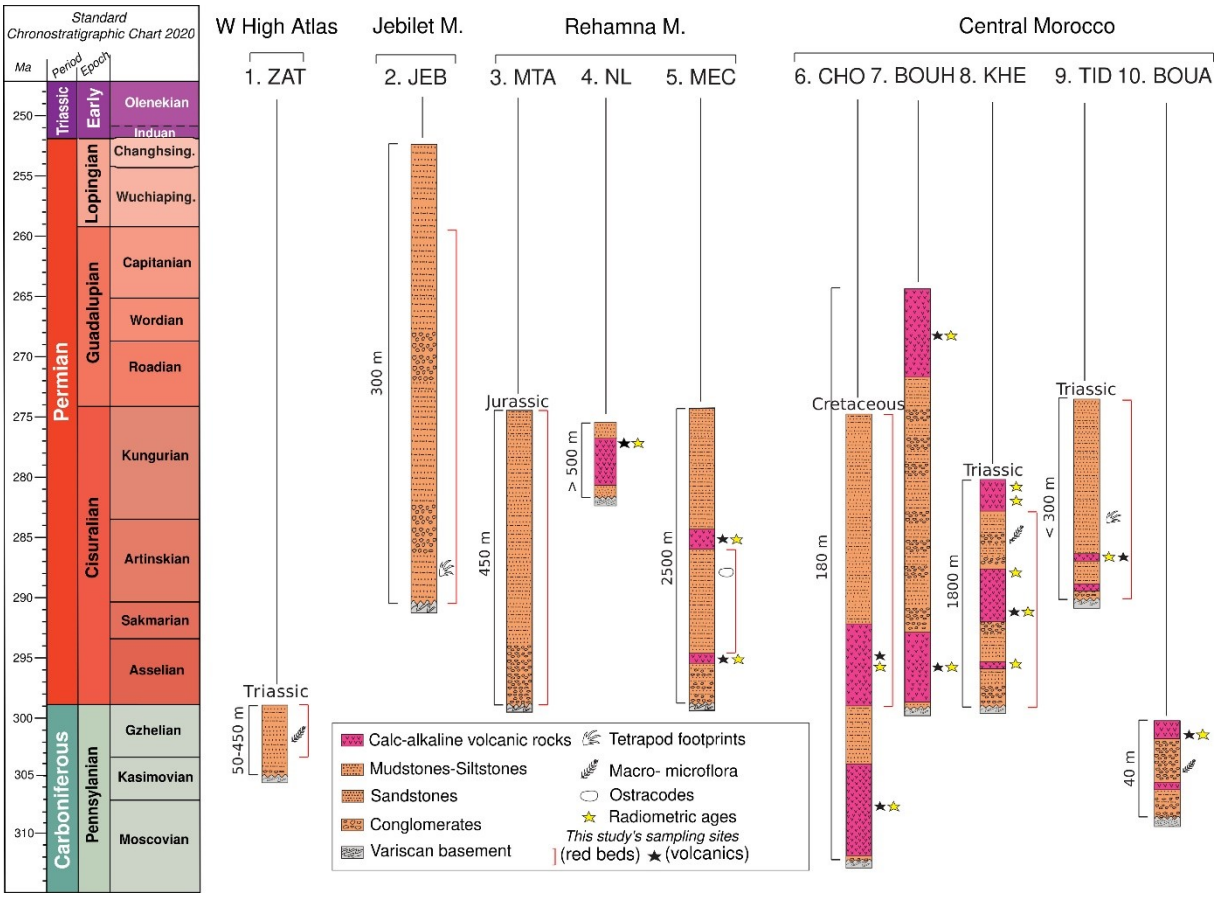

Figure 1.2: Lithostratigraphic correlation of sampled Stephano-Permian basins in Morocco with sampling horizons together with paleontological and radiometric age constraints (see text for further information and references) ordered by corresponding Late Paleozoic domains from south to north (numbering as in Fig. 1.1). Standard Chronostratigraphic chart after Gradstein et al. (2020). Symbols as in legend.

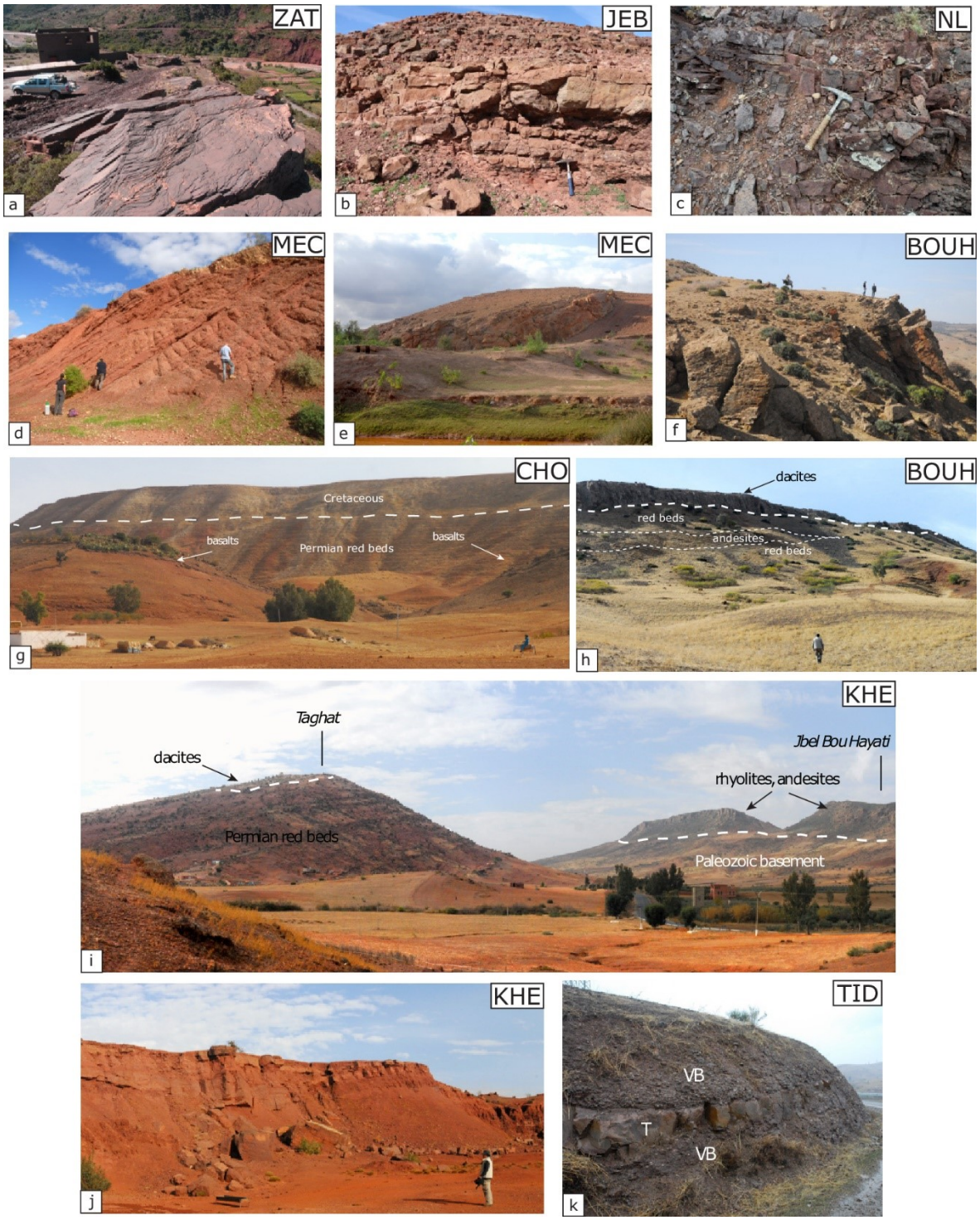

Figure 1.3: Field observations from some sampled Late Paleozoic basins in the Western High Atlas and Western Meseta of Morocco. a) Late Carboniferous fine-grained violet deposits in the Oued Zat basin. b) Panoramic view of the Koudiat El Hamra-Haiane basin profile (Jebilet massif). c) Close-up of the andesite lava flows in the Nzalt-Lararcha basin (Rehamna massif). d) Medium-coarse debris flow deposits in the Mechraa ben Abbou basin (Rehamna massif). e) Bled Mekrach garnet-bearing rhyolitic dome in the MEC basin profile. f) Dacites/andesites at the top of El Had Bouhsoussene basin profile. g) Panoramic view of the volcano-sedimentary succession of Chougrane basin. h) Panoramic view of the volcano-sedimentary succession of BOUH. i) Panoramic view of Khenifra basin from E to W. j) Coarse- to medium-grained red beds in KHE basin (El Messalla quarry). k) Tuff layers (T) intercalated with volcanic breccias (VB) in the Tiddas basin (Ait Ikkou locality).

1.3.1 Oued Zat (ZAT)

ZAT crops out in the northern prolongation of the WHA (Figs. 1.1, 1.4) on the road between Ouarzazate and Tighadwiyn. Its late Carboniferous basin fill is marked by increasing thickness towards the south ranging from 50 to 450 m, is unconformably capped by Triassic red beds and is composed of the following sedimentary formations from base to top: 1) a basal formation (Tighadwiyn formation), composed of purplish red conglomerates mainly composed of rounded quartzite pebbles. The base is erosive and rests unconformably over the green-yellowish flysch of the Visean basement; 2) an upper formation (Mçtour formation), composed of gray-purple to gray-brownish quartz-rich very fine sandstones (Fig. 1.3a), clays and silts containing greenish grey levels with carbonaceous lenses, native sulphur and remains of Stephanian B-C flora (Fig. 1.2; Doubinger and Roy-Dias, 1985; Saber and El Wartiti, 1996; Saber et al., 2007).

Therefore, the Mçtour formation can be roughly attributed to the Gzhelian (303.68 Ma – 298.90 Ma, Aretz et al. (2020)). From this upper section, 74 samples have been drilled at twelve sites (Fig. 1.4, Table 1.1).

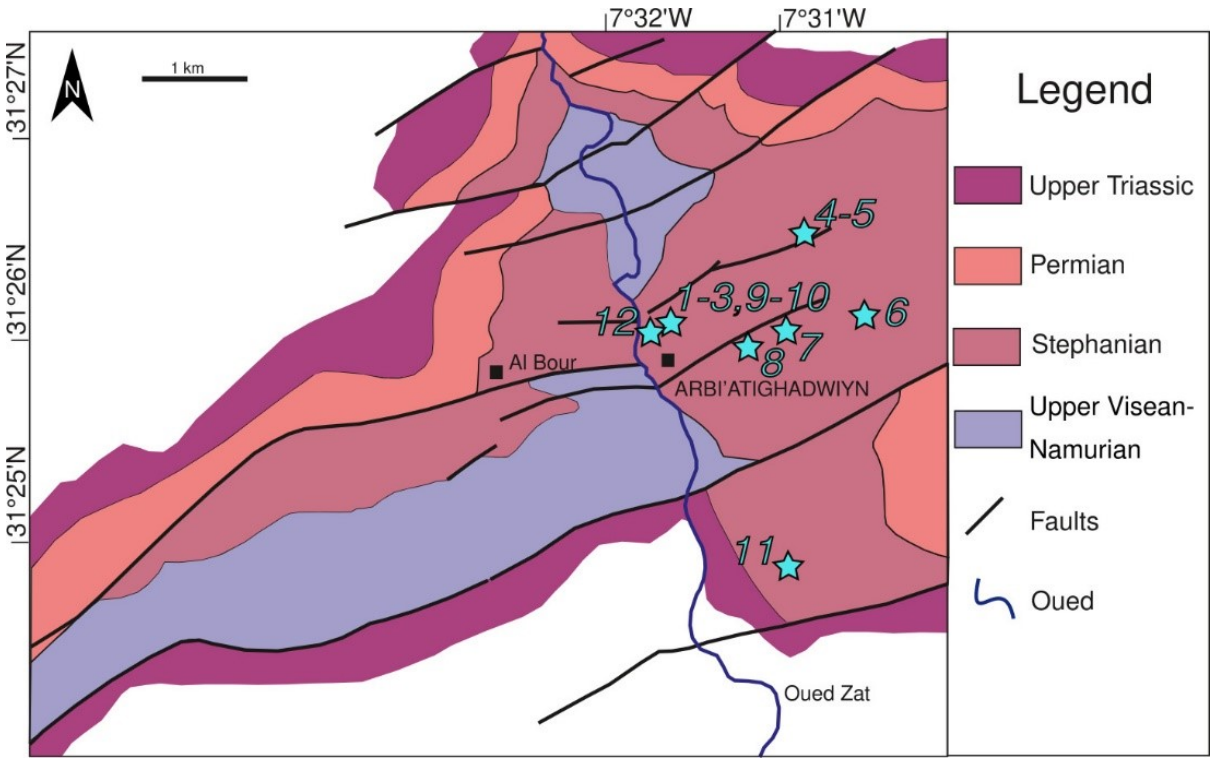

Figure 1.4: Simplified geological map of the basin of Oued Zat (ZAT), based on the geological map of Morocco -sheet Arbi'a Tighadwiyn (1/50000), model completed in 2002 and published in 2016 after Angoud (2016b). Light blue stars specify paleomagnetic site positions of this work. Numbering of samples correlate with Table 1.1. For further explanations see legend. This figure is located in the supplementary materials in the original publication.

***Table 1.1**: Summary of important site characteristics and paleomagnetic results from the Oued Zat (ZAT) basin for the high-stability component (Component B). Site names or quantities marked with an asterisk were not included in paleomagnetic calculations as their α_{95} fisher angle of half cone of 95% confidence exceeded the maximum threshold of 16° as suggested by Van der Voo (1990) or because their reliability is doubted (e.g. available information is not reliable, clear identification of data point as an outlier (superscript: O) or sample number was too small for proper statistical calculations). n/N: number n of specimens included in the determination of the mean direction/number N of measured specimens, all in all 70 specimens from 12 sites have been used. For directional analysis after Kirschvink (1980) a linear (L) and/or great circle (GC) approach was used to determine site-mean directions. Sites that are marked by a superscript 1 are analyzed by GC approach only. Superscript N in the exponent clarifies that the initial polarity of the measured data is reversed and therefore mirrored to be numerically compatible for statistical calculations. Age of the sites is given in steps of million years (Ma). Respective mean age ranges have been determined calculating the arithmetic mean of the minimal and maximal age boundaries. Dip Direction (Dip Dir.) and Dip represent the estimated orientation of the paleohorizontal plane as measured in the field. GLat: Geographic latitude of sampled sites. GLon: Geographic longitude of sampled sites. Declination (Dec), Inclination (Inc) as well as statistical parameters after Fisher (1953), namely k (precision parameter) and α_{95} (angle of half cone of 95% confidence) of mean directions for all sites are given in geographic (in situ) and bedding corrected (tectonic) coordinates. The overall mean direction for ZAT based on the site-mean directions of 11 sites with corresponding fisher parameters is given below the data of the individual sites in bold characters. This table is located in the supplementary materials in the original publication.*

	Site characteristics							In situ (geographic)				Tectonic (bedding corrected)			
Name	n/N	Age [Ma]	Lithology	Dip Dir. [°]	Dip [°]	GLat [°N]	GLon [°E]	Dec [°]	Inc [°]	a95 [°]	k	Dec [°]	Inc [°]	a95 [°]	k
ZAT1	7/7	303.68 – 298.90	Sandstone	169	16	31.434806	-7.527007	125.5	35.8	10.2	36.1	131.4	23.6	10.2	36.1
ZAT2[1]*	4/6	303.68 – 298.90	Sandstone	130	12	31.435069	-7.526729	123.5	7.4	16.1	33.4	123.6	-4.5	16.1	33.4
ZAT3	5/6	303.68 – 298.90	Sandstone	130	12	31.435150	-7.526680	130.6	37.4	9.1	71.5	130.5	25.4	9.1	71.5
ZAT4	6/6	303.68 – 298.90	Sandstone	135	17	31.442851	-7.513185	119	23.7	4.7	208.2	120.3	7.3	4.7	208.2
ZAT5	6/6	303.68 – 298.90	Sandstone	88	12	31.442344	-7.514646	123.4	29	3.7	334.2	120.5	19	3.7	334.2
ZAT6	5/6	303.68 – 298.90	Sandstone	70	15	31.435200	-7.508657	131.3	28.4	9.7	62.8	125.4	20.5	9.7	62.8
ZAT7	6/6	303.68 – 298.90	Sandstone	165	20	31.433534	-7.516489	115.4	24.9	7.4	81.6	120.3	11.2	7.4	81.6
ZAT8	7/7	303.68 – 298.90	Sandstone	165	20	31.433045	-7.519592	137.3	33.6	6.6	84	141.3	15.6	6.6	84
ZAT9	6/6	303.68 – 298.90	Sandstone	174	35	31.435197	-7.527149	133.7	35.7	4.8	200	142	7.1	4.8	200
ZAT10	6/6	303.68 – 298.90	Sandstone	178	17	31.435337	-7.527092	126.2	37.2	8.1	69.1	134	25.7	8.1	69.1
ZAT11	6/6	303.68 – 298.90	Sandstone	32	15	31.415007	-7.516185	114.5	20.1	2.8	564.9	109.4	17.5	2.8	564.9
ZAT12	6/6	303.68 – 298.90	Sandstone	202	32	31.433966	-7.528884	132.9	35	3.5	378.3	147.8	19.4	3.5	378.3
Mean	**11/12**	**303.68 – 298.90**	**-**	**-**	**-**	**31.43**	**352.48**	**126**	**31.2**	**5.1**	**81.9**	**129.3**	**17.8**	**7.3**	**40**

1.3.2 Koudiat El Hamra-Haiane (JEB)

The Koudiat El Hamra- Haiane basin is located in the western Jebilet Massif (Figs. 1.1, 1.5). Its stratigraphic succession shows about 300 m thick siliciclastic deposits with alternation of gray brownish shaly-silty to sandy horizons in the lower part and reddish sandstones to quartz-rich microconglomerates in repeated fining-upward sequences in the middle–upper portion (Fig. 1.3b). Red-ocher calcretes are very frequent in the lower–middle part of the profile (Zouicha et al., 2022). Again, the middle–upper part of the section shows strongly oxidized dark-red coarse sandstones, which contain many plant fragments and roots that suggest wet conditions (Fig. 1.2; Huvelin, 1977). The formation of the Koudiat El Hamra-Haiane basin has initially been attributed to the Westphalo-Permian by Huvelin (1977) which was also confirmed by Delchini et al. (2018). Recently a first record of invertebrate and vertebrate trace fossils was reported by Zouicha et al. (2021) in the lower beds of Koudiat El Hamra – Haiane sections suggesting a late early Permian (Artinskian) to middle Permian (Capitanian) age, i.e. 290.51 – 259.55 Ma following Henderson et al. (2020).

In the Koudiat El Hamra-Haiane basin we drilled 31 samples at five red bed sites (Fig. 1.5; JEB3- JEB8; due to their almost identical position and low number of samples taken at the last site we treat JEB7 and JEB8 as one site JEB7_8). Since one core's orientation could not be retrieved, 30 red bed cores have been paleomagnetically measured (Table 1.2).

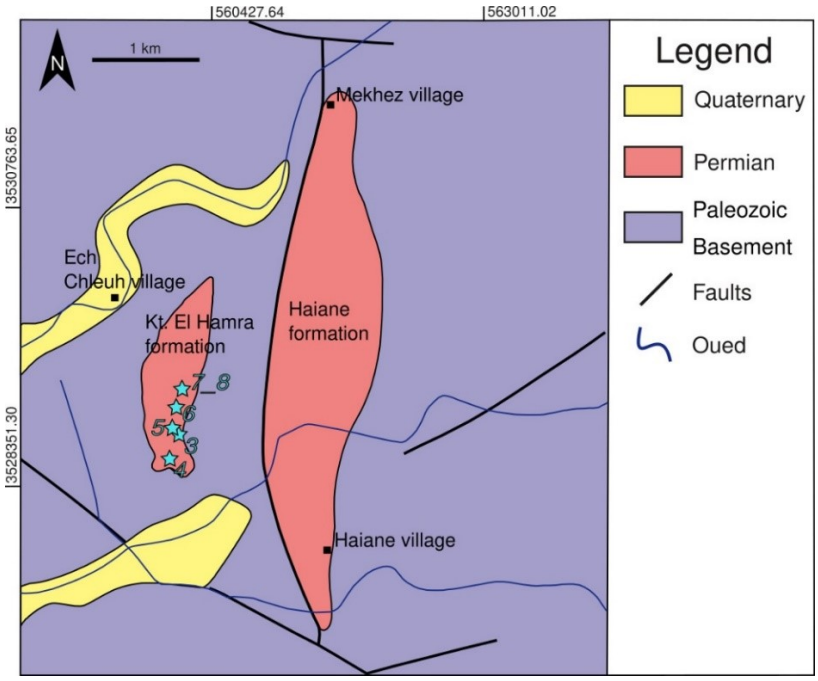

Figure 1.5: Simplified geological map of the sampled area in the Koudiat El Hamra-Haiane basin of the Jebilet Massif (JEB), redrawn and modified after Zouicha et al. (2022). Light blue stars specify paleomagnetic site positions of this work. Numbering of samples correlate with Table 1.2. For further explanations see legend. This figure is located in the supplementary materials in the original publication.

***Table 1.2**: Summary of important site characteristics and paleomagnetic results from the Jebilet Massif (JEB) for Component B, all in all 28 specimens from 5 sites have been used. For details see text and caption of Table 1.1. This table is located in the supplementary materials in the original publication.*

	Site characteristics							In situ (geographic)				Tectonic (bedding corrected)			
Name	n/N	Age [Ma]	Lithology	Dip Dir. [°]	Dip [°]	GLat [°N]	GLon [°E]	Dec [°]	Inc [°]	a95 [°]	k	Dec [°]	Inc [°]	a95 [°]	k
JEB3	5/6	290.51 – 259.55	Red beds	255	20	31.891894	-8.354221	116.9	-37.8	6.5	139.1	109.7	-22.1	6.5	139.1
JEB4*	5/5	290.51 – 259.55	Red beds	230	18	31.889538	-8.355797	137.6	-17.4	25.6	9.9	132.2	-15.8	25.6	9.9
JEB5	5/6	290.51 – 259.55	Red beds	358	15	31.892485	-8.354187	123.4	-35.1	12	41.6	130.3	-25.7	12	41.6
JEB6	6/6	290.51 – 259.55	Red beds	228	11	31.892959	-8.354254	127.3	-16.7	6	125.1	124.3	-14.3	6	125.1
JEB7_8	7/7	290.51 – 259.55	Red beds	228	11	31.894298	-8.354255	123.2	-8	14.5	18.2	122	-5	14.5	18.2
Mean	**4/5**	**290.51 - 259.55**	**-**	**-**	**-**	**31.89**	**351.65**	**123**	**-24.4**	**17.2**	**29.6**	**121.6**	**-16.9**	**14**	**44**

***Table 1.3**: Summary of important site characteristics and paleomagnetic results from the M'Tal basin (MTA) for Component B, all in all 39 specimens from 7 sites have been used. For details see text and caption of Table 1.1. This table is located in the supplementary materials in the original publication.*

	Site characteristics							In situ (geographic)				Tectonic (bedding corrected)			
Name	n/N	Age [Ma]	Lithology	Dip Dir. [°]	Dip [°]	GLat [°N]	GLon [°E]	Dec [°]	Inc [°]	a95 [°]	k	Dec [°]	Inc [°]	a95 [°]	k
MTA1^{N}*	1/1	298.89 – 274.37	Red beds	292	60	32.447401	-8.360516	333.7	45.1	-	-	320.2	-5.9	-	-
MTA2	5/6	298.89 – 274.37	Red beds	292	60	32.447342	-8.361178	129	-51.4	5.8	176.1	122.6	7.2	5.8	176.1
MTA3	5/5	298.89 – 274.37	Red beds	275	43	32.447145	-8.361743	114.3	-51	10.4	55.1	107.2	-9.4	10.4	55.1
MTA4	8/8	298.89 – 274.37	Red beds	283	40	32.447166	-8.362362	132.5	-39.8	5.4	107.5	125.3	-3.4	5.4	107.5
MTA5	6/6	298.89 – 274.37	Red beds	305	32	32.447186	-8.362575	128.1	-41.3	8.4	64.3	127.3	-9.3	8.4	64.3
MTA6	8/8	298.89 – 274.37	Red beds	284	28	32.447405	-8.363451	132.9	-35	4.7	137.6	127.7	-9.8	4.7	137.6
MTA7	6/7	298.89 – 274.37	Red beds	284	28	32.447482	-8.363942	128.9	-26	5.1	176.4	126.2	-0.2	5.1	176.4
Mean	**6/7**	**298.89 – 274.37**	**-**	**-**	**-**	**32.45**	**351.64**	**128.1**	**-40.9**	**9**	**56.1**	**122.8**	**-4.2**	**8.6**	**62.1**

1.3.3 M'Tal (MTA)

The M'Tal basin, the westernmost part of the Rehamna massif, crops out approximately 100 km south of El Jadida, on the road to Marrakech near Jemaâ M'tal (Figs. 1.1, 1.6). According to Saber et al. (2014), the approximately 450 m thick reddish succession consists of a lower part dominated by conglomerates with abundant matrix (Ouled Mira formation) overlain by a succession of sandstone-siltstones (Bir Enhass formation) (Fig. 1.2).

A systematic analysis of the synsedimentary fracturing reveals that the fault network and the opening of the MTA basin were activated during the E-W extension. Based on the analogy of the facies, the geological history and the geographical proximity, the deposits of MTA basin are considered as related to those in the MEC basin, which are Cisuralian (Damotte et al., 1993; Saber et al., 2014), i.e. 298.89 – 274.37 Ma in age (Henderson et al., 2020). From these early Permian red beds of MTA, we drilled 41 cores at seven sites (Table 1.3).

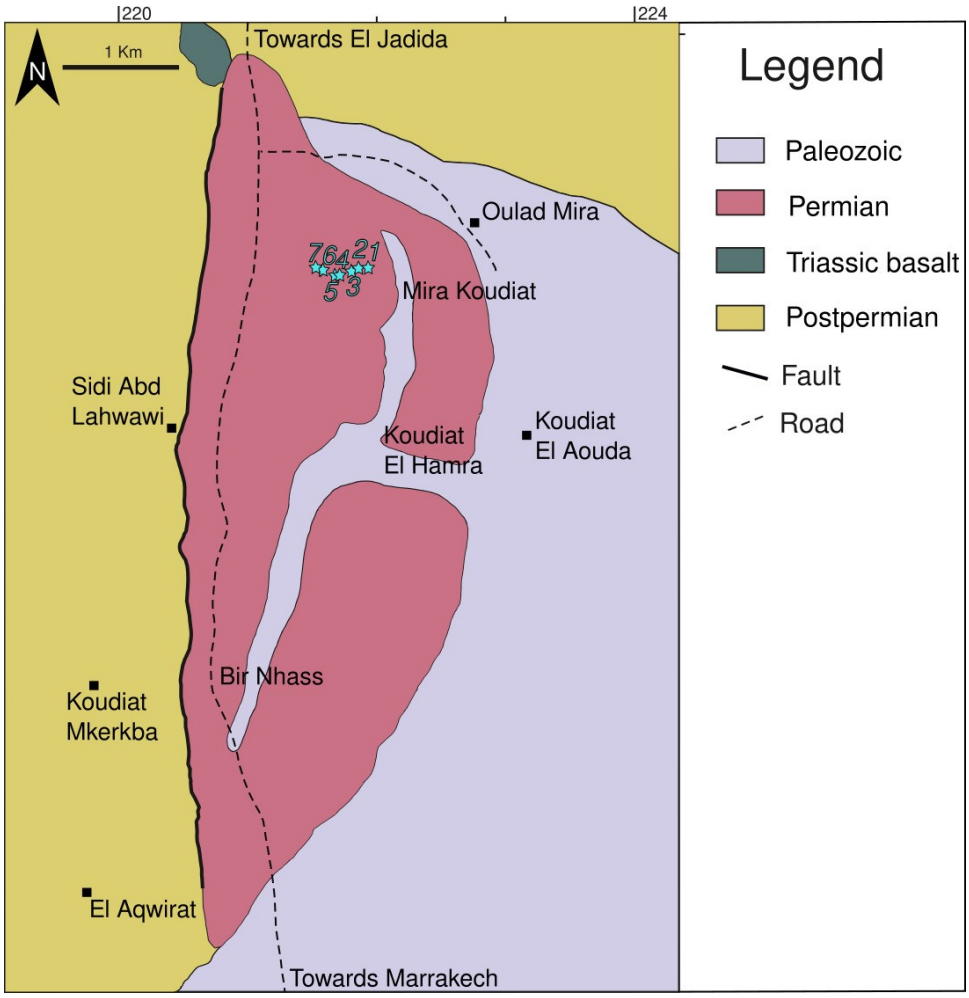

Figure 1.6: Simplified geological map of the sampled area in the M'Tal basin (MTA), redrawn and modified after Saber et al. (2014). Light blue stars show paleomagnetic site positions of this work. Numbering of samples correlate with Table 1.3. For further explanations see legend. This figure is located in the supplementary materials in the original publication.

1.3.4 Nzalt-Lararcha (NL)

NL is located in the SE part of the Rehamna massif (Figs. 1.1, 1.7). The volcano-sedimentary succession is represented by the Sidi Yahia formation exceeding 500 m (Saidi et al., 2002) and is unconformably deposed over the Hercynian basement (Michard, 1976; Michard, 1982). Corresponding sediments, consisting of fine-to-coarse-grained clastics, bracket a series of volcanics (Fig. 1.3c; Charif et al., 1998). Recent dating from a rhyolite in this basin (Sidi Bou Yahia dome) provided a $^{206}Pb/^{238}U$ weighted mean age of 277.07 ± 0.61 Ma, which represents the first absolute age constraint from this basin (Fig 1.2; Domeier et al., 2021).

In the NL basin, we extracted 71 cores of mainly andesitic affinity at eleven different sites (Fig. 1.7, Table 1.4). Since we observed the geochronologically dated dome of Sidi Bou Yahia to interfinger with our adjacent, sampled andesites, a mean age of 277.07 ± 0.61 Ma has been assumed for all samples taken at NL (Table 1.4).

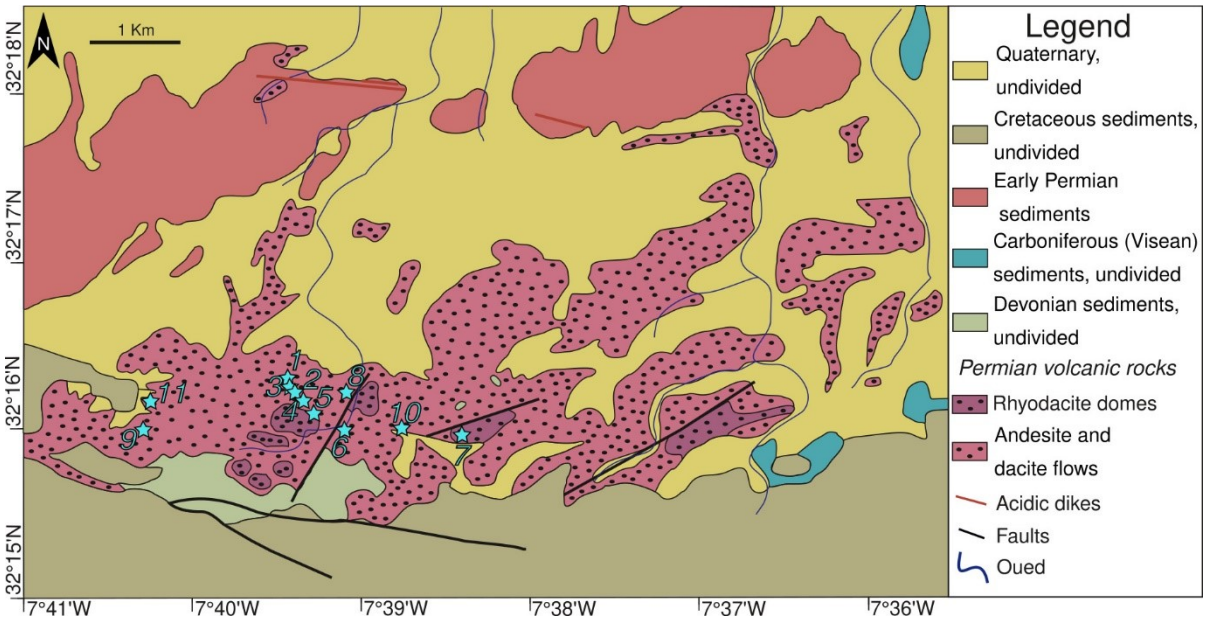

Figure 1.7: Simplified geological map of the basin of Nzalet-Laararcha (NL), redrawn and modified after Domeier et al. (2021). Light blue stars specify paleomagnetic site positions of this work. Numbering of samples correlate with Table 1.4. For further explanations see legend. This figure is located in the supplementary materials in the original publication.

***Table 1.4**: Summary of important site characteristics and paleomagnetic results from the basin of Nzalet el Laraarcha (NL) for the high-stability component (Component B). All in all, 66 specimens from 11 sites have been used. Below this study's data set, paleomagnetic results and site characteristics reported in Domeier et al. (2021), i.e. NE1-3, are also given as a reference. Finally, an overall mean direction integrating both data sets is calculated and as well given in bold characters. For details see text and caption of Table 1.1. This table is located in the supplementary materials in the original publication.*

		Site characteristics						In situ (geographic)				Tectonic (bedding corrected)			
Name	n/N	Age [Ma]	Lithology	Dip Dir. [°]	Dip [°]	GLat [°N]	GLon [°E]	Dec [°]	Inc [°]	a95 [°]	k	Dec [°]	Inc [°]	a95 [°]	k
NL1	3/6	277.07 ± 0.61	Andesite	173	45	32.270979	-7.657277	155	36.7	7	310.3	158.5	-6.7	7	310.3
NL2	6/6	277.07 ± 0.61	Andesite	190	48	32.269968	-7.656834	152	24.4	4.5	226.4	154.5	-14.9	4.5	226.4
NL3	6/6	277.07 ± 0.61	Andesite	173	45	32.269676	-7.657111	143.8	1.6	8.1	68.7	135.5	-36.6	8.1	68.7
NL4	6/6	277.07 ± 0.61	Andesite	173	45	32.269262	-7.655644	151.9	14.5	3	516.3	149.9	-27.5	3	516.3
NL5	6/6	277.07 ± 0.61	Andesite	173	45	32.268613	-7.655216	160.9	29	4.1	267.6	162	-15.2	4.1	267.6
NL6	6/6	277.07 ± 0.61	Andesite	245	25	32.266647	-7.651822	144.9	7.9	4.1	273.9	149.2	11.4	4.1	273.9
NL7*	8/8	277.07 ± 0.61	Rhyodacite	173	45	32.265808	-7.640218	167.3	37.1	13.2	18.5	168.4	-7.8	13.2	18.5
NL8	7/7	277.07 ± 0.61	Andesite	173	45	32.269973	-7.651489	157.5	26.8	2.8	469.4	158.5	-16.8	2.8	469.4
NL9*	4/6	277.07 ± 0.61	Andesite	235	55	32.266483	-7.671447	135.5	13.7	16.7	31.2	151	15.5	16.7	31.2
NL10	7/7	277.07 ± 0.61	Andesite	158	38	32.266732	-7.646370	121.7	32.7	13.8	20.1	128.2	0.5	13.8	20.1
NL11	7/7	277.07 ± 0.61	Andesite	235	55	32.269367	-7.670714	154.8	4.4	11	31	154.2	-5.5	11	31
Mean	**9/11**	**277.68 – 276.46**	**-**	**-**	**-**	**32.27**	**352.34**	**149.3**	**20.1**	**10.8**	**23.8**	**150.3**	**-12.6**	**11.7**	**20.4**
NE1	7/8	277.07 ± 0.61	Andesite	261.4	31.8	32.265	-7.651	136.1	23.4	5.6	117.9	153.5	38.1	5.6	117.9
NE2	7/7	277.07 ± 0.61	Andesite	166.9	37.1	32.265	-7.650	137.1	23.7	10.4	39.4	139.4	-9.1	10.4	39.4
NE3	5/5	277.07 ± 0.61	Andesite	154.4	65.3	32.265	-7.650	139.6	42.1	12.1	41	142.6	-21.8	12.1	41
All mean	**12/14**	**277.68 – 276.46**	**-**	**-**	**-**	**32.27**	**352.35**	**146.5**	**22.6**	**8.9**	**24.9**	**149**	**-9.2**	**12**	**14.2**

1.3.5 Mechraa Ben Abbou (MEC)

The basin of MEC is part of the northern Rehamna massif and is predominantly filled by clastic deposits (Figs. 1.1, 1.8; Damotte et al., 1993; El Kamel, 1987; El Wartiti et al., 1992; El Wartiti et al., 1990). The huge fining-to-coarsening upward red-bed succession with an estimated thickness of about 2500 m is interrupted by two volcanic pulses and can be subdivided into two sequences. The lower segment starts with talus-cone conglomerates-breccias, evolving into fluvial sandstones and to floodplain deposits. Then the sequence continues in the middle-upper part again with thick fluvial deposits and mudflows (Fig. 1.3d). In the fine-grained middle part of the succession, rare lacustrine carbonates and mudstones contained stromatolites, algal buildings and an ostracod fauna occur which permit to ascribe the series to the Cisuralian (Fig. 1.2; Damotte et al., 1993), i.e. 298.89 – 274.37 Ma (Henderson et al., 2020).

The volcanic rocks of MEC are intercalated in the red beds (e.g. Gigout, 1951; Hoepffner, 1982) and appear as massive/fluidal andesitic lava flows, interspaced to the lower clastic deposits of the first sedimentary sequence, and as rhyolitic domes associated with the second sequence (e.g. the Bled Mekrach garnet-bearing rhyolitic dome; Figs. 1.2, 1.3e). The thickness of these volcanic rocks varies from a few tens to 500 meters depending on their proximity to the effusive centers (Hadimi et al., 2018).

U-Pb zircon ages by Sensitive High-Resolution Ion Microprobe (SHRIMP) on the Bled Mekrach garnet-bearing rhyolitic dome was recently performed by Hadimi et al. (2018): A concordant age obtained is 285.3 ± 4.9 Ma. More recent datings by Domeier et al. (2021) were performed on the andesite flow and andesite plug and yield $^{206}Pb/^{238}U$ ages of 284.2 ± 4.6 and 294.63 ± 0.67 Ma, respectively.

In the Mechraa Ben Abbou basin, 68 paleomagnetic cores at 11 different sites (five of rhyolitic and two of andesitic geochemistry as well as four red bed sites) were drilled (Fig. 1.8, Table 1.5). Sites MEC1-3 and MEC10-11 all come from the Bled Mekrach garnet rhyolitic dome (Fig. 1.3e), which is why we assign an age of 285.3 ± 4.9 Ma (Fig. 1.2). At andesitic sites MEC4 and MEC5, direct contact to the basal conglomerates was identified, which stratigraphically ties them to the early phase of volcanism in MEC, which is why we assume by lithological correlation a mean age of 294.63 ± 0.67 Ma for them (Fig. 1.2). Additionally, an older paleomagnetic study from Westphal et al. (1979) documents two paleomagnetic sites in MEC (104 and 105) suspected to belong to the Mekrach rhyolitic dome complex and therefore assigned a provisional age of 285.3 ± 4.9 Ma (Table 1.5).

Eventually, since our red bed samples from MEC6-9 from the sedimentary record are stratigraphically bracketed by the basal andesitic lavas and the Bled Mekrach garnet rhyolitic dome, their deposition age is determined by these two magnetic pulses (Fig. 1.2; Table 1.5).

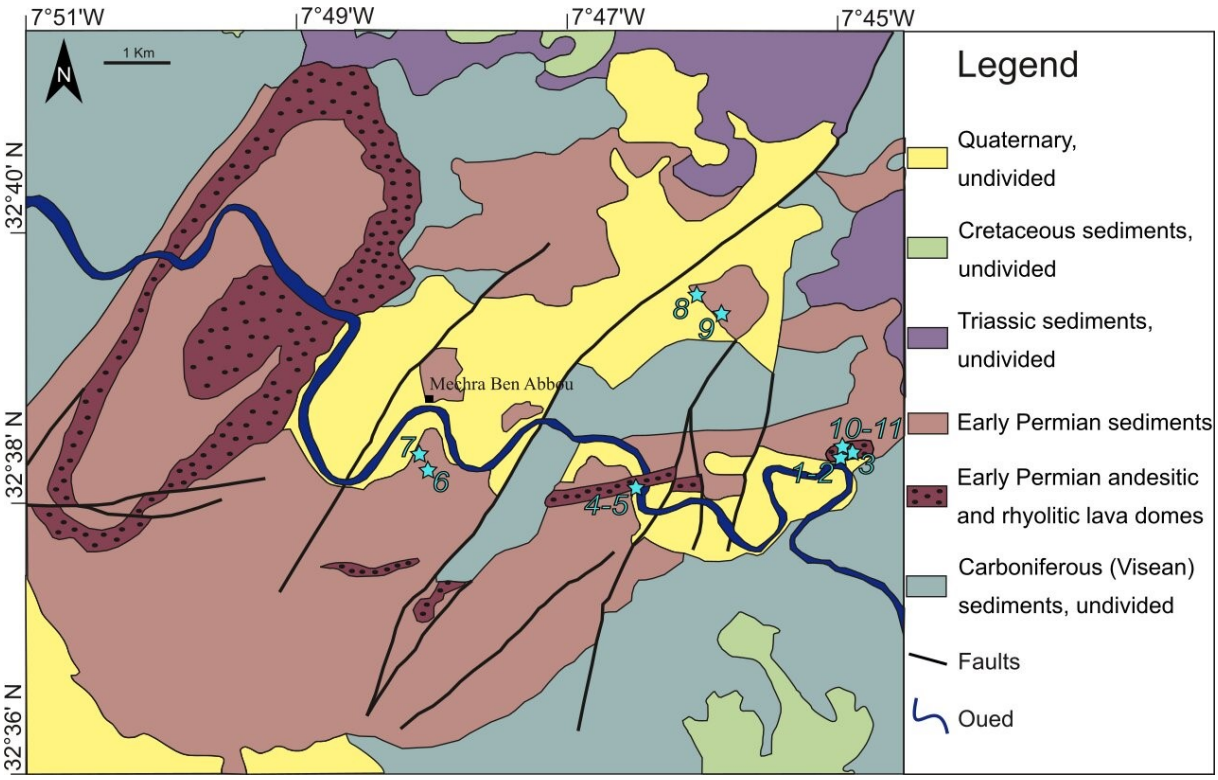

Figure 1.8: Simplified geological map of the basin of Mechraa Ben Abbou (MEC), redrawn and modified after Domeier et al. (2021). Light blue stars specify paleomagnetic site positions of this work. Numbering of samples correlate with Table 1.5. For further explanations see legend. This figure is located in the supplementary materials in the original publication.

1.3.6 Chougrane-El Had Bouhssoussene (CHO-BOUH)

The Permian volcanic Chougrane-El Had Bouhsoussene complex in the southern part of the Central Massif trends along a NE-SW oriented axis with an approximate length of 20 km and a maximum width of 8 km covering an area of about 110 km^2 (Figs. 1.1, 1.9; Domeier et al., 2021). The wedge-shaped basin hosts a volcano-sedimentary succession with a thickness of about 180 m (Boutsougame et al., 2016). The BOUH-CHO basin was created by intracontinental transtensional tectonics in the Asturian phase during the late Carboniferous (Michard, 1976) and recorded two major eruptive episodes and a third phase dominated by dyke and sill emplacements. The eruptive episodes are represented by rhyodacites and overlain basalts (e. g. Fig 1.3f) which are intercalated in the reddish clay-sandstone-conglomeratic Permian deposits (Figs. 1.2, 1.3g, 1.3h; Boutsougame et al., 2016).

***Table 1.5**: Summary of important site characteristics and paleomagnetic results from the basin of Mechraa Ben Abbou (MEC) for the high-stability component (Component B), all in all 68 specimens from 11 sites have been used. Sites reported in Domeier et al. (2021), MB1, MB2, MB3 as well as MB5, and Westphal et al. (1979), 104 and 105, are listed and combined with this study's data for reference (if necessary, site mean position was estimated from available information). For details see text and caption of Table 1.1. This table is located in the supplementary materials in the original publication.*

	Site characteristics							In situ (geographic)				Tectonic (bedding corrected)			
Name	n/N	Age [Ma]	Lithology	Dip Dir. [°]	Dip [°]	GLat [°N]	GLon [°E]	Dec [°]	Inc [°]	a95 [°]	k	Dec [°]	Inc [°]	a95 [°]	k
MEC1	6/6	285.3 ± 4.9	Rhyolite	340	35	32.638815	-7.750616	141.8	-20.4	7.5	80.6	142.6	13	7.5	80.6
MEC2	6/6	285.3 ± 4.9	Rhyolite	340	35	32.638915	-7.750255	143	-20.5	4.8	196.8	143.7	13.1	4.8	196.8
MEC3	6/6	285.3 ± 4.9	Rhyolite	245	26	32.639385	-7.749270	148	-20.8	7.5	80.8	139.5	-15.6	7.5	80.8
MEC4	6/6	294.63 ± 0.67	Andesite	355	45	32.635079	-7.774648	169.2	-46.3	3.7	337	171	-1.5	3.7	337
MEC5	6/6	294.63 ± 0.67	Andesite	355	45	32.635261	-7.774595	113.9	-44.2	8.4	65.3	134.6	-14.4	8.4	65.3
MEC6	7/7	295.3 – 280.4	Red beds	342	34	32.638565	-7.801280	152	-34.2	3.8	256.2	153.7	-0.6	3.8	256.2
MEC7	7/7	295.3 – 280.4	Red beds	338	36	32.639055	-7.801161	153	-35.7	5.6	115.5	154	0.2	5.6	115.5
MEC8	6/6	295.3 – 280.4	Red beds	340	35	32.660519	-7.769411	152.4	-24.8	3.7	324.8	153	10	3.7	324.8
MEC9	6/6	295.3 – 280.4	Red beds	340	35	32.660595	-7.769378	148.3	-21.7	6.1	122.5	148.9	12.7	6.1	122.5
MEC10*	6/6	285.3 ± 4.9	Rhyolite	57	27	32.639756	-7.748816	138.2	-27.4	18.6	14	152.7	-28.1	18.6	14
MEC11	6/6	285.3 ± 4.9	Rhyolite	35	44	32.639813	-7.749056	154.4	-26.5	12.6	29.4	164	-2.5	12.6	29.4
Mean	**10/11**	**293.3 – 283.1**	**-**	**-**	**-**	**32.64**	**352.23**	**147.8**	**-30**	**9**	**29.8**	**150.6**	**1.5**	**9.3**	**27.8**
MB1	5/5	294.63 ± 0.67	Andesite	311.8	34.1	32.657	-7.809	149.3	-38.7	4.4	297.8	145.4	-5.8	4.4	297.8
MB2	7/8	284.2 ± 4.6	Andesite	295.3	47.2	32.660	-7.811	133.6	-52.1	3.3	336.6	126.5	-6.2	3.3	336.6
MB3	9/9	294.63 ± 0.67	Andesite	321.4	35.5	32.658	-7.811	146.2	-39.8	2.3	522.9	145.1	-4.4	2.3	522.9
MB5	8/8	285.3 ± 4.9	Rhyolite	310.4	41.5	32.639	-7.751	147.8	-24.1	9.2	37.5	146.9	15.7	9.2	37.5
Mean VW+DO	**14/15**	**293.0 – 284.2**	**-**	**-**	**-**	**32.65**	**352.22**	**147**	**-32.6**	**7.2**	**31.8**	**147.8**	**1**	**7.6**	**28.4**
104*	5/6	285.3 ± 4.9	Rhyolite	?	?	?(32.645)	?(-7.775)	?	?	?	?	107	4	19	14
105	6/6	285.3 ± 4.9	Rhyolite	?	?	? (32.645)	?(-7.775)	?	?	?	?	146	-6	6	116
Mean all	**15/17**	**292.8 – 284.0**	**-**	**-**	**-**	**32.65**	**352.22**	-	-	-	-	**147.7**	**0.5**	**7.1**	**30.1**

The basin can further be subdivided into spatially separated successions in the northeast (Bouhsoussene – BOUH) and the southwest (Chougrane – CHO). In this context, 66 paleomagnetic samples (volcanic rocks of various compositions) were collected at 11 sites in BOUH whereas 100 paleomagnetic cores were retrieved at 14 sites (five red beds, four sills and five volcanics) in CHO. Here, 94 out of 99 samples could be paleomagnetically measured (Tables 1.6 and 1.7).

The age of 270 ± 17 Ma of the BOUH-CHO complex is historically based on whole rock K-Ar data from volcanic rocks at Bir el Gassaa (Van Houten, 1976). Moreover, the petrographic and geochronological characteristics of these extrusive rocks are comparable to those of the Cisuralian volcanic successions of KHE and TID (Hadimi et al., 2021; Youbi et al., 2018). On top of that, the volcanic pulses of CHO and BOUH can be temporally correlated via lithostratigraphy (Cailleux et al., 1983; Youbi, 1998). Recently, Domeier et al. (2021) reported geochronological data (although potentially affected by inheritance and Pb loss) from Bir el Gassaa (their sample TC1G) and Souk el Had Bouhsoussene (their sample TZ1G), which triggered some controversy about their respective eruption ages. TC1G provides age ranges of 307.8 ± 4 Ma to 295.5 ± 3.4 Ma. Inconsistently with its stratigraphic position, the TZ1G provides $^{206}Pb/^{238}U$ ages which span the early and middle Permian from 295.6 ± 2.9 to 267.9 ± 3.9. Thus, Domeier et al. (2021) contend that these geochronological results might suggest that the Souk el Had Bouhsoussene sub-basin is younger than Chougrane therefore discounting the existing stratigraphic models.

Considering BOUH's available geochronological constraints (i.e. TZ1G), we can roughly attribute an intrusion age between 298.5 Ma and 264 Ma for our sites BOUH1-11 as well as paleomagnetic sites reported from literature, i.e. Domeier et al. (2021; TZ1) and Daly and Pozzi (1976) (Table 1.7).

Apart from the geochronology sample TC1G from Domeier et al. (2021) only the whole-rock K-Ar absolute age constraint (270 ± 17 Ma) of Van Houten (1976) is available for CHO clearly deviating from each other in its absolute age dating. Since the latter's quality cannot be compared to modern standards, we are aware of its unreliable character and prefer to generously confine the emplacement of CHO's volcanic rocks using the available geochronological data from Domeier et al. (2021). Based on the considerations delineated above we assign an age range of 311.8 – 292.1 Ma to the volcanic sequences studied in CHO. This age also applies to earlier studies of the basin (Domeier et al., 2021; Westphal et al., 1979; see table 1.6). The red

beds sampled in this study and by Daly and Pozzi (1976; their Série A) are estimated to belong to the Cisuralian, spanning 298.89 – 274.37 Ma according to Henderson et al. (2020).

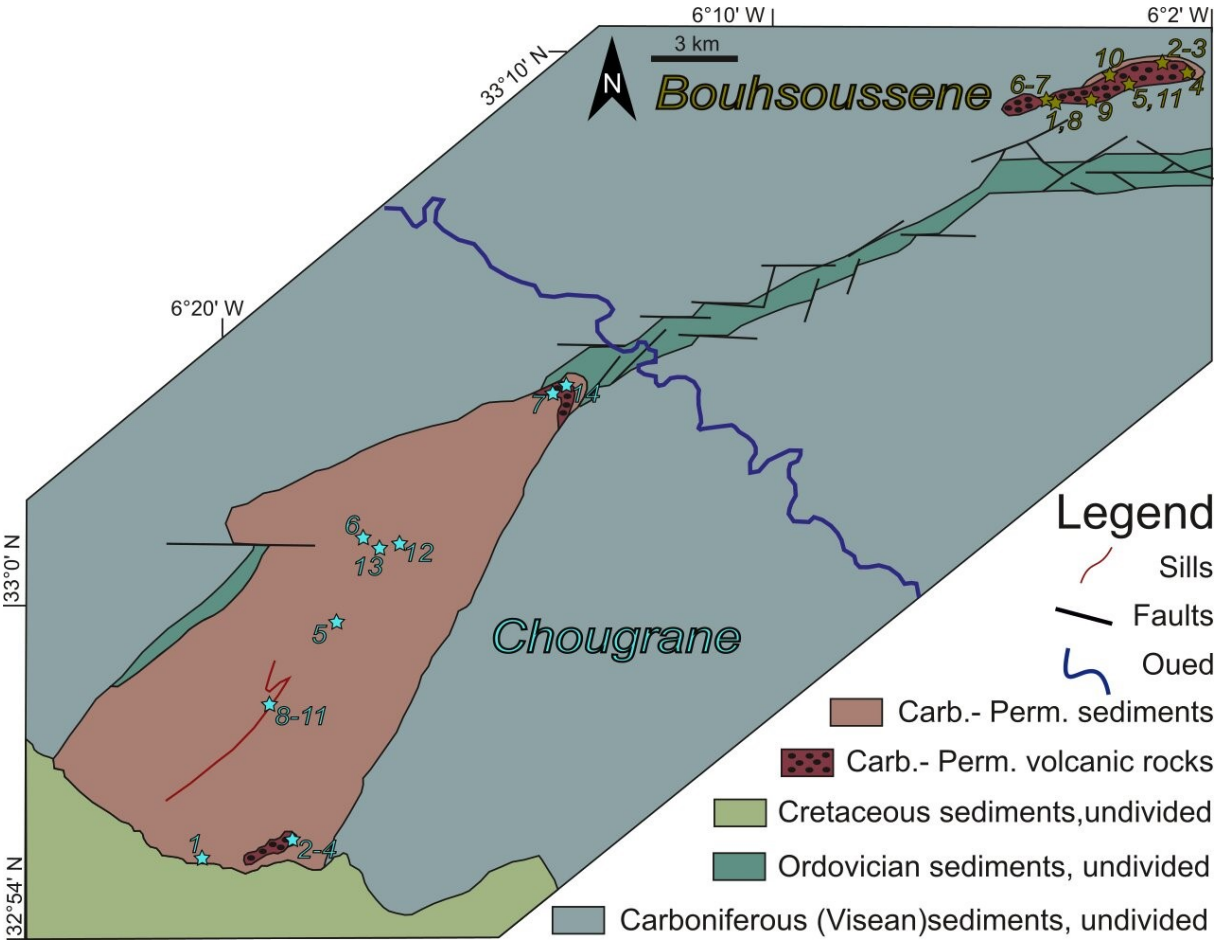

Figure 1.9: Simplified geological map of the basins of Chougrane (CHO) and Bouhsoussene (BOUH), redrawn and modified after Domeier et al. (2021). Light blue (brown) stars specify this work's paleomagnetic site positions from Chougrane (Bouhsoussene). Numbering of samples correlate with Tables 1.6 (CHO) and 1.7 (BOUH). For further explanations see legend. This figure is located in the supplementary materials in the original publication.

1.3.7 Khenifra (KHE)

The 7x17 km large, SSW-NNE trending Khenifra basin is situated about 160 km SE of Rabat in the eastern part of the Central Massif close to the western front of the Middle Atlas (Figs. 1.1, 1.10; Broutin et al., 1998; Voigt et al., 2011b; Youbi et al., 1995). KHE refers to a succession of red beds that unconformably rests on the Hercynian basement of Ordovician to early Carboniferous age (Termier, 1936). El Wartiti et al. (1990) proposed a lithostratigraphic division of the Late Paleozoic deposits into three members of similar thickness:

***Table 1.6**: Summary of important site characteristics and paleomagnetic results from the basin of Chougrane (CHO) for the high-stability component (Component B), all in all 93 specimens from 14 sites have been used. At the end, sites TC1 and TC2 of Domeier et al. (2021), Série A, of Daly and Pozzi (1976), and sites 74 and 75 of Westphal et al. (1979) are listed and combined with this study's data. For details see text and caption of Table 1.1. This table is located in the supplementary materials of the original publication.*

	Site characteristics							In situ (geographic)				Tectonic (bedding corrected)			
Name	n/N	Age [Ma]	Lithology	Dip Dir. [°]	Dip [°]	GLat [°N]	GLon [°E]	Dec [°]	Inc [°]	a95 [°]	k	Dec [°]	Inc [°]	a95 [°]	k
CHO1^{N}*	5/5	298.89 – 274.37	Red beds	2	26	32.919915	-6.339769	326.8	15	20.3	15.1	328	-6.6	20.3	15.1
CHO2	7/8	311.8 – 292.1	Andesite	0	0	32.926389	-6.315791	122.5	-7.6	13.7	20.5	122.5	-7.6	13.7	20.5
CHO3	7/7	311.8 – 292.1	Andesite	0	0	32.926114	-6.315334	124.4	-1.8	8.8	48.3	124.4	-1.8	8.8	48.3
CHO4	6/6	311.8 – 292.1	Andesite	0	0	32.927100	-6.314797	122.3	-10.6	7.4	82.3	122.3	-10.6	7.4	82.3
CHO5	6/6	298.89 – 274.37	Red beds	330	11	32.991564	-6.298476	144.7	-22.9	10.2	44.4	145	-11.9	10.2	44.4
CHO6	7/7	298.89 – 274.37	Red beds	354	7	33.020688	-6.287488	131.2	-14.4	5.5	123.6	132.2	-9.3	5.5	123.6
CHO7	6/6	311.8 – 292.1	Andesite	350	20	33.066351	-6.233673	142.5	-15.1	5.6	142.1	143.4	2.8	5.6	142.1
CHO8	8/8	311.8 – 292.1	Andesite S.	148	55	32.965417	-6.319802	134.7	23.4	11.6	23.6	133.9	-30.3	11.6	23.6
CHO9	7/7	311.8 – 292.1	Andesite S.	148	55	32.965654	-6.319470	116.1	23.8	13.5	20.8	116.1	-23.8	13.5	20.8
CHO10*	6/6	311.8 – 292.1	Basaltic S.	150	30	32.968028	-6.317027	153.8	17.9	18.3	14.4	153.7	-12.1	18.3	14.4
CHO11	6/6	311.8 – 292.1	Basaltic S.	200	37	32.968319	-6.312823	124.2	15.2	9.4	51.9	130.3	3.8	9.4	51.9
CHO12	10/10	298.89 – 274.37	Red beds	90	15	33.016294	-6.283063	124.7	7.9	11	20.4	124.5	-4.5	11	20.4
CHO13	6/6	298.89 – 274.37	Red beds	250	4	33.017020	-6.288834	157.9	-6.4	15.3	20.1	157.5	-6.2	15.3	20.1
CHO14	6/6	311.8 – 292.1	Andesite	197	20	33.068264	-6.229809	149	-3.9	5.7	137.9	146.1	-17	5.7	137.9
Mean	**12/14**	**307.5 – 286.2**	**-**	**-**	**-**	**32.99**	**353.71**	**132.8**	**-1.1**	**10.9**	**16.7**	**133.2**	**-9.9**	**8.6**	**26.4**
TC1	6/6	311.8 – 292.1	Andesite	178.1	6.3	32.927	-6.314	123.5	-8.4	5.9	134.2	122.6	-12	5.9	134.2
TC2	7/7	311.8 – 292.1	Andesite S.	135.3	29.4	32.942	-6.345	138.4	12.1	10.9	32.2	138.5	-17.3	10.9	32.2
Mean VW+DO	**14/16**	**308.1 – 287.0**	**-**	**-**	**-**	**32.98**	**353.7**	**132.5**	**-0.7**	**9.6**	**18.3**	**132.8**	**-10.6**	**7.5**	**29.3**
Sèrie A	?/45	298.89 – 274.37	Red beds	?	?	33.0	-6.3	?	?	?	?	127	-6	4.7	20
74	6/6	311.8 – 292.1	Trachyand.	?	?	?(32.982)	?(-6.298)	?	?	?	?	137	-5	4	370
75	6/6	311.8 – 292.1	Trachyand.	?	?	?(32.982)	?(-6.298)	?	?	?	?	141	-5	6	113
Mean all	**17/19**	**308.0 – 286.9**	**-**	**-**	**-**	**32.98**	**353.7**	-	-	-	-	**133.2**	**-9.7**	**6.2**	**33.9**

***Table 1.7**: Summary of important site characteristics and paleomagnetic results from the basin of Souk El Had Bouhsoussene (BOUH) for the high-stability component (Component B), all in all 57 specimens from 11 sites have been used. At the end, site TZ1, reported in Domeier et al. (2021) and Série B, sampled in the course of the study of Daly and Pozzi (1976), are listed and combined with this study's data for reference. Superscript A represents application of bedding correction determined via AMS measurements instead of field measurements (Domeier et al., 2021). For details see text and caption of Table 1.1. This table is located in the supplementary materials in the original publication.*

	Site characteristics							In situ (geographic)				Tectonic (bedding corrected)			
Name	n/N	Age [Ma]	Lithology	Dip Dir. [°]	Dip [°]	GLat [°N]	GLon [°E]	Dec [°]	Inc [°]	a95 [°]	k	Dec [°]	Inc [°]	a95 [°]	k
BOUH1	6/6	298.5 – 264	Rhyolite	180	27	33.148811	-6.087227	133.6	6.7	2.4	770.6	132.7	-11.9	2.4	770.6
BOUH2^{N}	5/6	298.5 – 264	Basalt	185	20	33.163104	-6.049326	303.4	-13.7	4.9	244.6	306.1	-3.7	4.9	244.6
BOUH3	5/5	298.5 – 264	Basalt	185	20	33.162929	-6.047583	135.2	0.6	12.1	41.2	133.6	-12.1	12.1	41.2
BOUH4	7/7	298.5 – 264	Andesite	185	8	33.161327	-6.040318	137.8	-7.1	3.4	314.2	136.8	-12.5	3.4	314.2
BOUH5	6/6	298.5 – 264	Rhyodacite	80	20	33.155969	-6.063091	148.9	11.6	10.9	38.7	146.3	3.9	10.9	38.7
BOUH6	6/6	298.5 – 264	Rhyolite	220	25	33.149654	-6.088550	142.9	7	12.8	28.4	144.6	0.9	12.8	28.4
BOUH7	2/6	298.5 – 264	Rhyolite	220	25	33.149976	-6.088108	141.7	-4.9	9.7	665	138.6	-9.3	9.7	665
BOUH8	6/6	298.5 – 264	Rhyolite	220	25	33.151063	-6.085787	139.5	-3.6	7.1	90.1	137.1	-7.3	7.1	90.1
BOUH9	2/6	298.5 – 264	Andesite	22	25	33.149603	-6.075406	137.1	-15.3	7.4	1141.6	140.9	-3.8	7.4	1141.6
BOUH10	6/6	298.5 – 264	Rhyodacite	163	22	33.156504	-6.067040	139.2	4.8	8	71.9	138.4	-15.3	8	71.9
BOUH11	6/6	298.5 – 264	Rhyolite	123	31	33.157427	-6.062866	144.2	12.5	4.5	219	144.6	-16.5	4.5	219
Mean	**11/11**	**298.5 – 264**	**-**	**-**	**-**	**33.16**	**353.93**	**138.5**	**2.4**	**6.4**	**51.6**	**138.1**	**-7.3**	**5.4**	**73.1**
TZ1	9/9	298.5 – 264	Andesite	92.7^{A}	35.0^{A}	33.148	-6.092	149	-0.2	2.7	363.9	154.2	-18.7	2.7	363.9
Mean VW+DO	**12/12**	**298.5 – 264**	**-**	**-**	**-**	**33.16**	**353.93**	**139.4**	**2.2**	**6.1**	**52.3**	**139.4**	**-8.3**	**5.7**	**58.4**
Sèrie B	?/12	298.5 – 264	Trachyand.	?	?	32.2	-6.0	?	?	?	?	136	-5	4.6	80
Mean all	**13/13**	**298.5 – 264**	**-**	**-**	**-**	**33.08**	**353.94**	-	-	-	-	**139.2**	**-8.1**	**5.3**	**62.7**

a) the lower member consists of stacked, coarse-grain dominated, fining-upward cycles whose conglomerates, sandstones, and few mudstones were probably accumulated in an alluvial-fan to alluvial-plain environment with major gradient changes (Fig 1.3j). b) the middle member is characterized by a volumetric dominance of red and grey mudstones representing deposition on an extended floodplain. c) the upper member is located above an erosional unconformity indicating activation of the basin relief and begins with fluvial conglomerates; towards the top, fine-grained sandstones and pedogenetically overprinted mudstones become increasingly frequent. After red-bed deposition had ceased, first rhyolitic-rhyodacitic, then dacitic-andesitic flows were emplaced within the succession to form lower Permian volcanics that outcrop in the center of the basin and along its north-western margin (Fig. 1.3i; Youbi et al., 1995). The whole section reaches an approximate thickness of 1800 m and is unconformably overlain by Late Triassic sediments (Fig. 1.2; Domeier et al., 2021 and references therein).

Macro- and microfloral remains in the middle part of the sedimentary succession of interbedded conglomerates, sandstones, and mudstones are supposed to be of middle to late early Permian age (Aassoumi et al., 1992; Broutin et al., 1998). More generally, the whole succession spans for most of the early Permian (Domeier et al., 2021).

The oldest volcanic pulse is represented by dacitic lava flows in the center of the basin at Taghat Hill and is dated by U-Pb on zircon analysis to be 295.1 ± 2.9 Ma in age (Youbi et al., 2018). The composite volcanic dome of Sidi Tiri represents the largest occurrence of Permian volcanics in Morocco, crops out in the western part of KHE and unconformably overlies the Paleozoic basement. This complex made up of rhyolites, andesites and hybrid lavas yielded U/Pb SHRIMP ages ranging from 290.6 ± 2.6 Ma, 290.3 ± 2.1 Ma to 287.9 ± 3.8 Ma (Youbi et al., 2018). Finally, the emplacement of the last volcanic pulse (Talat Mechtal lava flows) capping the whole volcano-sedimentary succession can be bracketed between 282.76 ± 2.19 Ma (Domeier et al., 2021) and 280.3 ± 2.1 Ma (Youbi et al., 2018). In addition, reported ages of 305.59 ± 2.68 Ma (Domeier et al., 2021) or 264 ± 10 Ma (Jebrak, 1985) are either in conspicuous conflict with the other age constraints or do not fulfil modern quality requirements.

In the Khenifra basin, 49 paleomagnetic cores at 8 sites (five red beds and three rhyolites) were drilled (Fig. 1.10, Table 1.8). The sedimentary sites (KHE1-5 from this study and site M10 from Martin et al. (1978)) were sampled in lower Permian red beds that are capped by Talat Mechtal lava flows with the latest emplacement age at 280.57 Ma hence bracketing deposition between 298.89 Ma and 280.57 Ma (Table 1.8; Henderson et al., 2020).

Khenifra's oldest volcanic pulse, the dacites of Jbel Taghat Hill, has recently been dated 295.1 ± 2.9 Ma based on U-Pb on zircon analysis by Youbi et al. (2018). The rhyolitic samples KHE6-8 taken northwest of KHE's interior were dated 290.6 ± 2.6 Ma by a geochronological sample of Youbi et al. (2018) of the same section. The stratigraphy and position of KHE6, however, were difficult to estimate in the field (Fig. 1.10). Therefore, the paleomagnetic results from this site have been excluded (Table 1.8).

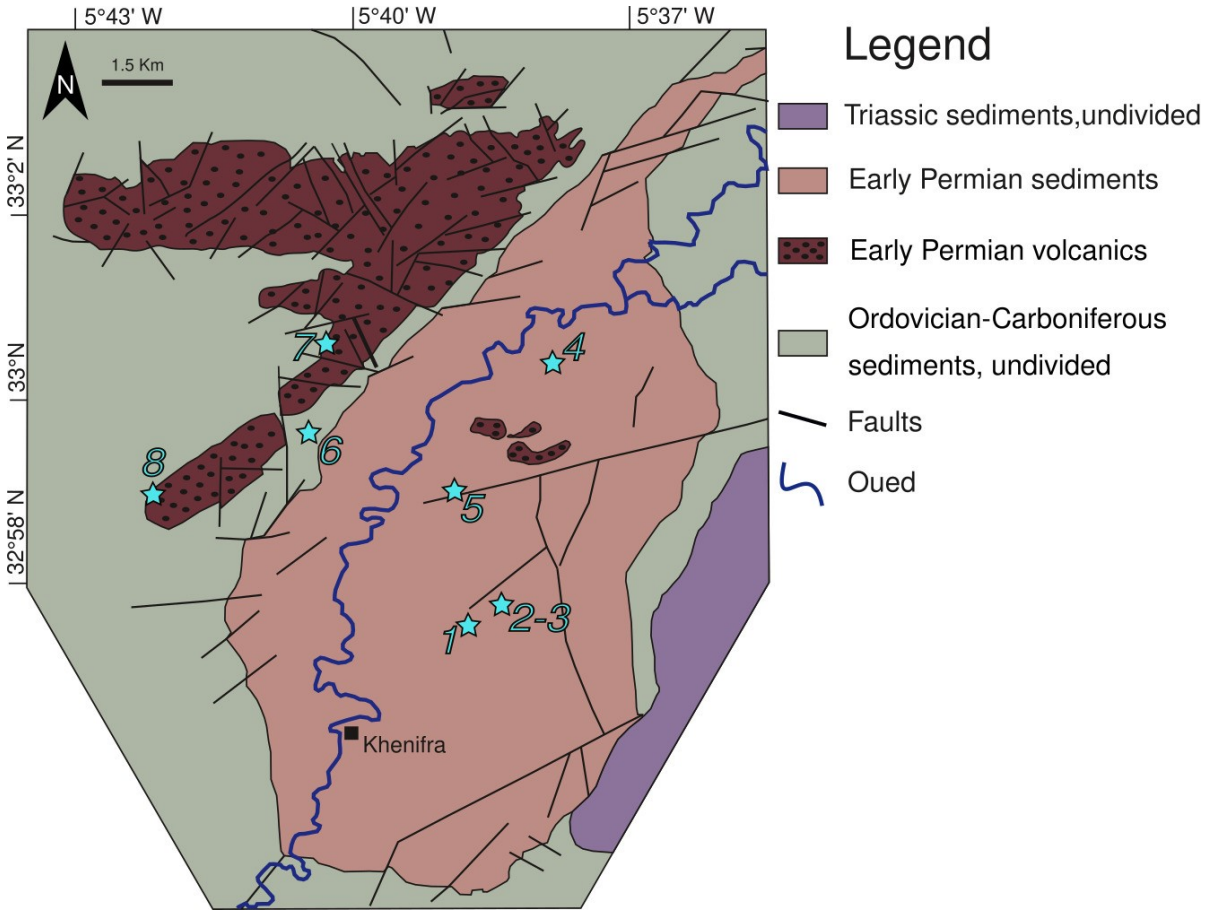

Figure 1.10: Simplified geological map of the Khenifra basin (KHE), redrawn and modified after Domeier et al. (2021). Light blue stars specify this work's paleomagnetic site positions from Khenifra. Numbering of samples correlate with Table 1.8. For further explanations see legend. This figure is located in the supplementary materials in the original publication.

1.3.8 Tiddas-Souk Es-Sebt des Ait Ikko (Tsesdai / TID)

The Tiddas (TID) basin, about 110 km to the SE of Rabat, is located in the Khemisset region and represents the third largest Late Paleozoic continental trough in the northern Central Moroccan Meseta (Figs. 1.1, 1.11). It is about 20 km long and 2-3 km wide and shows a volcano-sedimentary reddish-violet succession of Permian rocks that rest unconformably on Visean marine sediments and are covered by Triassic and Cenozoic deposits (e. g. Cailleux et al., 1983; El Wartiti et al., 1990; Hadimi et al., 2021; Larhrib, 1996; Voigt et al., 2011a).

Table 1.8: *Summary of important site characteristics and paleomagnetic results from the basin of Khenifra (KHE) for the high-stability component (Component B), all in all 45 specimens from 8 sites have been used. At the end, sites reported in Domeier et al. (2021) - namely GB2, GB3, TA1, TG1, TG2 as well as TM1 - and Martin et al. (1978), with site M10, are listed and combined with this study's data for reference. TM1 is originally dated 305.59 ± 2.68 Ma by Domeier et al. (2021) but is only based on two concordant ages and one slightly discordant age (out of 26 grains analyzed), represents an outlier in available age models and is therefore excluded when calculating the arithmetic mean of KHE. For details see text and caption of Table 1.1. This table is located in the supplementary materials in the original publication.*

	Site characteristics							In situ (geographic)				Tectonic (bedding corrected)			
Name	n/N	Age [Ma]	Lithology	Dip Dir. [°]	Dip [°]	GLat [°N]	GLon [°E]	Dec [°]	Inc [°]	a95 [°]	k	Dec [°]	Inc [°]	a95 [°]	k
KHE1	6/6	298.89 – 280.57	Red beds	303	24	32.958069	-5.644138	125.3	-23.5	11.7	33.6	125.1	0.5	11.7	33.6
KHE2	6/6	298.89 – 280.57	Red beds	297	28	32.964239	-5.639395	135.4	-17.7	1.6	1811.1	134.7	9	1.6	1811.1
KHE3	6/6	298.89 – 280.57	Red beds	339	30	32.964913	-5.638808	131.3	-17.1	3	490.1	132.2	9.7	3	490.1
KHE4	5/6	298.89 – 280.57	Red beds	130	15	33.007363	-5.630850	124.5	0.6	10.4	54.9	124.4	-14.4	10.4	54.9
KHE5	6/6	298.89 – 280.57	Red beds	345	10	32.982586	-5.647526	135.7	-12.6	4.8	195.4	136.4	-3.8	4.8	195.4
KHE6^{O}*	6/6	290.6 ± 2.6	Rhyolite	5	62	32.994448	-5.673385	261.5	-62.5	2.4	783.8	213.3	-18.8	2.4	783.8
KHE7	6/7	290.6 ± 2.6	Rhyolite	210	52	32.994649	-5.673316	130.9	-10.4	9.4	51.5	118.4	-14.9	9.4	51.5
KHE8^{O}*	4/6	290.6 ± 2.6	Rhyolite	210	52	32.981675	-5.701036	349.4	31.6	18.8	24.8	298.4	56.3	18.8	24.8
Mean	**6/8**	**297.9 – 281.8**	**-**	**-**	**-**	**32.98**	**354.35**	**130.5**	**-13.5**	**7.8**	**73.9**	**128.6**	**-2.3**	**10.7**	**39.8**
GB2*	2/5	282.76 ± 2.19	Tuff	359.3	20.2	32.981	-5.701	124.7	6.9	22.3	12.8	120.9	18.1	22.3	12.8
GB3	4/4	282.76 ± 2.19	Andesite	359.3	20.2	32.981	-5.701	118.6	-16.6	12.4	55.8	122.1	-6.1	12.4	55.8
TA1	8/8	282.76 ± 2.19	Andesite	27.3	11.0	32.999	-5.685	126.3	-14.6	6.5	74	129	-12.6	6.5	74
TG1	5/8	295.1 ± 2.9	Dacite	154.0	10.3	32.995	-5.643	138.7	-1.2	5	245.4	138.4	-11.2	5	245.4
TG2	5/8	295.1 ± 2.9	Dacite	114.3	9.7	32.994	-5.643	169.9	12.9	10.7	55.7	168.5	7.3	10.7	55.7
TM1	8/8	305.59 ± 2.68*	Andesite	268.2	33.1	33.025	-5.664	129.4	-12.5	3.8	212.5	129.4	12.7	3.8	212.5
Mean VW+DO	**11/14**	**295.4 – 283.6**	**-**	**-**	**-**	**32.99**	**354.35**	**133.1**	**-10.5**	**9.6**	**23.8**	**132.4**	**-2.2**	**9.7**	**23.2**
M10	?/?	298.89 – 280.57	Red beds	?	?	33.5	-6.5	?	?	?	?	120.6	3.6	7.8	?
Mean all	**12/15**	**295.7 – 283.4**	**-**	**-**	**-**	**33.03**	**354.27**	-	-	-	-	**131.4**	**-1.7**	**9**	**24.1**

The cumulative maximum thickness of the Permian red bed succession has been disputable, ranging from 180 m (Aassoumi et al., 1992; Aassoumi and Vozenin-Serra, 1996; El Wartiti, 1981; El Wartiti et al., 1986; El Wartiti et al., 1990; Zouine, 1986) to 500 m (Broutin et al., 1998; El Wartiti, 1996) but was finally established to not exceed 300 m (Larhrib, 1996). The stratigraphy of TID, generally incomplete due to faulting, is characterized by three red-beds formations (Hadimi et al., 2021; Larhrib, 1988; Larhrib, 1996): a lower formation (F1) represented by purple-red silty argillites, interbedded with polymictic, heterometric conglomerates, crudely horizontal or cross-bedded sandstone and laminated to massive mudstones with minor intercalations of coal, limestone, and volcanic tuff (Fig 1.3k; about 100 meter-thick); an intermediate formation (F2), consisting of planar to cross-bedded silty argillites alternated with channelized deposits (about 120 m thick) and an upper formation (F3) characterized by red silty argillites interspersed with sandstone (50 to 80 meter-thick).

The Permian age of these formations was initially constrained using plant remains of early to late Permian affinities (Broutin et al., 1998). A recently found rich tetrapod footprint assemblage (Voigt et al., 2011a) ties the succession more precisely to the Artinskian – Kungurian (i.e. 290.51 - 274.37 Ma; Henderson et al., 2020) (Table 1.9).

The effusive and subintrusive magmatic units of TID consist of andesitic to dacitic flows and rhyolitic domes with associated rhyolitic dikes. In this context, three major volcanic pulses were distinguished (Hadimi et al., 2021): the first one (mainly andesitic) predates the Permian series; the second pulse is synsedimentary, displays different petrographic characteristics and is remarkable for its andesitic lava flows interbedded with the siliciclastic deposits. The third pulse of intrusive rhyolitic dykes is linked to the Ari el Mahsar rhyolitic dome emplacement and the dacitic flows. For the last volcanic pulse, a Sensitive High-Resolution Ion Microprobe (SHRIMP) gave a concordant U-Pb age of zircon age as 286.4 ± 4.7 Ma which is also assessed valid for our volcanic samples from TID (Fig. 1.2, Table 1.9; Hadimi et al., 2021).

In the Tiddas basin, we sampled 11 different sites (nine red beds and two andesites) and generated 73 drill cores, one drill core lost its orientation, which is why 72 paleomagnetic samples could be obtained for TID (Fig. 1.11, Table 1.9).

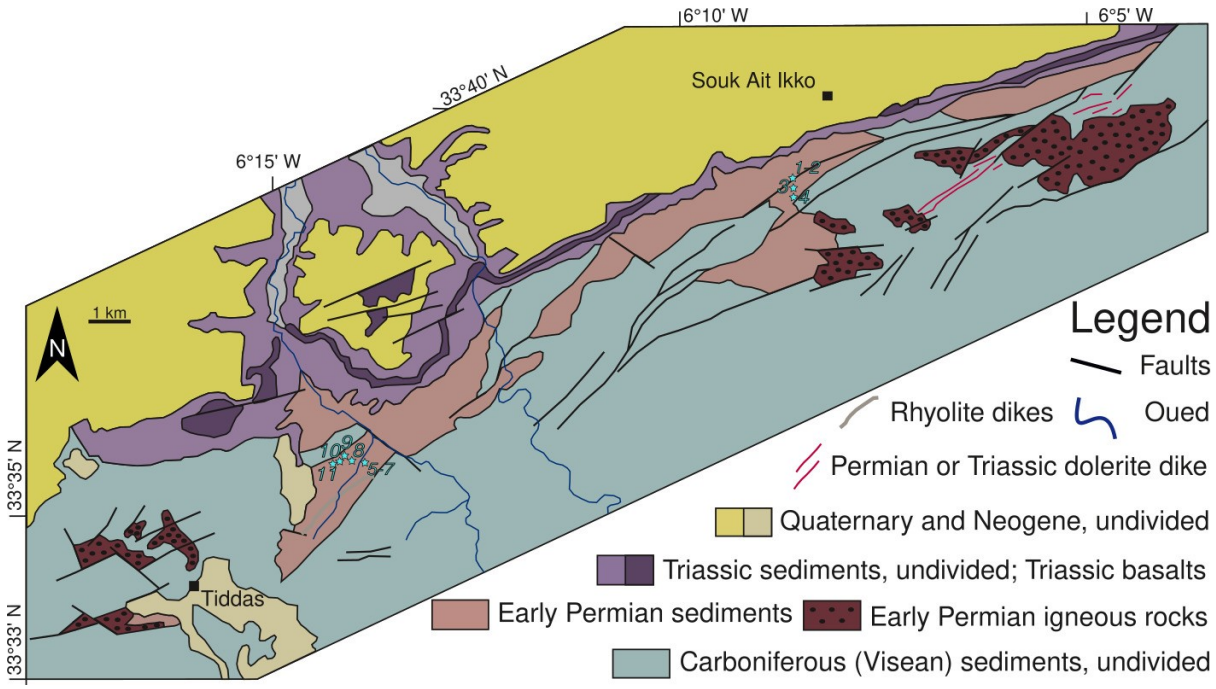

Figure 1.11: Simplified geological map of the Tiddas basin (TID), redrawn and modified after Domeier et al. (2021). Light blue stars specify this work's paleomagnetic site positions. Numbering of samples correlate with Table 1.9. For further explanations see legend. This figure is located in the supplementary materials in the original publication.

1.3.9 Bou Achouch (BOUA)

BOUA is a comparatively small (~1 km^2) basin located in the northeast of the Central Massif (Figs. 1.1, 1.12) and is represented by a volcano-sedimentary succession only 40 m thick. It unconformably overlays the upper Visean-Namurian basement and is unconformably capped by Neogene deposits (Cailleux et al., 1983; El Wartiti et al., 1990).

Two groups of rocks can be distinguished: detritic rocks (conglomerates, silt- and sandstones) and volcanic rocks with calc-alkaline affinity (andesites and rhyolites). The latter crops out in different ways: as lava flows, pyroclastic deposits (e.g., tuffs) and dikes. The petrographic characteristics of the Carboniferous volcanic rocks of BOUA show great similarities with those of TID (El Wartiti et al., 1990) and KHE (Youbi, 1998). A first volcanic episode (mainly rhyolites) crops out in the NE part together with cinerites and fine-grained sediments (El Wartiti et al., 1990). They are overlain by coarser-grained deposits, rich in volcanic pebbles. At the top of the succession a mainly andesitic volcanic episode occurs (Fig. 1.2).

A rich macroflora assemblage was recovered from the finer grained clastic units (Broutin et al., 1998) and permitted to link these sediments to the Kungurian. Subsequently,

Kerp et al. (2001) shifted this age constraint to the latest Carboniferous on the basis of similarities between the BOUA floras and those of the Lower Rotliegend of the Saar-Nahe Basin in Germany. The only available geochronological constraint from BOUA includes zircons where ~ 60% have ages which cluster around ~ 300 Ma, and the youngest part of this cluster provides a weighted mean $^{206}Pb/^{238}U$ age of 301.50 ± 1.24 (Domeier et al., 2021). This latest Carboniferous age supports the observations of Kerp et al. (2001) and is therefore esteemed more realistic than the formerly postulated Kungurian age.

In the basin of BOUA, we drilled 50 cores at seven sites, of which three were extracted from rhyolites and cinerites (tuff), respectively (Fig. 1.12, Table 1.10). Since the only available absolute age constraint is reported by Domeier et al. (2021) to be 301.50 ± 1.24 Ma, a corresponding age range is assumed for all studied sites (Table 1.10).

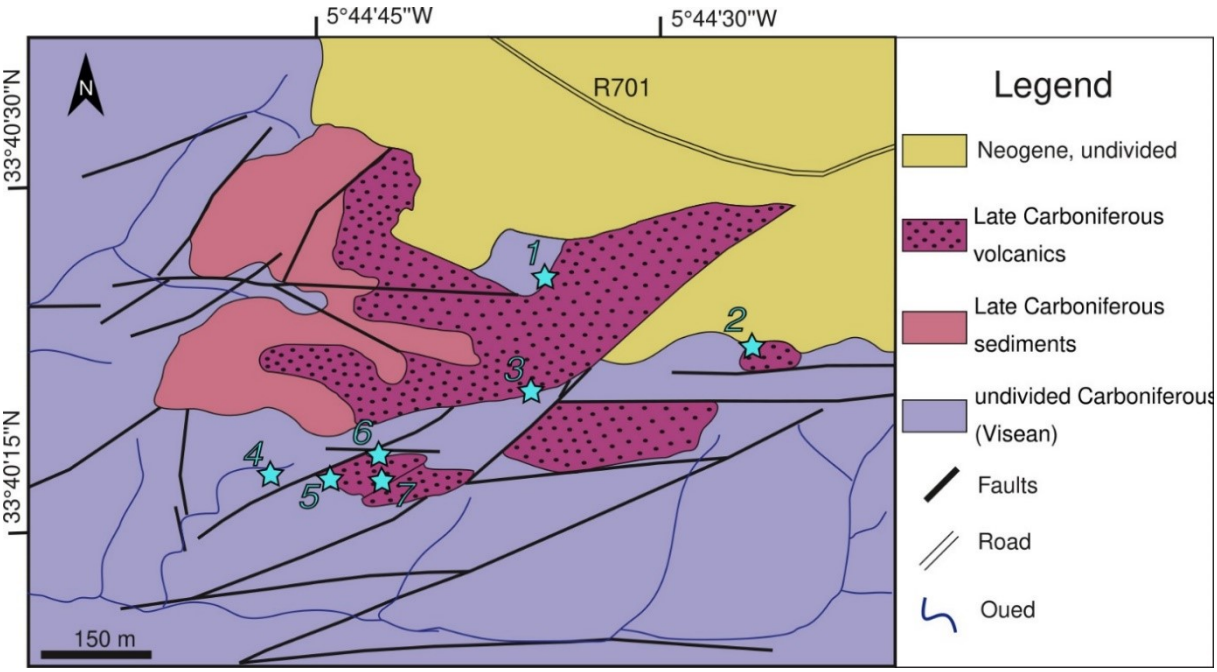

Figure 1.12: Simplified geological map of the basin of Bou Achouch (BOUA), redrawn and modified after Domeier et al. (2021). Light blue stars specify the paleomagnetic site positions of this work. Numbering of samples correlate with Table 1.10. For further explanations see legend. This figure is located in the supplementary materials in the original publication.

Table 1.9: *Summary of important site characteristics and paleomagnetic results from the basin of Tiddas (TID) for Component B, all in all 71 specimens from 11 sites have been used. At the end, sites reported in Domeier et al. (2021) - namely TL1, SA1 and SA2 - are listed and combined with this study's data for reference. For details see text and caption of Table 1.1. This table is located in the supplementary materials in the original publication.*

	Site characteristics							In situ (geographic)				Tectonic (bedding corrected)			
Name	n/N	Age [Ma]	Lithology	Dip Dir. [°]	Dip [°]	GLat [°N]	GLon [°E]	Dec [°]	Inc [°]	a95 [°]	k	Dec [°]	Inc [°]	a95 [°]	k
TID1	8/8	286 ± 4.7	Andesite	145	22	33.651003	-6.144460	168.4	9.9	6	85.7	168.4	-10.3	6	85.7
TID2	6/6	286 ± 4.7	Andesite	145	22	33.651143	-6.144298	172.6	11.7	6.5	108	172.2	-7.9	6.5	108
TID3	8/8	290.51 – 274.37	Red beds	70	23	33.649721	-6.145095	155.8	9.9	9.3	36.6	152.3	7.4	9.3	36.6
TID4	6/6	290.51 – 274.37	Red beds	130	17	33.648065	-6.144856	152	2.9	4.2	261.6	152.6	-12.8	4.2	261.6
TID5	6/6	290.51 – 274.37	Red beds	140	15	33.597069	-6.231418	134	-2.1	7.3	85.3	133.7	-17.1	7.3	85.3
TID6	8/8	290.51 – 274.37	Red beds	140	15	33.597069	-6.231418	140.2	6.4	9.6	34	140.2	-8.6	9.6	34
TID7	5/6	290.51 – 274.37	Red beds	140	15	33.597069	-6.231418	146.4	5.9	4.4	309.9	146.4	-9	4.4	309.9
TID8	6/6	290.51 – 274.37	Red beds	140	15	33.597214	-6.231867	142.2	-0.2	2.9	536.3	142.3	-15.2	2.9	536.3
TID9	6/6	290.51 – 274.37	Red beds	142	30	33.597478	-6.232597	143.5	16.2	4.3	245.7	143.4	-13.8	4.3	245.7
TID10	6/6	290.51 – 274.37	Red beds	142	30	33.597457	-6.232596	147.8	29.8	7.1	90.9	147	-0.1	7.1	90.9
TID11	6/6	290.51 – 274.37	Red beds	142	30	33.597551	-6.233221	143.8	24	4.8	193.8	143.6	-6	4.8	193.8
Mean	**11/11**	**290.6 – 275.7**	**-**	**-**	**-**	**33.62**	**353.8**	**149.6**	**10.6**	**8.7**	**28.6**	**149.3**	**-8.7**	**7.7**	**36.2**
TL1	13/13	286 ± 4.7	Andesite	341.8	9.5	33.579	-6.271	134.2	-20.1	5	70.6	135.4	-11.6	5	70.6
SA1	6/6	286 ± 4.7	Rhyolite	0	0	33.655	-6.075	138.1	14.3	10.7	40.1	138.1	14.3	10.7	40.1
SA2	8/8	286 ± 4.7	Dacite	220.7	11.5	33.643	-6.133	158.6	3.6	7.7	52.9	158.8	-1.8	7.7	52.9
Mean VW+DO	**14/14**	**290.7 – 277.0**	**-**	**-**	**-**	**33.62**	**353.8**	**148.4**	**8.2**	**8.3**	**23.7**	**148.2**	**-6.8**	**7.2**	**31.4**

Table 1.10: *Summary of important site characteristics and paleomagnetic results from the basin of Bou Achouch (BOUA) for Component B, all in all 46 specimens from 7 sites have been used. At the end, site BA1 reported in Domeier et al. (2021) is listed and combined with this study's data for reference. For details see text and caption of Table 1.1. This table is located in the supplementary materials in the original publication.*

	Site characteristics							In situ (geographic)				Tectonic (bedding corrected)			
Name	n/N	Age [Ma]	Lithology	Dip Dir. [°]	Dip [°]	GLat [°N]	GLon [°E]	Dec [°]	Inc [°]	a95 [°]	k	Dec [°]	Inc [°]	a95 [°]	k
BOUA1	8/8	301.50 ± 1.24	Rhyolite	0	0	33.674062	-5.742887	161.2	26	4.6	149	161.2	26	4.6	149
BOUA2*	8/8	301.50 ± 1.24	Rhyolite	0	0	33.673265	-5.740344	180.4	-6.3	18.2	10.2	180.4	-6.3	18.2	10.2
BOUA3	6/6	301.50 ± 1.24	Rhyolite	138	12	33.672726	-5.743453	140.1	12.2	11.1	37.3	140.1	0.3	11.1	37.3
BOUA4*	4/8	301.50 ± 1.24	Tuff	140	43	33.671407	-5.746438	247.3	-25	29.3	10.8	259.4	-7.2	29.3	10.8
BOUA5	7/7	301.50 ± 1.24	Tuff	125	8	33.671352	-5.745928	162.7	-2.5	12.2	25.4	163.2	-8.8	12.2	25.4
BOUA6	7/7	301.50 ± 1.24	Tuff	155	25	33.671724	-5.745256	183.4	16.1	11.5	28.6	182.4	-6.1	11.5	28.6
BOUA7	6/6	301.50 ± 1.24	Rhyolite	155	25	33.671544	-5.745242	141.5	11.4	15	20.8	141.4	-13	15	20.8
Mean*	**5/7**	**302.74 - 300.26**	**-**	**-**	**-**	**33.67**	**354.26**	**157.6**	**13.1**	**19.5**	**16.4**	**157.5**	**-0.5**	**22.8**	**12.2**
BA1	10/11	301.50 ± 1.24	Andesite	90	18.7	33.673	-5.743	171	14.8	4.8	104.1	166.7	11.2	4.8	104.1
MeanVW+DO*	**6/8**	**302.74 - 300.26**	**-**	**-**	**-**	**33.67**	**354.26**	**159.9**	**13.5**	**15.9**	**18.8**	**159.1**	**1.6**	**18.5**	**14.1**

1.4 Additional Paleomagnetic Data

1.4.1 Methodology

All samples were extracted using a portable petrol-powered water-cooled rock-drill and oriented with a standard magnetic Brunton compass and an inclinometer in the field. Then, they were cut into cylindrical specimens of about 1-inch diameter and a volume of about 10 cm^3 at the Department of Earth- and Environmental sciences of the Ludwig-Maximilians-University of Munich. When possible, several specimens from one sample core were generated and labelled alphabetically from the top to the bottom of the core. Broken specimens have been fixed with heat-resistant, non-magnetic glue. Finally, they have been subjected to demagnetization and paleomagnetic measurements in a magnetically shielded room in the Department of Environmental- and Geosciences in Munich.

After detailed pilot studies applying alternating field (AF) and thermal demagnetization procedures, most of the samples were thermally demagnetized using an ASC oven (ASC Scientific Model TD-48, Thermal Specimen Demagnetizer). Paleomagnetic measurements were carried out using the SushiBar, an automated sample handling system integrated with a three axis, 2G Enterprises superconducting rock magnetometer (Wack and Gilder, 2012). After each heating step, the specimens were allowed to cool down in magnetically field free space and their remanent magnetization was measured on the three axis 2G cryogenic magnetometer.

Paleomagnetic data analysis was carried out using an online multi-platform tool with an open source environment (Paleomagnetism.org - Koymans et al., 2016), its recent update (Koymans et al., 2020) and the software Palaeomag-Tools from Hounslow (2006). Directional data is presented via orthogonal vector diagrams (Zijderveld, 1967) on equal area projections and analyzed by applying a least square method (Kirschvink, 1980) on linear parts of the demagnetization plots defined by a minimum of three successive demagnetization steps. The linear segments were anchored to the point of origin when appropriate. Subsequent statistical analysis of the results was carried out after Fisher (1953) and included the calculation of mean directions as well as virtual geomagnetic poles and paleopoles. Furthermore, parametric bootstrap fold tests (Tauxe and Watson, 1994), incremental fold tests (Watson and Enkin, 1993) and inclination-based fold tests (based on “inclination-only” and “block-rotation fisher” analysis) (Enkin and Watson, 1996) have been routinely applied to all site mean data. In addition the data sets have been subjected to the quantile-quantile method (Fisher et al., 1993) in order to test whether the respective paleomagnetic data fulfils the criterion of a Fisher

distribution. For further visualization of acquired data in the shown figures, GMAP2015 (Torsvik et al., 2015), GMT (Wessel et al., 2019) and GPlates (Müller et al., 2018) have been utilized.

In order to check the magnetic mineralogy, rock magnetic measurements were conducted on leftovers of the paleomagnetic samples (at least one per site with 5mm diameter). Hysteresis loops, backfield curves and thermomagnetic curves were determined for each of the sites using an MM VFTB (Munich Measurement Limited Variable Field Translation Balance; Krása et al., 2007) and a one-component Lakeshore Vibrating Sample Magnetometer (VSM) (general principle after Foner, 1959). Additionally, an isothermal remanent magnetization (IRM) of up to 2.5 T was imparted on selected samples using a MMPM10 Pulse Magnetizer. The rock magnetic data was visualized with a custom-made MATLAB code.

1.4.2 Results

1.4.2.1 Rock Magnetic Results

Since the rock magnetic behavior is not basin-specific but lithology controlled, we split the 97 sampled sites into groups of characteristic rock types (Fig. 1.13). 50 sites (from seven basins) from volcanic rocks are subdivided into mafic outcrops (group I), rhyolitic rocks (group II) and two endmembers for andesitic samples (groups III and IV). Another 47 sites (from seven basins) are from sedimentary rocks, mostly medium-grained red beds (group V).

Mafic samples display sharp-shouldered hysteresis loops indicative of a single low-coercivity ferrimagnetic component (Fig. 1.13 Ic), IRMs with sharp increase up to 100 mT and approximate saturation at 1 T (Fig. 1.13 Ib) and thermomagnetic curves with steady loss of magnetization and unblocking temperatures at ~ 580°C and occasionally around 200°C (Fig. 1.13 Ia) reflecting the occurrence of magnetite as the main magnetic carrier and potential relevance of maghemite in minor proportions.

The group of rhyolites shows broadly shouldered and wasp-waisted hysteresis loops (Fig. 1.13 IIc) and IRMs with steep magnetization increase up to 100 mT followed by a gradual increase up to 2.5 T without reaching saturation (Fig. 1.13 IIb) hence pointing towards the presence of a high and a low coercive magnetic mineralogical component. Corresponding thermomagnetic curves mostly show a distinct inflection of the heating branch at around Tc1 ~ 580°C, a less pronounced intensity drop at Tc2 ~ 650° as well as a much lower magnetization acquisition during cooling below 570°C (Fig. 1.13 IIa). This probably reflects a potential

breakdown of primary maghemite to hematite plus the presence of magnetite and hematite as magnetic carriers.

Andesitic specimens reveal a broad spectrum of rock magnetic properties and typical endmember cases (groups III and IV) are shown in Figure 1.13. On the one hand, most of the andesites are characterized by wasp-waisted hysteresis loops (Fig. 1.13 IIIc), IRM curves with a steep increase in magnetic intensity up to 100mT and then a gradual increase up to 2.5 T without saturating (Fig. 1.13 IIIb) and reversible thermomagnetic curves with two distinct inflections at Tc1 ~ 570°C and Tc2 ~ 680°C (Fig. 1.13 IIIa) thus suggesting alternating combinations of magnetite and hematite. On the other hand, a significant part of the andesitic volcanic rocks exhibits wide-shouldered hysteresis branches (Fig. 1.13 IVc), IRMs with a steady increase in magnetization approaching saturation at 2.5 T (Fig. 1.13 IVb) and reversible thermomagnetic curves with Tc ~ 660°C (Fig. 1.13 IVa) which we ascribe to the sole prevalence of hematite in these samples. Similar rock-magnetic findings for early Permian andesites from Morocco are also reported by Domeier et al. (2021).

The rock-magnetic properties of the red beds are mostly dominated by wide-shouldered hysteresis loops (Fig. 1.13 Vc) with high coercivities, IRMs with almost no magnetization acquisition up to 250 mT and a subsequent steady increase up to 2.5 T without reaching saturation (Fig. 1.13 Vb) and reversible thermomagnetic curves with a distinct inflection around Tc ~ 650-660°C. Additionally, low and medium temperature components are present to a minor extent (Fig. 1.13 Va). The red bed's magnetic mineralogy is therefore uniformly characterized by the predominance of hematite with the addition of minor amounts of goethite and potentially pyrrhotite.

1.4.2.2 Paleomagnetic Results

Demagnetization Behavior of the NRM

Figure 1.14 shows representative orthogonal projection diagrams (Zijderveld, 1967) of all sampled basins and lithologies sorted from south to north according to the geographic position of the basins shown in Figures 1.1 and 1.2. Since AF demagnetization experiments on pilot samples rendered either ineffective due to high presence of hematite within the sampled basins (Fig. 1.13) or produced comparable results to its heated counterpart (e. g. Fig. 1.14e vs. Fig. 1.14f), thermal demagnetization was predominantly used to isolate characteristic directions of the NRM.

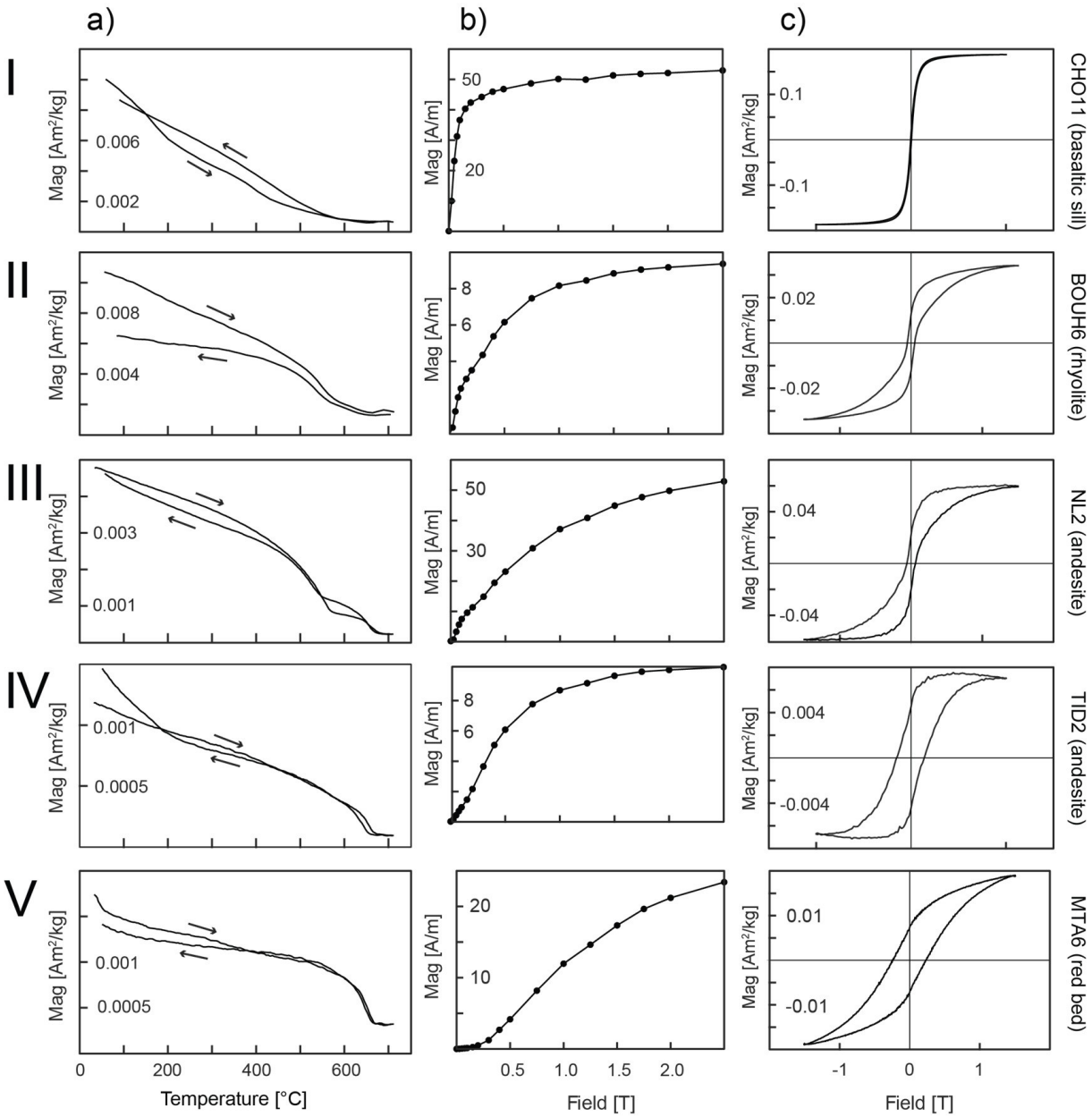

Figure 1.13: Representative rock magnetic results subdivided according to lithology, where groups I-IV were derived from volcanic samples of various affinities and group V emanates from sedimentary samples, predominantly red beds. For each category, thermomagnetic curves (a), IRM-curves (b) and hysteresis-loops (c) are provided. Arrows specify heating and cooling cycles of thermomagnetic curves.

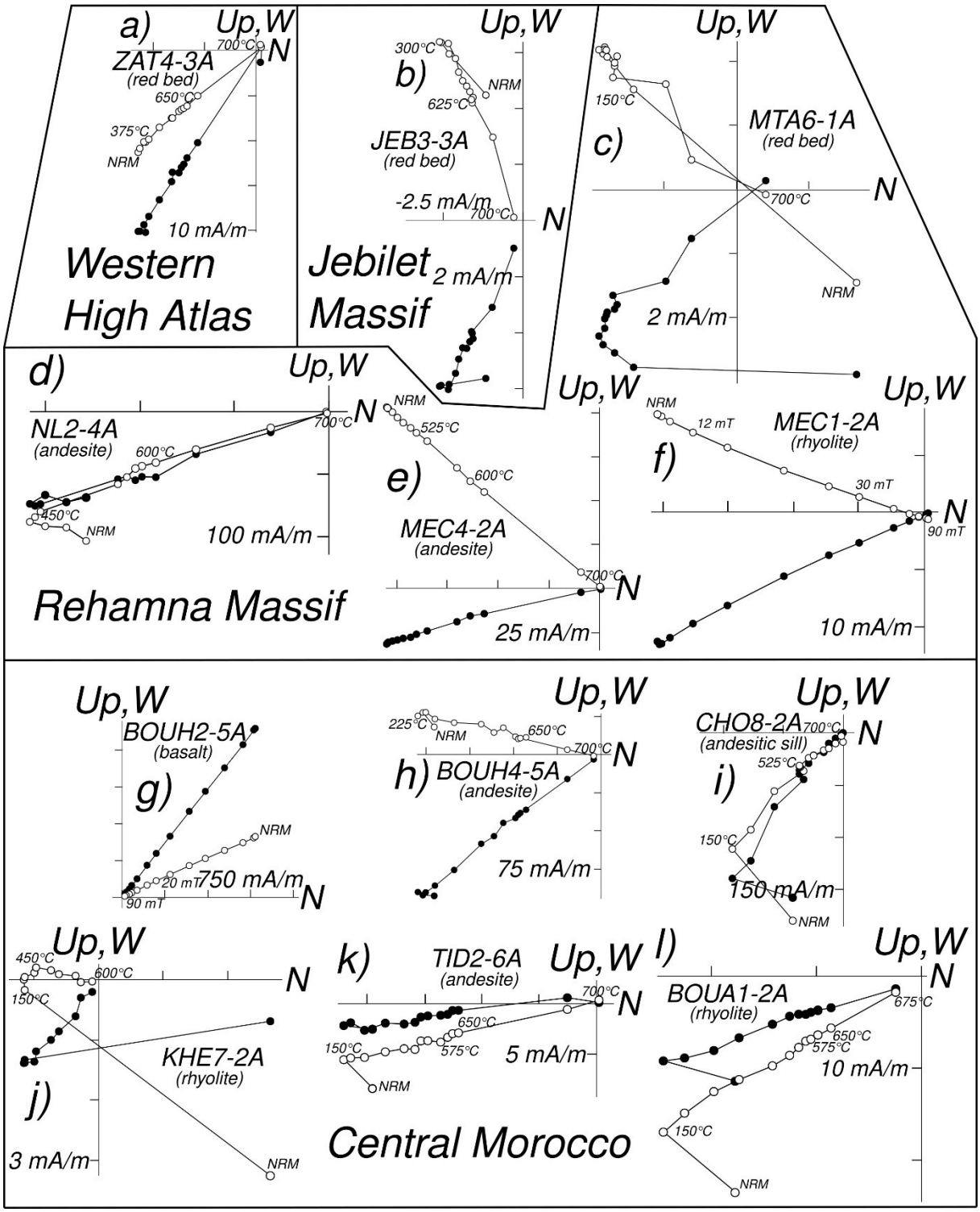

Figure 1.14: Paleomagnetic results of demagnetization experiments of representative samples plotted as orthogonal vector diagrams after Zijderveld (1967) in geographic (in situ) coordinates. Solid (open) dots describe the vector endpoints projected onto the horizontal (vertical) plane and some of them are labelled with their respective demagnetization steps (in [mT] for AF demagnetization and in [°C] for thermal demagnetization) or the NRM.

While some samples exhibit straightforward unidirectional behavior (Figs. 1.14a, 1.14e, 1.14f, 1.14g), a majority is characterized by two distinct directional components, where the Low Temperature Component (LTC) or Component A, is typically isolated below 300°C and covers variable proportions of the respective NRM (Figs. 1.14b, 1.14c, 1.14d, 1.14h-l). Upon further demagnetization, the magnitude of the High Temperature Component (HTC) or Component B is gradually removed and trajectories of the magnetic vectors trend towards the origin while trespassing unblocking temperatures corresponding to the underlying rock magnetic mineralogy (Fig. 1.13). Accordingly, a "hematite unblocking spectrum" between 625°C and 700°C can be observed in the red beds (Figs. 1.14a-c). Demagnetization ranges diagnostic for magnetite characterize the mafic volcanic rocks (Fig. 1.14g) and some rhyolites (Figs. 1.14f and 1.14j). A broader unblocking interval is evident for rhyolites and andesitic sills linked to a higher amount of hematite (Figs. 1.14i and 1.14l). Ultimately, all andesites are associated with a striking unblocking spectrum at high temperatures beyond 625°C indicating the prevalence of hematite and unblocking spectra of differing width at intermediate temperatures between 450°C and 575°C highlighting the variable influence of magnetite (Figs. 1.14d, 1.14e, 1.14h, 1.14k).

Notably, the demagnetization behavior of both magnetic components does not significantly vary across the sampled basins, where both the low stability component (if present) and the high-stability component are more or less collinear. Almost all of the samples are of reversed polarity consistent with their suggested late Carboniferous to early Permian age which falls within the Kiaman reversed superchron spanning from the mid-Bashkirian (about 318 Ma; Aretz et al., 2020; Hounslow, 2022) to the Early Wordian (around 267 Ma; Hounslow and Balabanov, 2018). However, a small number of drill cores (11 samples from 3 sites in total) are characterized by a strong and stable remanence of normal polarity (Fig. 1.14g), which can be correlated to one of the normal magnetozones within the Kiaman reversed superchron (Hounslow and Balabanov, 2018).

Mean Directions

Component A mean directions and their averaged overall mean direction are clustering around the recent geomagnetic field for the sampling area (D = 358.4°, I = 44.1°; using IGRF2020 model: https://www.ngdc.noaa.gov/geomag/calculators/magcalc.shtml#igrfwmm visited on July 20th, 2022) and is therefore interpreted to be of secondary origin (Fig. 1.15).

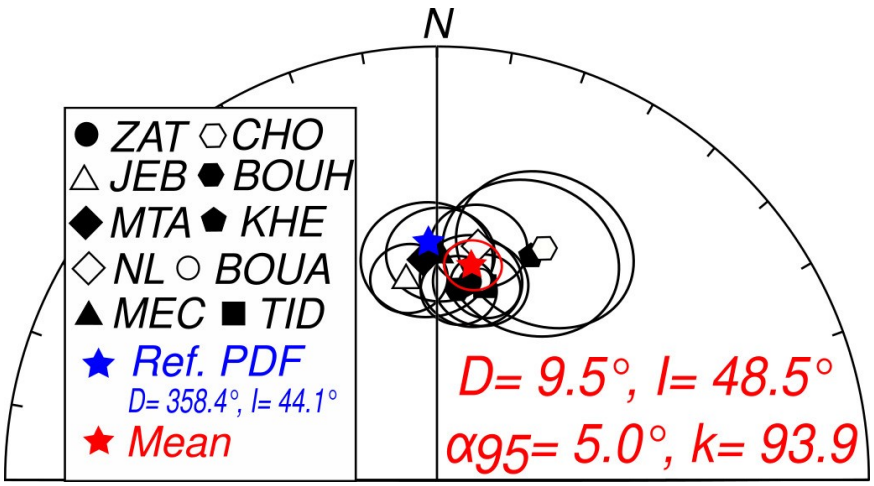

Figure 1.15: Stereographic projection of the individual basins' low temperature paleomagnetic mean directions (black symbols associated with respective basins are given in the inset) in geographic (in situ) coordinates surrounded by their corresponding α_{95} confidence intervals (black circles). The referential present-day field (PDF) for the sampling area in Morocco is visualized by a blue star and given in the inset, as well. The overall mean direction of all basins is marked by a red star and related quantities like mean declination, mean inclination as well as Fisher (1953) parameters (α_{95} and k) are given within the stereoplot. α_{95} is the fisher angle of half cone of 95% confidence around the mean direction and k is the fisher precision parameter of the mean direction.

The high-stability component or component B generally falls within the SE quadrant of the stereographic equal-area projection, with declinations ranging from ESE to S and shallow to moderate inclinations that are rotated towards the horizontal upon applying tectonic correction thereby minimizing potential inclination shallowing effects. Mean directions of Late Paleozoic Moroccan sites and basins from this study as well as available literature data reported by Daly and Pozzi (1976), Martin et al. (1978), Westphal et al. (1979) and Domeier et al. (2021) are listed in Tables 1.1 – 1.11 and shown in the left panel of Fig. 1.16.

Some site-mean directions (MTA1, CHO1 and BOUH2) point down and towards NW, clearly antipodal to the dominating SE and up component observed elsewhere (Figs. 1.16c, 1.16f, 1.16g). While MTA1 consists only of one paleomagnetic direction and CHO1 is poorly constrained (α_{95} = 20.3°), BOUH2 displays a well-defined (α_{95} = 4.9°, k = 244.6) site mean-direction (D = 303.4°, I = -13.7° in geographic coordinates and D = 306.1°, I = -3.7° in tectonic coordinates) which robustly reflects a geomagnetic reversal.

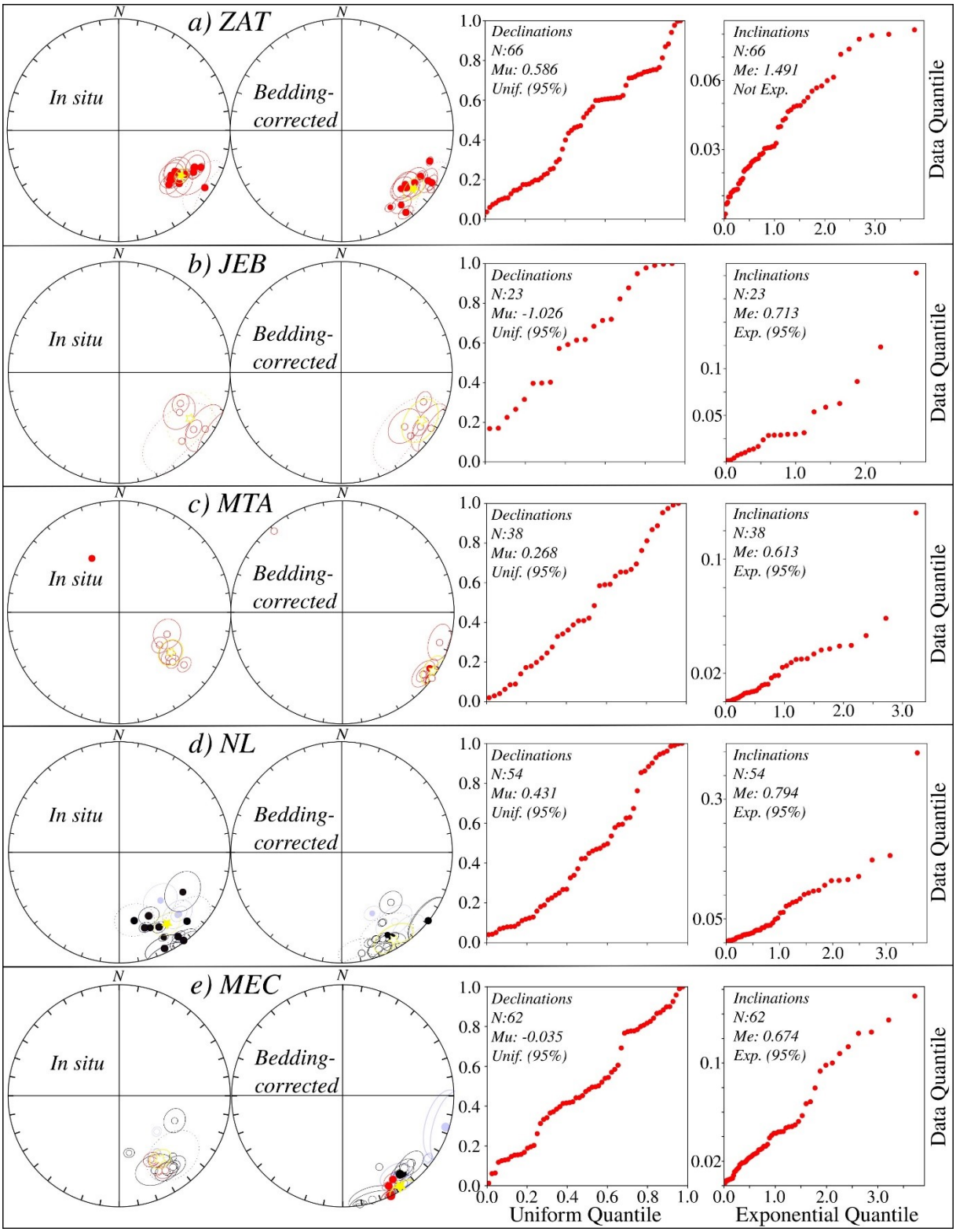

Figure 1.16: Left panel - Stereographic equal-area projection of site-mean (circles) and basin-mean (yellow stars) directions in geographic (in situ) and tectonic (bedding-corrected) coordinates. Contours around the circles (stars) define the α_{95} Fisher (1953) angles of half cone of 95% confidence around the mean direction of respective sites (basins). Black (red) circles show site-mean stereographic projections of paleomagnetic data derived from volcanic (sedimentary) rocks whereas blue circles and 95% confidence ellipses reflect available data sets from the literature for respective basins. Data points with dotted contour lines have been discarded for further statistical analysis once reliability criteria of Van der Voo (1990) are not sufficiently met or respective data points are

identified as clear outliers. Solid (open) symbols represent projections in in the lower (upper) hemisphere, respectively. Numerical values for the shown data can be found in Tables 1.1 – 1.11. Right panel - Quantile-quantile diagram of declinations plotted against a reference uniform distribution (left) and inclinations drawn against an expected exponential distribution (right) taken from bedding-corrected paleomagnetic directions of this study's site-data after Fisher et al. (1993). If both test statistics M_u and M_e do not exceed the critical values of M_u = 1.207 and M_e = 1.094, the data is Fisher distributed at a 95% level of confidence.

A conspicuous feature also noticed by Domeier et al. (2021) in their data set is the elongation of the site-mean declinations along small circles in most of the basins after tilt-correction (Fig. 1.16). Since there is no systemic directional difference between red beds and volcanics and both groups seem to be equally streaked, this rotational effect is no sedimentary feature but might rather reflect vertical axis rotations given the transpressive tectonic regime and abundance of dextral fault zones in the sampling area (chapter 1.3). Since rotated/elongated paleomagnetic data typically miss characteristic attributes of a Fisher distribution, we checked this integral requirement for further analysis by applying the quantile-quantile method described by Fisher et al. (1993) (right panel of Fig. 1.16). Site-mean directions of three basins (ZAT, KHE and BOUA) are not Fisher distributed, whereas NL and MEC statistically fulfil the requirements of a Fisher distribution but their tendency to form a girdle is visually evident (Figs. 1.16d and 1.16e). For the remaining basins, Fisher parameters improve after bedding-correction on the 95% significance level (Table 1.11).

Fold Tests

In order to constrain component B's relative magnetization age and to further investigate the potential influence of vertical axis rotations on our data set, we conducted an incremental fold test after Watson and Enkin (1993) and a parametric bootstrap fold test (Tauxe and Watson, 1994) – hereafter briefly called 'bulk fold tests" – as well as inclination-based fold tests following Enkin and Watson (1996), namely the inclination-only approach and BRF analysis, for every basin (Fig. 1.17). In general, the fold tests show similar behavior and can be subdivided into four different categories.

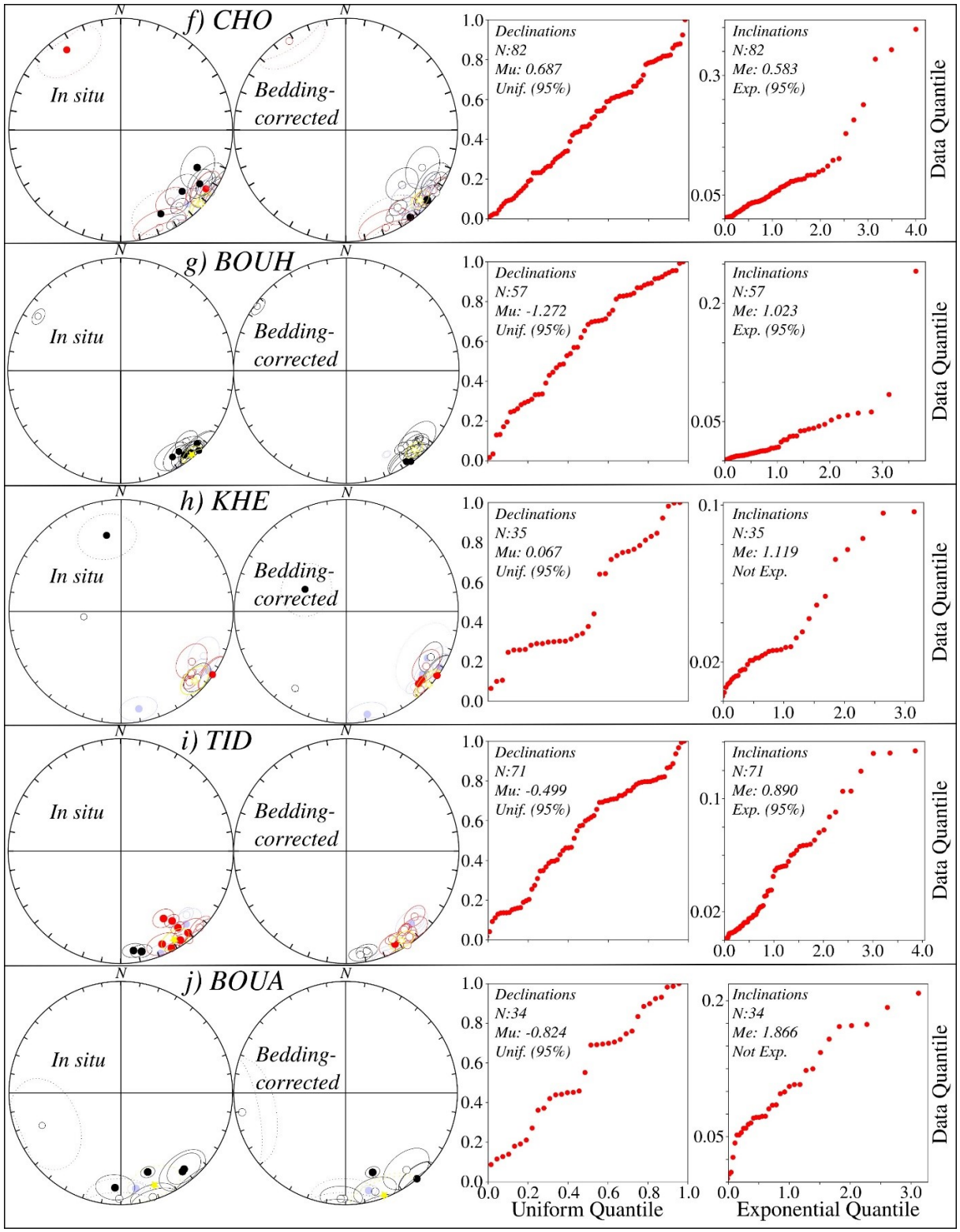

Figure 1.16 continued.

***Table 1.11**: Summary of paleomagnetic results for the high-stability component (Component B). Age ranges are based on paleontological and geochronological constraints as presented in section 1.3 and were determined calculating the arithmetic mean of the minimal and maximal age boundaries. See Tables 1.1 – 1.10 for more information. n/N: number n of site-mean directions included in the determination of the basin-mean direction/number N of measured sites. Glat/Glong: Averaged geographic position of sampled basins given in latitude/longitude. Declination (Dec), Inclination (Inc) as well as statistical parameters after Fisher (1953), i.e. k (precision parameter) and α_{95} (angle of half cone of 95% confidence), of mean directions for all basins are given in geographic and stratigraphic coordinates whenever available. Plat/Plon show basin-specific paleopole positions calculated from paleomagnetic data in stratigraphic coordinates, whereas A95 and K are related Fisher parameters. References: Reference data added to this study's results, [1]: Domeier et al. (2021); [2]: Westphal et al. (1979); [3]: Daly and Pozzi (1976); [4]: Martin et al. (1978).*

			Geographic coordinates						Stratigraphic coordinates				Pole position				References
Name	Age range [Ma]	n/N	Glat [°N]	Glong [°E]	Dec [°]	Inc [°]	α_{95} [°]	k	Dec [°]	Inc [°]	α_{95} [°]	k	Plat [°N]	Plon [°E]	A95 [°]	K	
Oued Zat (ZAT)	303.7 – 298.9	11/12	31.43	352.48	126	31.2	5.1	81.9	129.3	17.8	7.3	40	-26.8	51.3	6.8	46.4	-
Jebilet massif (JEB)	290.5 – 259.6	4/5	31.89	351.65	123	-24.4	17.2	29.6	121.6	-16.9	14	44	-31.3	71.9	11.2	68.4	-
M'Tal (MTA)	290.5 – 274.4	6/7	32.45	351.64	128.1	-40.9	9	56.1	122.8	-4.2	8.6	62.1	-28.4	64.5	7.1	90.9	-
Nzalt-Lararcha (NL)	277.7 – 276.5	9/11	32.27	352.34	149.3	20.1	10.8	23.8	150.3	-12.6	11.7	20.4	-52.2	46.1	8.7	35.7	-
		12/14	32.27	352.35	146.5	22.6	8.9	24.9	149	-9.2	12	14.2	-49.8	45.3	8	30.4	[1]
Mechraa Ben Abbou (MEC)	293.3 – 283.1	10/11	32.64	352.23	147.8	-30	9	29.8	150.6	1.5	9.3	27.8	-46.5	37.9	7.5	43	-
	293.0 – 284.2	14/15	32.65	352.22	147	-32.6	7.2	31.8	147.8	1	7.6	28.4	-45	41.2	6.1	42.8	[1]
	292.8 – 284.0	15/17	32.65	352.22	-	-	-	-	147.7	0.5	7.1	30.1	-45.1	41.5	5.7	45.8	[1], [2]
Chougrane (CHO)	307.5 – 286.2	12/14	32.99	353.71	132.8	-1.1	10.9	16.7	133.2	-9.9	8.6	26.4	-38.3	61.5	7.3	36.7	-
	308.1 – 287.0	14/16	32.98	353.7	132.5	-0.7	9.6	18.3	132.8	-10.6	7.5	29.3	-38.2	62.2	6.3	40.3	[1]
	308.0 – 286.9	17/19	32.98	353.7	-	-	-	-	133.2	-9.7	6.2	33.9	-38.2	61.4	5.3	46.6	[1], [2], [3]
El Had Bouhssoussene (BOUH)	298.5 – 264	11/11	33.16	353.93	138.5	2.4	6.4	51.6	138.1	-7.3	5.4	73.1	-41.1	56.1	4	132.8	-
		12/12	33.16	353.93	139.4	2.2	6.1	52.3	139.4	-8.3	5.7	58.4	-42.4	55.4	4.5	95.3	[1]
		13/13	33.08	353.94	-	-	-	-	139.2	-8.1	5.3	62.7	-42.2	55.5	4.1	102.3	[1], [3]
Khenifra (KHE)	297.9 – 281.8	6/8	32.98	354.35	130.5	-13.5	7.8	73.9	128.6	-2.3	10.7	39.8	-32.3	62	7.4	83.8	-
	295.4 – 283.6	11/14	32.99	354.35	133.1	-10.5	9.6	23.8	132.4	-2.2	9.7	23.2	-35.2	58.9	8.2	32.3	[1]
	295.7 – 283.4	12/15	33.03	354.27	-	-	-	-	131.4	-1.7	9	24.1	-34.4	59.4	7.6	33.4	[1], [4]
Tiddas (TID)	290.6 – 275.7	11/11	33.62	353.8	149.6	10.6	8.7	28.6	149.3	-8.7	7.7	36.2	-49.1	45	6.9	44.7	-
	290.7 – 277.0	14/14	33.62	353.8	148.4	8.2	8.3	23.7	148.2	-6.8	7.2	31.4	-47.6	45.3	6.1	42.9	[1]
Bou Achouch (BOUA)	302.7 – 300.3	5/7	33.67	354.26	157.6	13.1	19.5	16.4	157.5	-0.5	22.8	12.2	-50.3	31	18.6	17.9	-
		6/8	33.67	354.26	159.9	13.5	15.9	18.8	159.1	1.6	18.5	14.1	-50.2	28.1	15	21	[1]

In the first group, all fold tests rendered negative which only comprises the southernmost sampled basin ZAT (Figs. 1.17a and 1.17b). Secondly, areas JEB and TID exhibit positive parametric bootstrap fold tests (Figs. 1.17c, 1.17q). The incremental and inclination-based fold tests yield an improved clustering of directional data upon untilting (i. e. a significant increase in k from 0% to 100% unfolding) for both basins. The incremental fold test for JEB also yields a formally positive result (Fig. 1.17c), whereas the incremental fold test for TID renders barely inconclusive with 95% confidence intervals at 55% and 99% unfolding (Fig. 1.17q). The inclination-only fold test for JEB is marked by large confidence intervals including both the 0% and 100% threshold value potentially due to the low number of samples for this basin, while the BRF fold test for JEB as well as both inclination-based fold tests for TID are positive (Figs. 1.17d and 1.17r).

The third category comprises all basins of the Rehamna massif (MTA, NL and MEC) and the southern basins of the central massif (CHO, BOUH and KHE). All bulk fold tests turned out to be inconclusive with syn-folding maximal clustering at intermediate percentages of unfolding (Figs. 1.17e, 1.17g, 1.17i, 1.17k, 1.17m, 1.17o) probably caused by minor differences in bedding attitudes within respective basins (Tables 1.3 - 1.8) and in accordance with the inconclusive regional fold test of Domeier et al. (2021). As pointed out by Domeier et al. (2021), since the folding within the basins should be related to the final phase of the Variscan orogeny, a syn-folding maximal clustering would imply a paleomagnetic signal not much younger than the primary ages (~ 285 Ma). However, in contrast to their also inconclusive regional inclination-only fold test, the inclination-based fold tests of MTA (Fig. 1.17f), NL (Fig. 1.17h), MEC (Fig. 1.17j) and KHE (Fig. 1.17p) of this study are positive with varying widths of their respective confidence intervals implying a primary character of the magnetization and post-depositional variations of the declinations. For BOUH and CHO, at least their BRF fold tests were also positive, while their inclination-only fold tests were either inconclusive or accompanied by huge uncertainty intervals albeit clearly showing an increase in k upon unfolding (Figs 1.17l, 1.17n).

Ultimately, the northernmost sampled basin BOUA exhibits negative bulk fold tests, but a distinct increase of directional grouping for both inclination-based fold tests when reaching 100% unfolding, thereby providing a positive BRF fold test and a formally inconclusive inclination-only fold test due to its huge 95% confidence interval most likely related to the comparatively low number of available samples from BOUA (Figs. 1.17s-t).

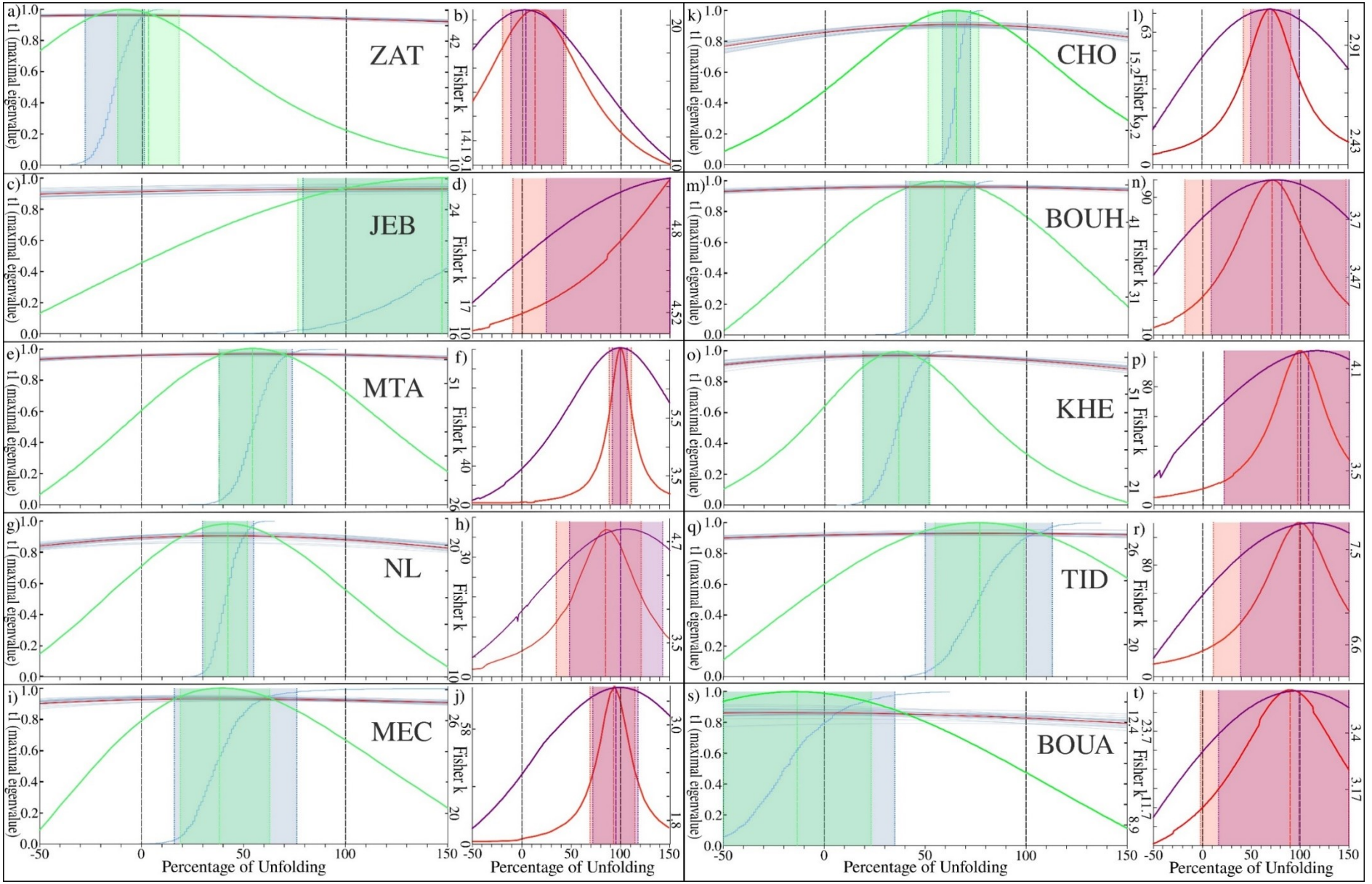
a)
b)
k)
l)
ZAT
CHO
c)
d)
m)
n)
JEB
BOUH
e)
f)
o)
p)
MTA
KHE
g)
h)
q)
r)
NL
TID
i)
j)
s)
t)
MEC
BOUA
t1 (maximal eigenvalue)
Fisher k
Percentage of Unfolding

Figure 1.17: Fold tests applied on component B data from this study arranged according to sampled basins from south to north. Threshold values of geographic coordinates/no folding (0%) and tectonic coordinates/complete folding (100%) are given by black vertical dashed lines. Left panels (a, c, e, g, i, k, m, o, q, s): Application of the parametric bootstrap fold test (blue) after Tauxe and Watson (1994) with N=1000 iterations and corresponding τ_1 eigenvalues (left ordinate) plotted against percentage of gradual unfolding. Red curves mark τ_1 values of the non-bootstrapped data and respective light blue curves represent the first 25 bootstrapped curves. 95% confidence intervals are highlighted by blue shaded intervals delimited by stippled vertical lines and cumulative density functions (CDFs) are represented by the blue curves. Fisher precision parameter k (right ordinate) is plotted against percentage of unfolding according to the incremental fold test procedure (green curve) as suggested by Watson and Enkin (1993) using 1% of incremental change in dip per iteration step. Best groupings of k are represented by dashed green vertical lines, with 95% confidence intervals shown as green shaded interval confined by green dotted vertical lines. Right panels (b, d, f, h, j, l, n, p, r, t): Results of inclination-based fold tests following Enkin and Watson (1996) where k is plotted against the percentage of unfolding. In the case of the inclination-only approach (red curve), maximal clustering of k (left ordinate) is characterized by the red dashed vertical lines, respectively, whereas corresponding 95% confidence intervals (determined by parametric simulation) are depicted by reddish areas delimited by red dotted vertical lines. For fold tests based on block-rotation fisher (BRF) analysis (purple curve), maximal values for k (right ordinate) are visualized by purple dashed vertical lines, respectively. Associated 95% confidence intervals (also based on parametric simulation) are indicated by purple areas confined by purple dotted vertical lines.

1.4.3 Discussion of New Paleomagnetic Data

For the southernmost basin ZAT all fold tests are negative (Figs. 1.17a and 1.17b), Fisher parameters deteriorate after applying tectonic correction (Table 1.11) and resulting paleolatitudes rather fit the ~ 260 Ma segment of the APWP of Gondwana instead of its assigned late Carboniferous age (Fig. 1.20), suggesting that ZAT represents a late Permian remagnetization and is therefore no longer considered in this work.

For each of the remaining nine basins, at least one of the bulk or inclination-based fold tests yields positive results (Fig. 1.17), indicating their high-stability components to be primary. Further support for this interpretation comes from the identification of normally magnetized samples/sites at three different sites/basins (i.e., MTA1, CHO1 and BOUH2). While MTA1 (N=1) and CHO1 (α_{95} = 20.3°) are admittedly associated with some uncertainty (Figs. 1.16c and 1.16f; Tables 1.3 and 1.6), BOUH2 is well-defined and unequivocally represents a reversal (Fig. 1.16g, Table 1.7). Since it is expected that the volcanics of BOUH were emplaced between 298.5 Ma and 264 Ma (Table 1.7), we ascribe the reversal to one of the two well-documented short normal magnetochrones CI2n (281.24 ± 2.3 Ma) and CI3n (275.86 ± 2.0 Ma) within the Kiaman reversed superchron (Hounslow and Balabanov, 2018). Domeier et al. (2021) also describe data (LTC of their site TZ1) hinting towards the possibility of a reversal within BOUH. If the reversal character of MTA1 and CHO1 is presumed and their estimated age range is considered (Tables 1.3 and 1.6), both sites can be ascribed to CI2n and CI3n as well. Relative and absolute age constraints favor CI2n (281.24 ± 2.3 Ma) as temporally closest (late-Artinskian) and therefore representative magnetochron for all three sites (chapter 1.3), but we emphasize the preliminary character of this interpretation.

1.5 Summary of Paleomagnetic Data from Morocco

1.5.1 Virtual Paleomagnetic Poles

To properly investigate the large amount of paleomagnetic data and its impact on paleogeographic reconstructions, all primary site/basin mean directions from this study (red/black circles for red beds/volcanics) and from available literature (blue squares) were transformed into virtual geomagnetic poles (VGPs; Fig. 1.18). Therefrom, paleopoles were calculated for each basin (yellow stars) which are also listed in Table 1.11. In accordance with the findings of section 1.4.2.2, no striking difference between samples of sedimentary and

volcanic origin can be found thus further corroborating the hypothesis that inclination shallowing is widely absent in our data set.

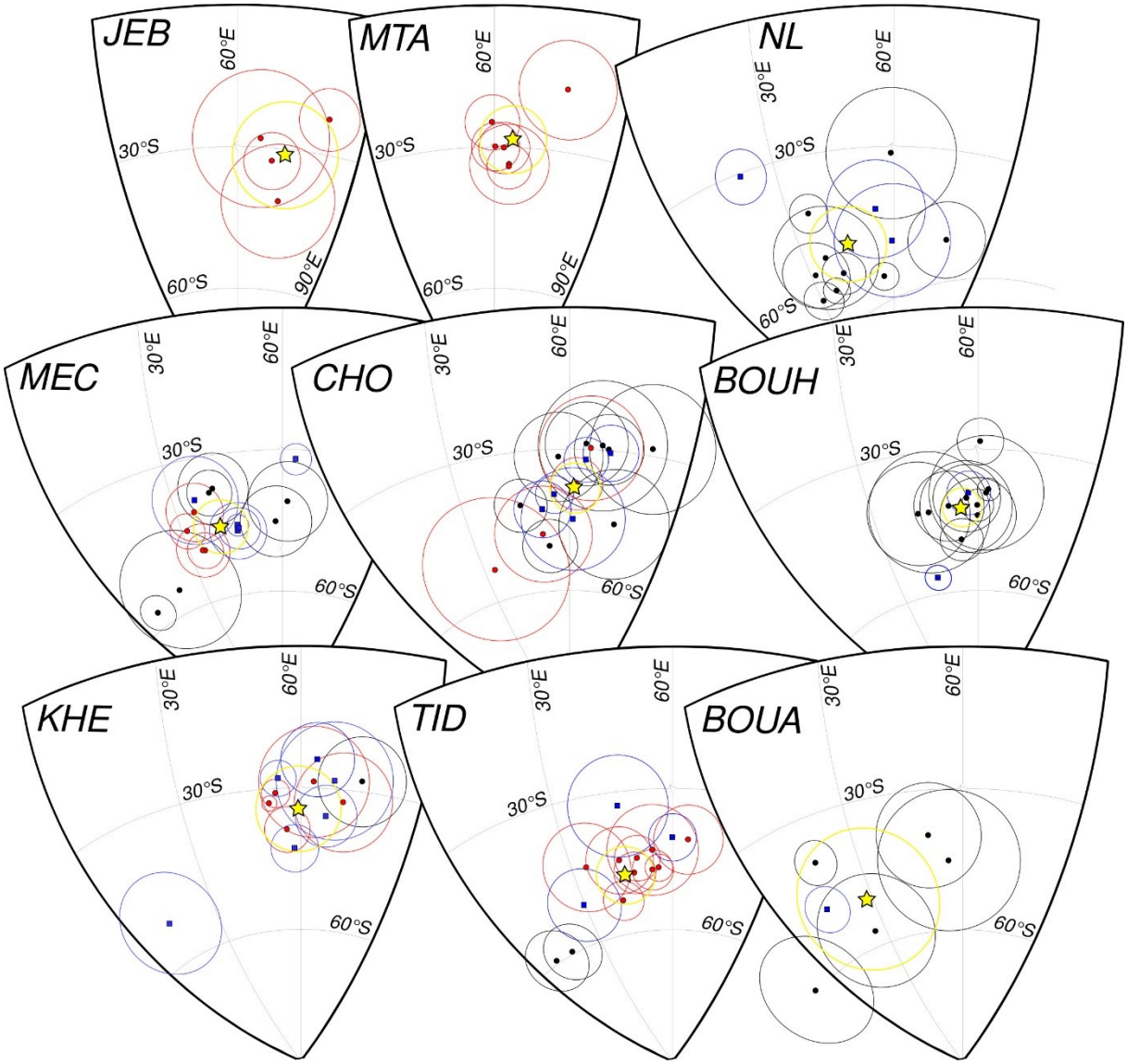

Figure 1.18: Virtual geomagnetic poles from the primary high-stability components of this study (red dots – red beds, black dots – volcanics) and of comparable literature (blue squares) with constituent uncertainties in tectonic coordinates in a Mesetian reference frame. For each basin, a paleopole and corresponding A95 (yellow star and contour) was calculated. Numerical values can be found in Table 1.11.

A majority of the inspected basins show an elongation of their bedding corrected VGPs in the NE-SW direction, an observation also reported by Domeier et al. (2021) for their significantly smaller Moroccan data set, who also suggest relative vertical axis rotations between or within constituent basins as a potential cause. Hence, in order to reliably assess and identify systematic rotational displacements, the data set needs to be discussed on a site-specific and basin-specific level. Therefore, we plotted all available primary Late Paleozoic Moroccan VGPs from the present study and from the literature on site-level with their respective mean

ages against the 310 Ma – 210 Ma APWP of Gondwana after (Torsvik et al., 2012) to obtain a more comprehensive picture (Fig. 1.19).

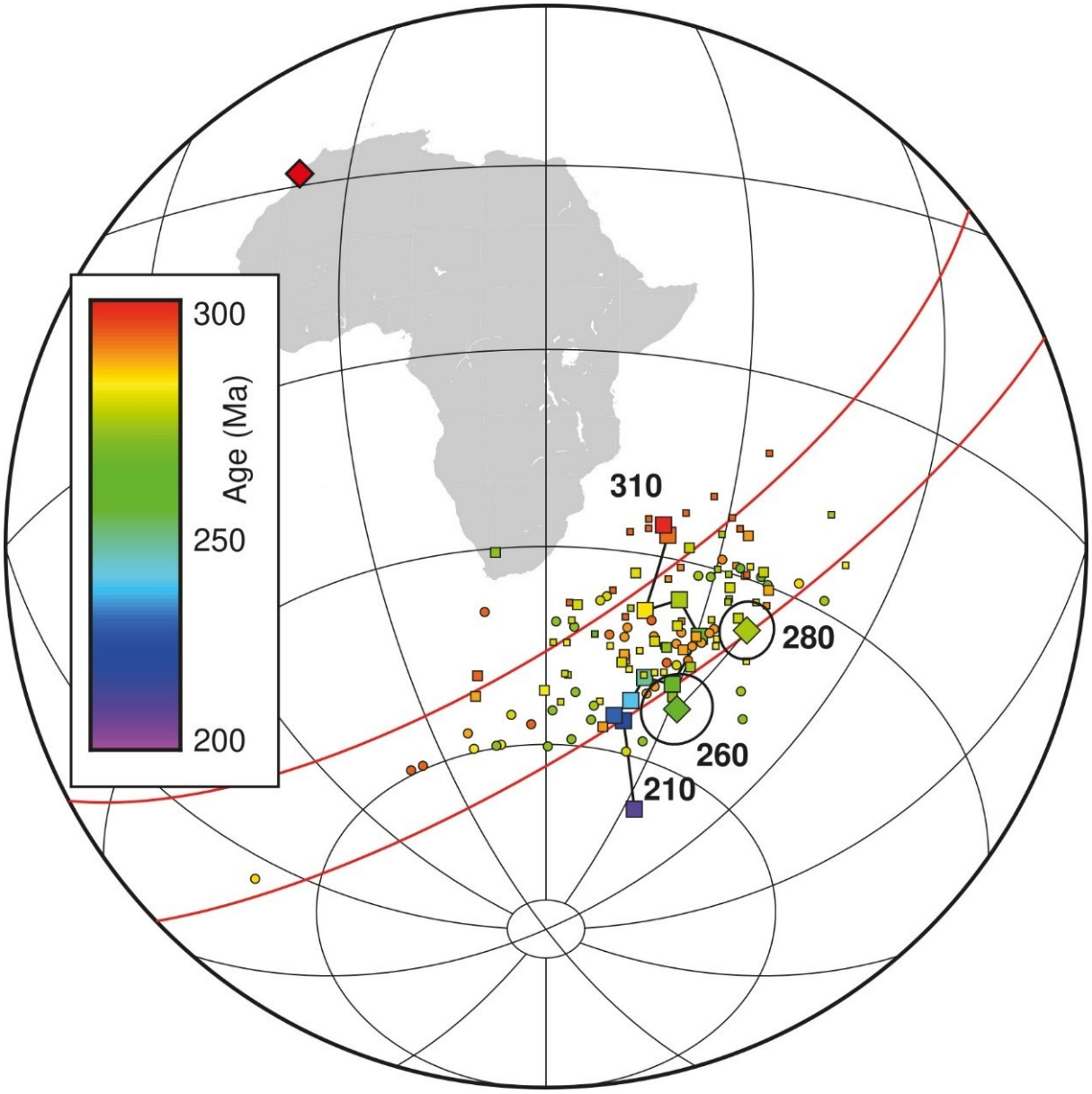

Figure 1.19: Virtual geomagnetic poles from this study (small circles) and VGPs from current literature (small squares) plotted in combination with 260 Ma and 280 Ma mean paleopoles (diamonds with black A95 confidence ellipses) from Channell et al. (2022) and the 310 Ma to 210 Ma APWP of Gondwana (big squares) by Torsvik et al. (2012). 95% confidence ellipses for this study's VGPs and for the APWP of Gondwana not shown for clarity. All poles are color-scaled according to their estimated mean ages (time bar from 300 Ma to 200 Ma shown in inset for comparison). Most poles fall within a small circle swath confined by red lines intersecting the Gondwana APWP at a time window of 300 Ma to 260 Ma. The pole of rotation to the small circle band lies within the sampling area (big red diamond) within the northwest of Africa (grey contour).

The VGPs from this study and published poles of comparable age for Morocco are broadly spread along a small circle band about a rotation point in Morocco in the middle of the study area and intersect the early Permian segment of the APWP. Moreover, the VGPs are plotting on both sites of the APWP, with an emphasis rather to the SW. These observations are in agreement with various amounts of vertical axis rotations affecting the Moroccan paleomagnetic data set. Apparently, counter-clockwise (CCW) and – to a higher percentage – clockwise (CW) vertical axis rotations are recorded in the studied samples, at least on site-level, with respect to Gondwana.

In order to further investigate the potential influence of rotational movements also on basin-level and its dependence on lithology, Fig. 1.20 shows all declinations and calculated paleolatitudes of site-mean VGPs and basin-mean paleopoles from this study as well as from published data sets drawn against their corresponding mean ages with uncertainties and color-coded according to their lithology (see legend). The expected declinations and paleolatitudes for a nominal reference point (Glat = 32°N, GLon= -8°E) were calculated based on the paleomagnetic compilations of Torsvik et al. (2012) and Channell et al. (2022). While a striking separate behavior is not detectable for volcanic and sedimentary results in Fig. 1.20, prominent features become obvious for both declination and paleolatitude subplots entailing further implications on the rotational mechanism and the paleogeographic reconstruction of the Moroccan Meseta.

1.5.2 Declination Variations and Rotational Mechanism

Whereas the expected declination from the APWP of Gondwana would suggest values between -40° and -60°, the Moroccan data reveal a large spread of declination between 0° and -60° with deviations up to 40°- 50° (Fig. 1.20). Upon calculation of basin-mean values, the spread decreases but is still statistically significant compared to predicted declinations. A clear trend of declination versus age, i.e., a proportionality of increasing age and declination deviation, is absent with only the northernmost and oldest basin BOUA showing the highest ΔD. In sum, the predominance of CW rotations with respect to the referential APWP is observed both on site-level and basin-level.

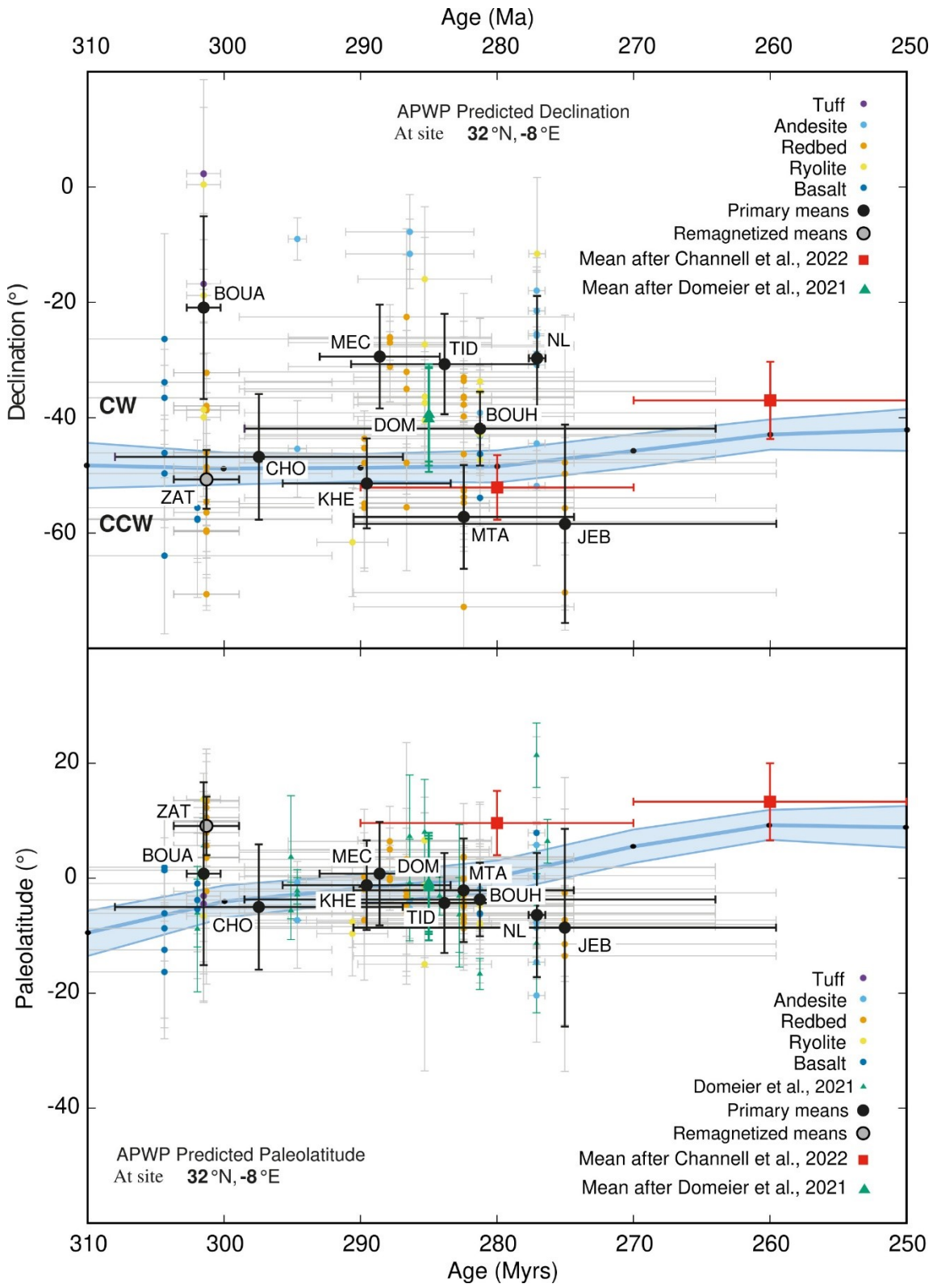

Figure 1.20: Declination and paleolatitude drawn against assigned age ranges (all with error bars) for the Moroccan results of this study on site-level (small circles color-coded according to underlying lithology) and basin-level (big black circles) as well as of Domeier et al. (2021) (triangles) and of Channell et al. (2022) (squares). The grey and black contoured circle shows the mean of the putatively remagnetized site ZAT. Predicted declination and paleolatitude based on the Gondwana APWP of Torsvik et al. (2012) and Channell et al. (2022) calculated for a nominal reference point amidst the sampled area in Morocco at 32°N and -8°E (blue polygon with associated error band).

The calculated declination based on the Meseta paleopole of Domeier et al. (2021) is located in the middle of this study's declinations based on our basin-mean paleopoles. The results of Domeier et al. (2021) only exhibit a slight amount of rotation within error relative to the Gondwanan reference site (Fig. 1.20). Our data set significantly improves the information on potential CCW and CW rotations in the Moroccan Meseta showing distinct CW rotations of NL, MEC and the northernmost basins of TID and BOUA, tendencies of CCW rotation of JEB and MTA (although not well resolved due to overlapping uncertainty intervals) and no clear basin-range rotation for CHO, BOUH and KHE in broad agreement with the fold tests results shown in Figure 1.17. Additionally, relative rotations within basins are also observed (Figs. 1.20 and 1.21). Since the stratigraphic position of sampled sites is not well constrained, we cannot define the timing of rotation of the pull apart basins for sure. However, the observed paleomagnetic rotation pattern suggests a syn-sedimentary rotation of the basins and therefore a syn-depositional magnetization acquisition. Declination values mainly based on Adria data of Channell et al. (2022) are well within rotational uncertainties of the APWP of Africa for using only averaged poles for 260 Ma and 280 Ma derived from a compilation of several separate areas. A recent study based on late Permian rocks from the Argana basin did not reveal any large scale declination variations (Kent et al., 2021), which are a further argument for an age of rotation close to the deposition/emplacement of the sediments/volcanics of the Meseta block. It has to be noted, however, that our conclusion is not with finality and more data is needed to ultimately constrain the age of rotational variation within the Meseta block.

Vertical axis rotations are present within and between the pull-apart basins. However, extent and rotational sense is not consistent. For the southern basins of the Jebilet and Rehamna massifs declination deviation seems to increase when going from NE to SW (Fig. 1.21), which would suggest a continuous rotation of a larger block. In contrast, observed vertical axis rotations of the northern basins of the Central massif follow no greater structural trend, but rather resemble brittle, fragmented rotations of multiple small blocks (Fig. 1.21; e.g. Todrani et al., 2020). Following Elter et al. (2020), dextral shearing of Laurasia with respect to Gondwana in the Late Paleozoic might have dismembered the northern margin of Gondwana into many "Gondwana derived continental (GDC)" crustal blocks that subsequently suffered differential rotations. Rotational movements between the basins can best be explained by the ball-bearing model as proposed by Aubele et al. (2012) consistent with a large shear system between the south and north of Pangea. By sampling the Moroccan Meseta we approached the presumed location of the Pangean mega-shear zone in the Mediterranean from the south and thus may have documented its distal effect on (northern) Moroccan basins.

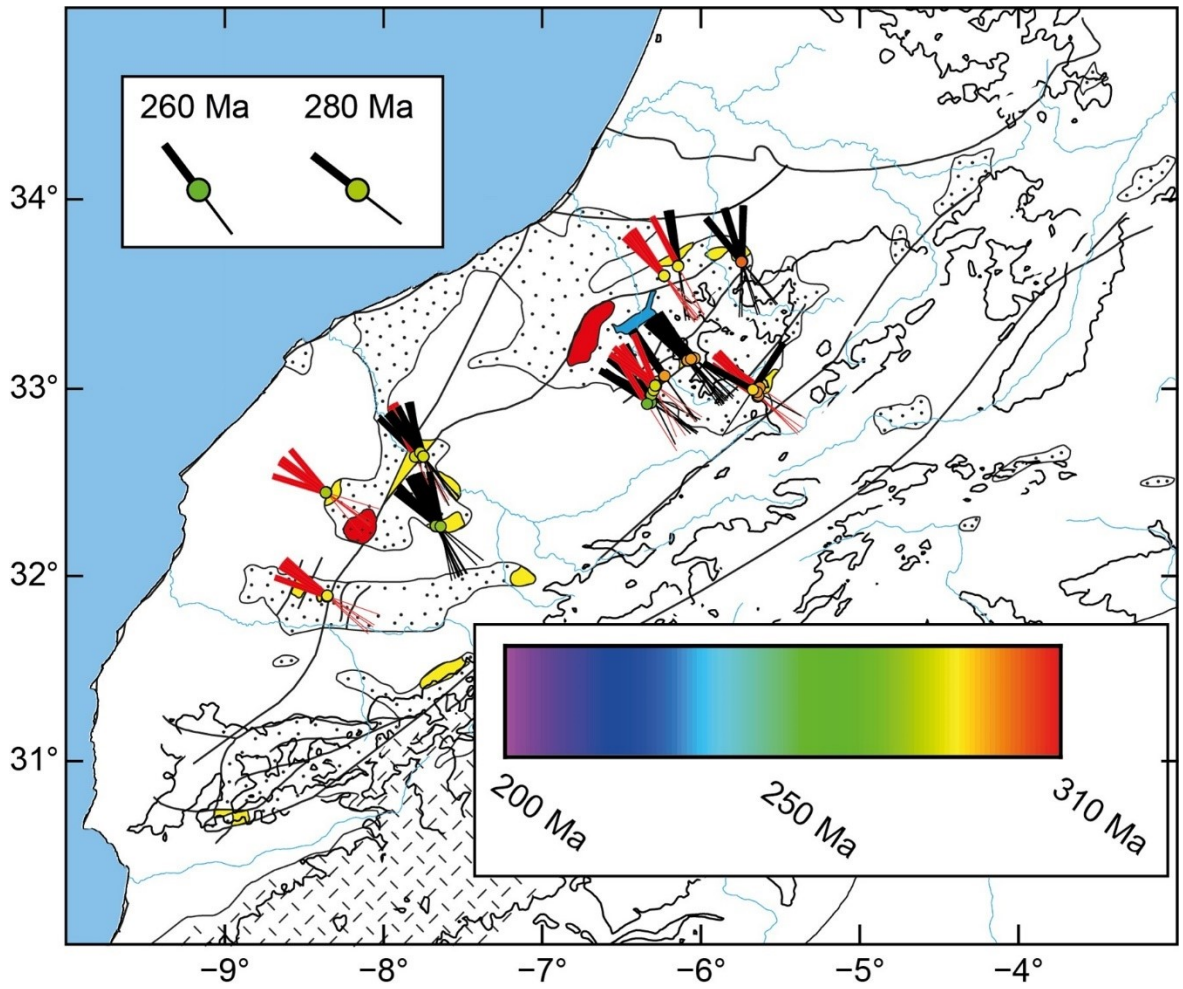

Figure 1.21: Declination values at the respective sites and basins shown with underlying main geologic units of Fig. 1.1. Reference declination at 260 Ma and 280 Ma are given in the top left of the figure for comparison. Fat black (red) lines display orientation of the volcanic (red bed) site mean declinations while color of the corresponding circle indicates the basin-mean age.

1.6 Implications of the Morocco Data for Pangea

1.6.1 Paleolatitudes and Plate Tectonic Reconstructions

Generally, the paleolatitude of the VGPs (site-level) and paleopoles (basin-level) are much more confined spreading only about 20° (Figure 1.20 is shown with the same y-axis length). The predicted basin-mean paleolatitudes of this work agree well within uncertainty bonds with previous results of Domeier et al. (2021) for the stable latitudinal position of the Moroccan Meseta (and Northern Africa) in the early Permian and also with referential values based on the APWP of Torsvik et al. (2012). It has to be noted that our data seem to imply a southward motion of the Meseta block between ca. 300 and 275 Ma, which would mean that the Meseta block underwent a disconnected motion compared to Gondwana, which moved

rather northward (Fig. 1.20). However, all our data matched the expected paleolatitude curve of Gondwana within error limits, making any robust statements about potential separate movements of Gondwana and Meseta not statistical viable at this stage.

While the 260 Ma mean paleopole of Channell et al. (2022) coincides well with the reference paleolatitudes, the 280 Ma averaged paleopole is shifted ~10° towards more positive values being just significantly distinct from the 280 Ma predicted paleolatitude from the Gondwana APWP and also deviating from this study's primary results (Fig. 1.20). For the calculation of the Cisuralian overall mean paleopole, Channell et al. (2022) mainly adopted the paleomagnetic compilation of Kent and Muttoni (2020) by including seven paleopoles from Adria as a proxy for Gondwana (from a total of 13 paleopoles used, see their Table 2). Pastor-Galán (2022) averaged all Adria poles documented in Kent and Muttoni (2020) into one pole and observed a similar paleolatitude deviation from the global apparent polar wander path rotated into Gondwana coordinates (their Figure 5). Therefore, it seems that paleomagnetic data from Adria cannot be simply assumed representative of Africa or Gondwana and thus the coherence of Adria and Africa becomes questionable. Hence, in contrast to our results on declinational variations, the paleolatitudinal results do not reinforce the validity of Pangea B. It should be pointed out that a late Carboniferous to earliest Permian Pangea B configuration as proposed by Klootwijk (2023) cannot be addressed using our dataset because the earlier data is not as numerous and robust (Fig. 1.20). Another problem regarding this time interval is related to a general spread of paleomagnetic data during the early Permian (Wu et al., 2015). Accordingly, more studies with a high site number like ours should be carried out for more places in Gondwana and Laurussia to complete our paleogeographic understanding of the assembly of Pangea.

To assess the implications of our data from the Meseta block for global reconstructions during the Permian we followed the approach of Domeier et al. (2021). Accordingly, we plot the paleopoles for Laurussia without inclination shallowing correction at 280 Ma of Torsvik et al. (2012) and the modified paleopoles for Gondwana for the same age (GP2 of Domeier et al., 2021). Our coloring of Gondwana (blue) and Laurussia (orange) follows Figure 16 of Domeier et al. (2021). Additionally, we plot a great circle (GC) fit to our data of ca. 280 Ma with and without the slightly younger area JEB. The centers of the great circle fits are very close to the actual sampling locality. It is interesting to note that a great circle around the proposed minimum-inertial axis (I_{MIN}) also seem to fit our paleopole data (Fig. 1.23). As expected from Figure 1.20, in terms of paleolatitudes our new extensive Gondwana-related data set is in agreement with all three major continental reconstructions of Gondwana and Laurussia without

a significant overlap at ca. 280 Ma (Fig. 1.22). There is a spread of our paleopoles visible, which does not seem to be correlated to an age progression (Figs. 1.19, 1.20, 1.23). As discussed earlier, this spread can be explained by vertical axis rotations affecting the various basins with different amplitudes resembling comparable late Paleozoic rotation patterns in SE France (Aubele et al., 2012) and Sardinia (Aubele et al., 2014; Bachtadse et al., 2018; Siravo et al., 2023). A TPW related explanation appears possible based on the sense of spread, especially when taking into account that the sampling locality is located close to I_{MIN} (Fig. 1.22), which could lead to rapid declination variations. More data is needed to further address this possibility.

1.6.2 Moroccan Data in a Global Context

To put our paleomagnetic results in a global context, we focus on the implications for a 280 Ma time, which is the crucial age when a significant overlap between Gondwana and Laurussia was identified (Channell et al., 2022). We show three continental reconstructions (Fig. 1.22) from the major contributors of these types of models: Earth-Dynamics Research Group / EDRG (Wu et al., 2024), EarthByte (Merdith et al., 2021) and the Center for Earth Evolution and Dynamics / CEED (Torsvik et al., 2014). We additionally provide a model constructed using Gondwana and Laurussia poles based on Channell et al. (2022). Figure 1.23 shows the resulting paleopoles of each paleogeographic reconstruction associated with the plate IDs of Gondwana (based on Domeier et al. (2021) and Channell et al. (2022)), Laurussia (based on Torsvik et al. (2012) and Channell et al. (2022)) and from Morocco (this study). It has to be noted that Channell et al. (2022) did include Moroccan data from the Meseta block of Domeier et al. (2021) in their 280 Ma mean paleopole of Gondwana as well as data from Adria. Inspection of Figures 1.22 and 1.23 reveals that our Meseta data is in general agreement with all presented paleogeographic models, where our data seems to be better represented by the Gondwana mean pole of Domeier et al. (2021), rather than that by Channell et al. (2022). Ultimately, since our data are also compatible with the Channell et al. (2022) reconstruction, the presence or absence of the latitudinal overlap of Gondwana and Laurussia is related to the low confidence intervals of Channell et al. (2022)'s paleopoles and the inclusion of the Adria data, which slightly moves the Gondwana mean pole (Fig. 1.23). In summary, the Meseta paleomagnetic data do not support a large latitudinal overlap of Gondwana and Laurussia and does therefore not require a Pangea B configuration in the early Permian. Our results stress again the importance of the structural relationship between Adria and Gondwana as the key to resolve the Pangea controversy.

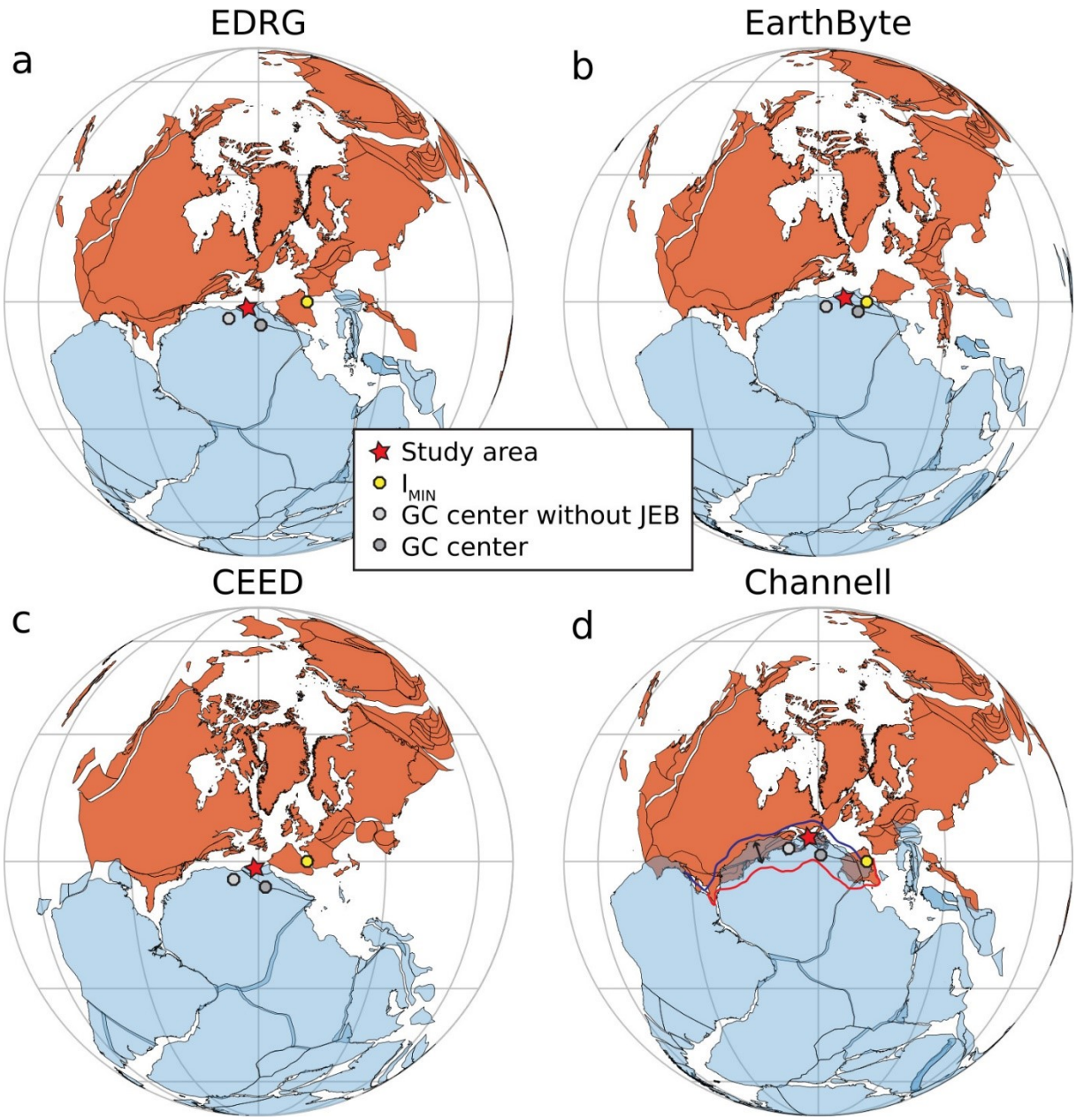

Figure 1.22: Paleogeographic reconstructions for 280 Ma, where blue continents correspond to Gondwana and orange ones to Laurussia. Red star indicates the study area in Morocco. (a-d) shows four different reconstructions based on paleogeographic models of: (a): The Earth-Dynamics Research Group (EDRG) after Wu et al. (2024), (b): EarthByte after Merdith et al. (2021), (c): The Center for Earth Evolution and Dynamics (CEED) after Torsvik et al. (2014), (d): Channell et al. (2022). Model (d) furthermore displays the reconstructed modern continent ocean boundaries visualizing the resulting continental overlap (Domeier et al., 2021). Also shown are the centers of great circle (GC) fits of our ca. 280 Ma data with (dark grey circle) and without (light grey circle) the paleopole of area JEB together with the proposed location of the minimum-inertial axis I_{MIN} (yellow circle), around which true polar wander (TPW) should take place (Torsvik et al., 2014).

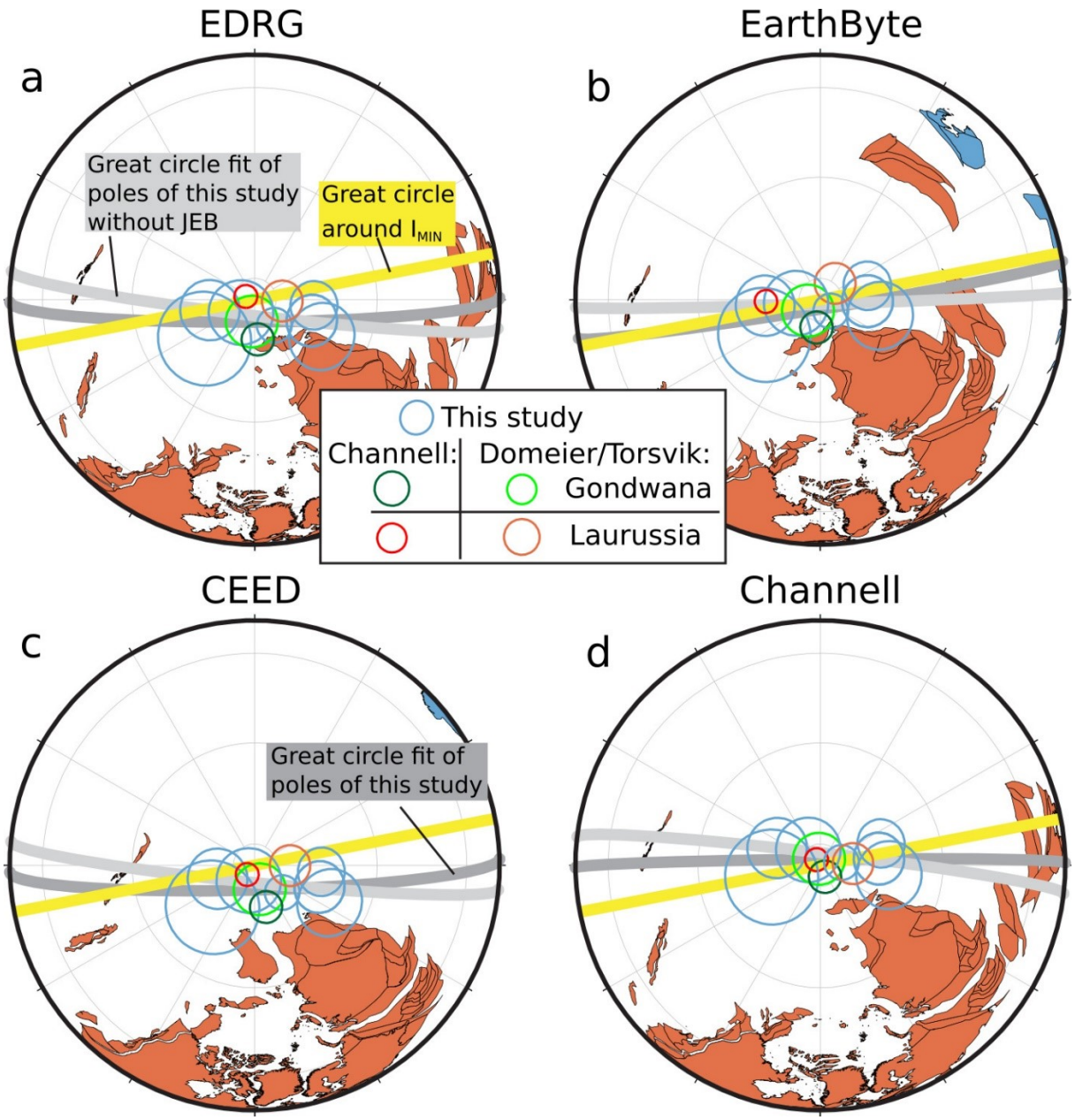

Figure 1.23: Reconstructed paleopoles according to reconstructions of Figure 1.22 from Gondwana: light green: Domeier et al. (2021), dark green: Channell et al. (2022) and Laurussia: orange: Torsvik et al. (2012), red: Channell et al. (2022) together with our coeval results (blue) of ca. 280 Ma from the Moroccan Meseta block (see Table 1.12 for details). Also shown are great circles around the proposed I_{MIN} of this time (Torsvik et al., 2014) in yellow and fits to our data in light grey (our data of ca. 280 Ma without paleopole of area JEB) and dark grey (all our data of ca. 280 Ma).

1.7 Conclusions

The presented paleomagnetic collection from Morocco represents one of the biggest entries in the paleomagnetic database for the late Paleozoic of the recent past. By integrating age constraints derived from recent radiometric dating, stratigraphy and paleontology we could further resolve and update the tectonic and paleogeographic setting for NW Africa (resp. Gondwana) provided by Domeier et al. (2021).

***Table 1.12**: Paleomagnetic poles used for reconstructions. Lat N, Lon E: paleopoles latitude and longitude in ° north and east. A_{95}: confidence interval*

Area	*Lat N*	*Lon E*	*A_{95}*	*Reference*
Gondwana (GP2)	*-37.7*	*59.3*	*6.1*	*(Domeier et al., 2021)*
Laurussia	*-45.0*	*340.9*	*2.6*	*(Torsvik et al., 2012)*
Gondwana	*-41.5*	*62.3*	*3.8*	*(Channell et al., 2022)*
Laurussia	*-46.0*	*345.1*	*2.7*	*(Channell et al., 2022)*
JEB	*-31.3*	*71.9*	*11.2*	*This study*
MTA	*-28.4*	*64.5*	*7.1*	*This study*
NL	*-49.8*	*45.3*	*8*	*This study*
MEC	*-45.1*	*41.5*	*5.7*	*This study*
TID	*-47.6*	*45.3*	*6.1*	*This study*
BOUH	*-42.2*	*55.5*	*4.1*	*This study*
KHE	*-34.4*	*59.4*	*7.6*	*This study*

Apart from a late Permian remagnetization of the southernmost basin ZAT revealed by negative fold tests, at least one type of fold test shows a positive outcome for all residual basins. Matching paleolatitudes for the respective age models and the presence of reversals at three basins (MTA, CHO and BOUH) that could be correlated to the late-Artinskian CI2n normal magnetochron (281.24 ± 2.3 Ma) within the Kiaman reversed superchron support a primary character of the latter.

The VGPs are elongated in a NE-SW sense and strung out along a small circle band intersecting the early Permian portion of the APWP of Gondwana with the Euler pole located within the study area thus showing CW and – to a minor extent – CCW vertical axis rotations on site and basin level. Since observed paleolatitudes are located close to the paleoequator and no striking difference between the volcanic and red bed samples was observed, inclination shallowing presumably has not altered the paleomagnetic signal.

Since paleomagnetic data from Adria has repeatedly been used to extend the sparse available data set for Gondwana and has been invoked as supportive evidence for the validity of Pangea B, we compared a 280 Ma mean paleopole that combined all available early Permian

information of Gondwana and Adria (Channell et al., 2022) with our results derived directly from Gondwana. The paleolatitude determined from the combined pole is within error of the newly obtained data, but slightly offset towards higher values. We used our paleopole data in the most up-to-date continental paleogeographic reconstructions to investigate the significance of the Moroccan data in the ongoing Pangea controversy. Interestingly, our data confirms previous data by Domeier et al. (2021) and overlaps with Gondwanan mean poles by Domeier et al. (2021) and by Channell et al. (2022). Accordingly, our data does not require a large continental overlap and therefore a Pangea B configuration, but it also stresses that ultimately only the inclusion/exclusion of paleomagnetic data from Adria can resolve the Pangea controversy. The potential vertical axis rotations within the Meseta block lend additional support to the existence of a major intra Pangea shear zone as proposed by Aubele et al. (2014).

1.8 Acknowledgements

VB was supported by the German Research Council (DFG) Grant BA1210/24-1. We are thankful to Giovanni Muttoni who triggered the project and who commented on earlier drafts of the manuscript. UK acknowledges funding from an Australian Research Council Discovery Project (DP210102495) awarded to Zheng-Xiang Li and Andy J Biggin. AR acknowledges also PRIN Project n.2022ZH5RWP DEtailing thE Palaeogeography of Southern PAlaeoeurope by meanS of biosTratigraphic correlation and basin development in the Palaeozoic to early Mesozoic time-frame: case histories from the Italian record (DEEP PAST).

2 Additional Sampling Areas in Morocco

In chapter 2, we describe the findings from those sampling areas in Morocco, which have not been discussed in chapter 1 due to their insufficient data reliability, namely the basins of Argana (ARG), Souss (i.e. the subbasins of Ida Ou Ziki – ZIKI – and Ida Ou Zal – ZAL), Ourika (OUR) from the Western High Atlas, the Sebt Brikiyne granite (BRI) from the Rehamna Massif and ultimately the Zaer granite (ZAE) as well as the basins of Sidi Kassem (KASS) and Bouterhella (BOUT) from the Central Massif where additional 329 samples from 55 sites were collected (Figs. 2.1, 2.2, Tables 2.1 – 2.8).

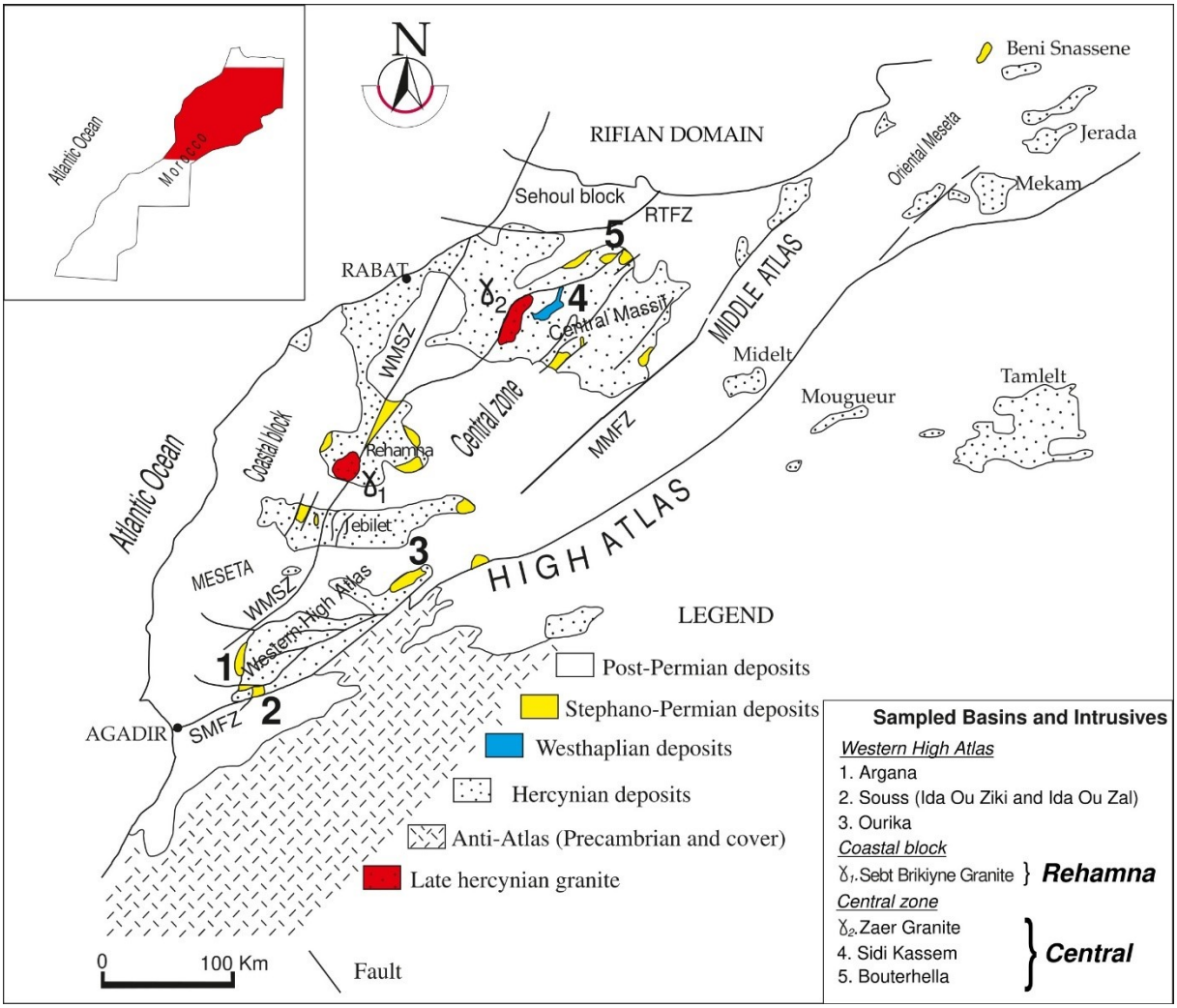

Figure 2.1: Schematic structural and geological map of the sampling area in the Moroccan Variscides with Late Paleozoic basins and late Hercynian plutonic massifs being highlighted whose paleomagnetic data sets have not been published (see text for explanations). Delimitation of main tectonomorphic domains after Chopin et al. (2014), Hoepffner et al. (2005), Hoepffner et al. (2006), Michard et al. (2008), Michard et al. (2010a) and Michard et al. (2010b). WMSZ: Western Meseta Shear Zone, RTFZ: Rabat-Tiflet Fault Zone, MMSZ: Middle Meseta Fault Zone, SMFZ: South Meseta Fault Zone.

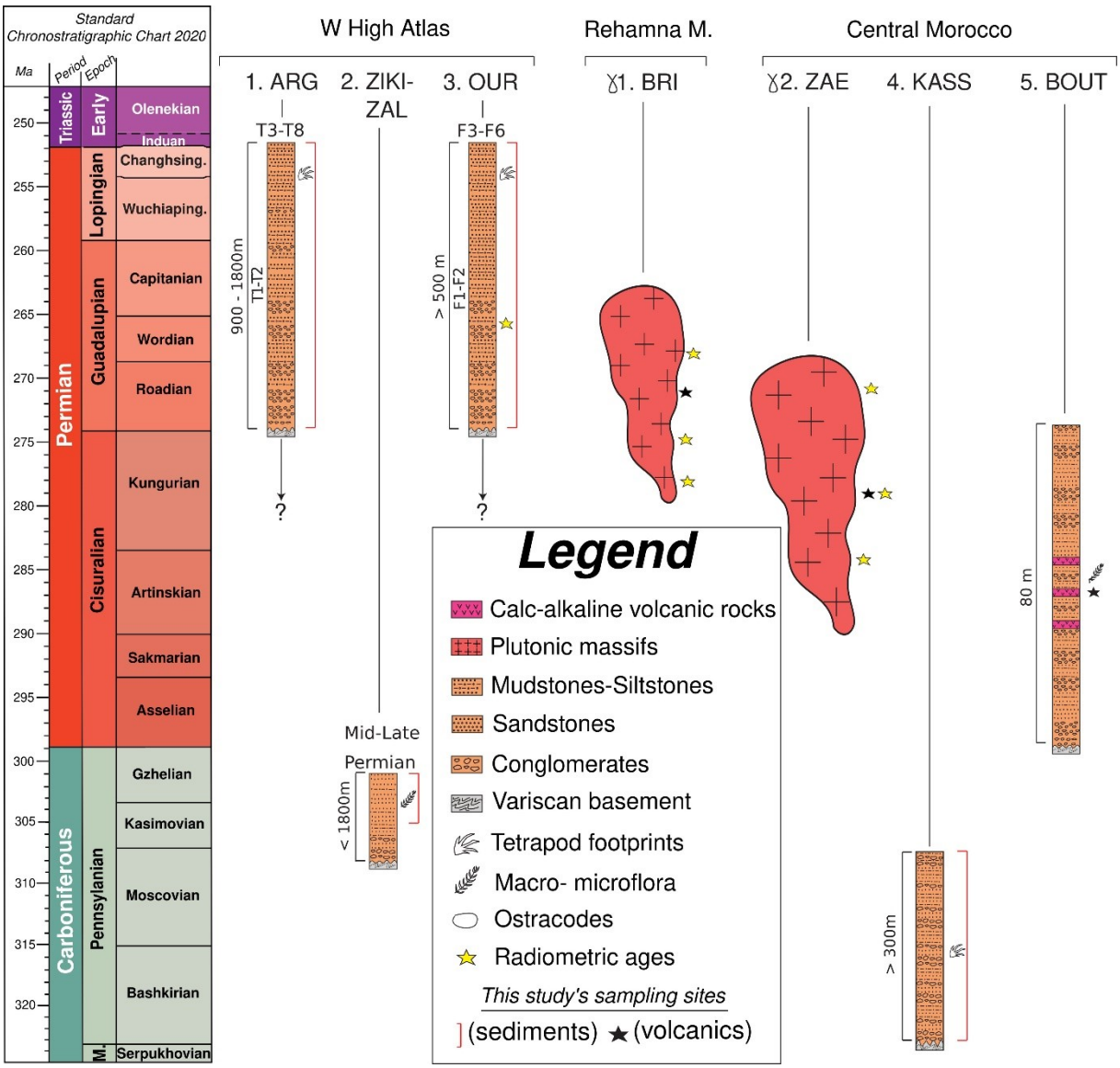

Figure 2.2: Lithostratigraphic correlation of sampled Westphalo-Permian basins in Morocco (yielding unpublished data sets) with sampling horizons together with paleontological and radiometric age constraints (see text for further information and references) ordered by corresponding late Paleozoic domains from south to north (numbering as in Fig. 2.1). Standard Chronostratigraphic chart after Gradstein et al. (2020). Symbols as in legend.

2.1 Argana (ARG)

The Argana basin is located between Marrakech and Agadir at the southwestern edge of the WHA and refers to an approximately 20 km wide and 70 km long, NNE–SSW trending area of well exposed Permian–Triassic red-beds (Fig. 2.1). The 2500–5000 m thick Permo-Triassic sedimentary succession consists of alluvial, fluvial, lacustrine, aeolian and playa deposits that accumulated in a continental rift basin. It unconformably caps the deformed, metamorphized Hercynian (Cambrian to Devonian) basement as well as, locally, late Carboniferous

(Stephanian A/B) clastics of the Souss basin and is followed by up to 150 m thick Rhaetian-Hettangian tholeiitic basalts (Belahmira et al., 2019; Hmich et al., 2005; Hmich et al., 2006; Jones, 1975; Kent et al., 2021).

Tixeront (1973) proposed a subdivision of the succession in eight lithostratigraphical units (T1–T8), which Brown (1980) formally assigned to three formations, each of them separated by either an angular or erosional unconformity. These are from base to top (Fig. 2.2): 1) The Ikakern formation (900–1800 m thickness) consisting of alluvial fan conglomerates (T1, Aït Driss member) grading vertically and laterally into red and purple alluvial plain conglomerates, sandstones, and mudstones (T2, Tourbihine member); 2) The Timezgadiouine formation (1000–2000 m), represented by braided river deposits (T3, Tanamert member), playa mudstones with intercalations of sheetflood and ephemeral stream sandstones (T4, Aglegal member) and alluvial plain sandstones and mudstones (T5, Irohalen member); 3) The Bigoudine formation (300–1500 m) starting with braided river conglomerates and aeolian sandstones (T6, Tadrat Ouadou member) that grade into increasingly fine-grained partially evaporitic playa red-beds (T7–T8, Sidi Mansour and Hasseine members) (e.g. Kent et al., 2021 and references therein).

Lithostratigraphic constraints as outlined by Kent et al. (2021) show that the Ikakern formation must be (middle – late) Permian in age. Furthermore, vertebrate remains from the uppermost level of T2 suggest at least a late Permian age for the T2 member (Dutuit, 1988; Jalil and Dutuit, 1996; Jalil and Janvier, 2005). Additionally, a moderately diverse assemblage of invertebrate and vertebrate traces from red beds of the Tourbihine Member (T2) confirmed the late Permian age of T2 (Hminna et al., 2012; Voigt et al., 2010).

The Timezgadiouine and Bigoudine formations are dated as Late Triassic (middle Carnian to earliest Norian) based on vertebrate remains and palynomorphs (Jalil, 1999; Tourani et al., 2000). Recently recovered tetrapod footprints from the T3 member and from the middle part of T4 suggest, however, that deposition of the Mesozoic part of the Argana red beds can be ascribed respectively to the Early and to the Middle Triassic (Klein et al., 2010; Klein et al., 2011; Lagnaoui et al., 2012; Lagnaoui et al., 2016).

We collected 61 paleomagnetic drill cores at 10 sites (close to the village of Si Mbark ou Mbarek and near the Assif n' Ait Moussa) from the Ikakern formation in the Argana basin (Fig. 2.3, Table 2.1). Since reliable absolute dating information is lacking, we apply all available stratigraphic and paleontological age constraints and assume a Guadalupian-Lopingian age for all our samples, i.e. 274.37 – 251.9 Ma as suggested by Henderson et al. (2020). Additionally,

Kent et al. (2021) report a characteristic remanent magnetization (ChRM) from the Ikakern formation displaying a mixed polarity pattern in contrast to our results' predominant reversed polarity (see chapter 1.4.2). Hence, the age of the samples can be bracketed by the onset of the Illawara mixed polarity interval (~ 267 Ma according to Hounslow and Balabanov (2018)) and the end of the Permian (= 251.9 Ma following Henderson et al. (2020)).

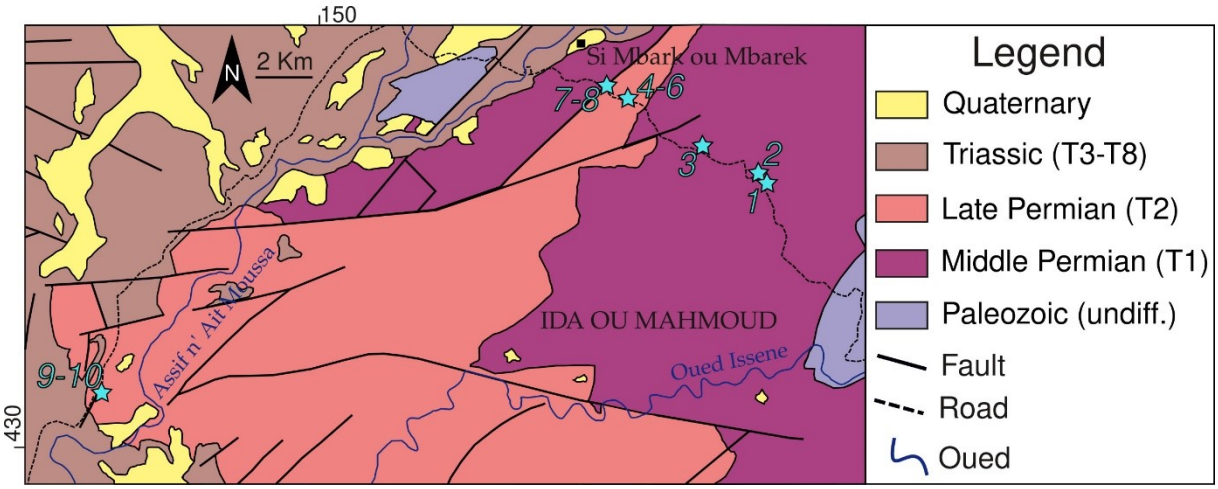

Figure 2.3: Simplified geological map of the Argana basin (ARG), based on the geological map of Morocco – sheet Argana / Western High Atlas (1/100000), model completed in 1971 and published in 1974 after Abdelkader Benslimane (1974). Light blue stars specify this work's paleomagnetic site positions. Numbering of samples correlate with Table 2.1. For further explanations see legend and text.

The paleomagnetic directions of the site-mean high-stability components of ARG exhibit SE declinations with inclinations pointing moderately upwards in geographic coordinates (Fig. 2.4a) which are shifted towards the sub-horizontal upon untilting (Fig. 2.4b). In contrast to the uniform reversed polarization of this study's data, the paleomagnetic collection of Kent et al. (2021) displays antipodal directions passing a local fold test (blue circles in Figure 2.4a-b). Note, that the reversely magnetized part of their data stems from the same sampling area as our data (near Si Mbark ou Mbarek) whereas the residual samples are collected at different localities (Sanaga and Ida Ou Kess Issar) within the Argana basin (Table 2.1). When the normally magnetized site-mean data of Kent et al. (2021) is mirrored and averaged with the reversed part of the data set, the resulting basin-mean directions from this study and of Kent et al. (2021) are statistically indistinct from each other (blue and red stars in Figure 2.4a-b). Since the Fisher parameters slightly deteriorate after tectonic correction (Table 2.1) and a Fisher distribution is not visually evident due to elongated streaking of declinations (Fig. 2.4a-b), this integral requirement for further analysis is confirmed by applying the quantile-quantile method described by Fisher et al. (1993) on the bedding-corrected data set of this work (Fig. 2.4c-d).

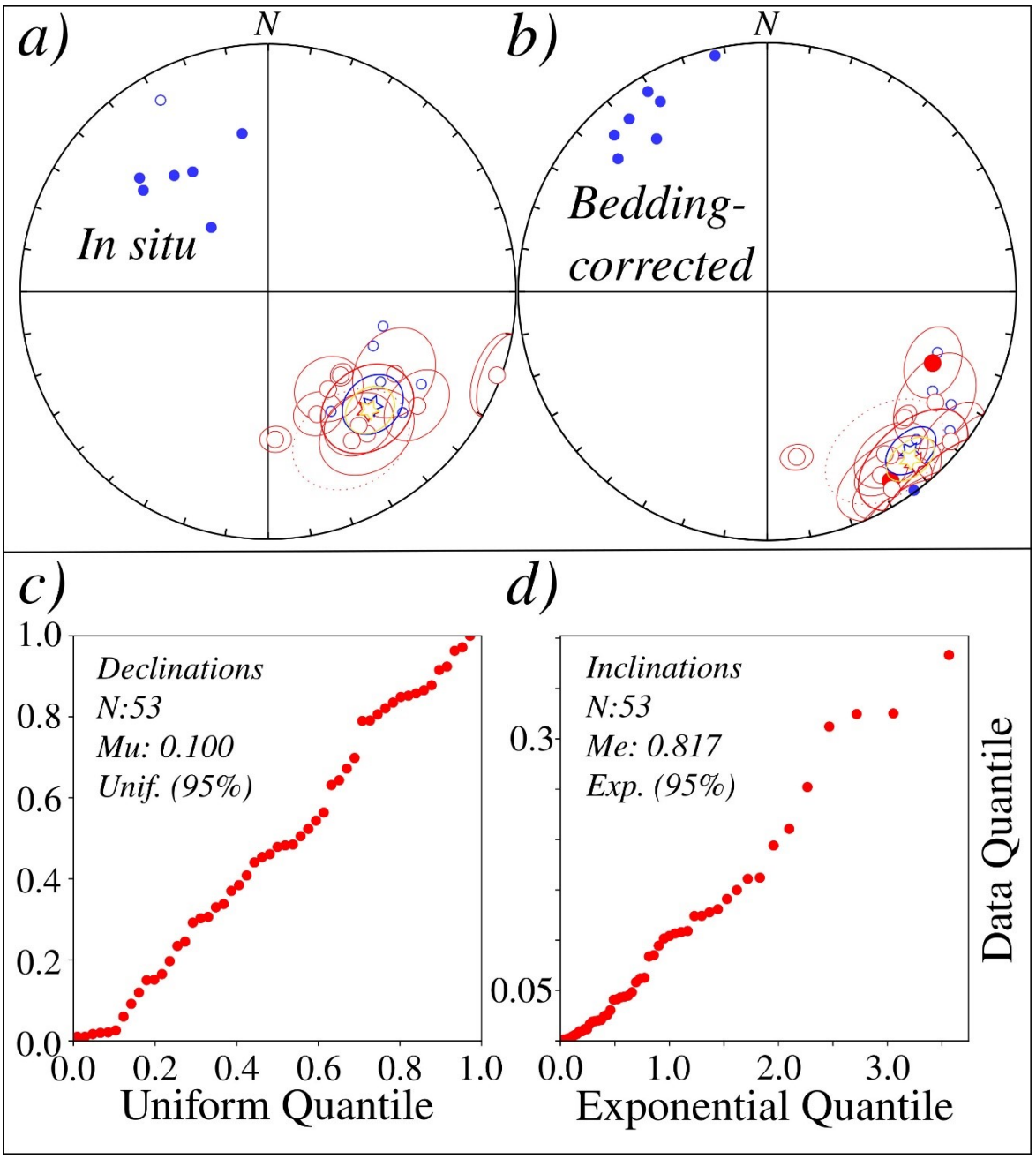

Figure 2.4: (a)-(b): Stereographic equal-area projection of site-mean (circles) and basin-mean (stars) directions from Argana (ARG) in geographic (in situ) and tectonic (bedding-corrected) coordinates. Red circles and 95% confidence ellipses show site-mean stereographic projections of paleomagnetic data derived from red beds in the course of this study whereas the blue circles reflect the available data set from Kent et al. (2021) for Argana (no α_{95} available). Blue stars specify the ARG-mean direction when converting all data of Kent et al. (2021) in reversed (south) coordinates (D_{geo} = 137.2°, I_{geo} = -37.7°, $\alpha_{95,\,geo}$ = 9.8°, k_{geo} = 16.3 / D_{tect} = 138.0°, I_{tect} = -14.7°, $\alpha_{95,\,tect}$ = 7.6°, k_{tect} = 26.4). Yellow stars represent the ARG-mean direction combining the data of this study and of Kent et al. (2021). Numerical values for the shown data can be found in Table 2.1. Conventions as in Fig. 1.16. (c)-(d): Quantile-quantile diagram of declinations plotted against a reference uniform distribution (left) and inclinations drawn against an expected exponential distribution (right) taken from bedding-corrected paleomagnetic directions of this study's ARG site-data after Fisher et al. (1993). If both test statistics M_u and M_e do not exceed the critical values of M_u = 1.207 and M_e = 1.094, the data is Fisher distributed at a 95% level of confidence. Conventions as in Fig. 1.16.

Because the data set is Fisher distributed at a 95% significance level, we can apply the McElhinny (1964) fold test by comparing the precision parameters before (k_1= 13.1) and after (k_2= 11.1) applying tectonic correction yielding a ratio k_2/k_1 = 0.85 < 2.12 for N = 9 hence statistically not passing the fold test on a 95% significance level. A negative outcome is also observed when applying the parametric incremental fold test (Watson and Enkin, 1993) as well as the bootstrap fold test (Tauxe and Watson, 1994) on the high-stability paleomagnetic data from ARG, with both confidence bounds clearly missing the 100% threshold (Fig. 2.5a). In contrast, both the parametric inclination-only and the BRF fold tests (Enkin and Watson, 1996) render positive, with both confidence bounds encompassing the 100% threshold and maximal clustering at 91% (BRF) and 96% unfolding (inclination-only), respectively (Fig. 2.5b).

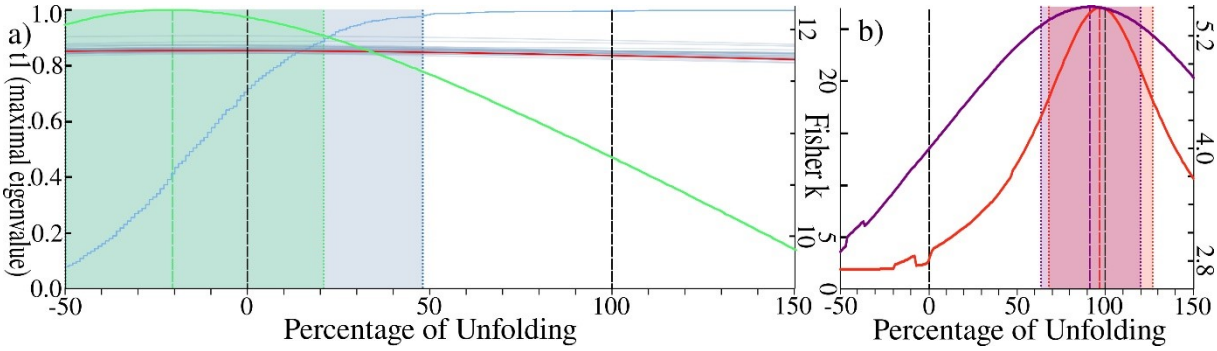

Figure 2.5: Fold tests applied on component B data from Argana (ARG) basin. For conventions and further explanations see caption of Fig. 1.17 and text.

Hence, the Argana basin might have suffered internal rotational movements. However, the negative results of the parametric fold tests (Fig. 2.5a) might also stem from minor differences in bedding correction field data (Table 2.1). Kent et al. (2021) also highlight homoclinal bedding attitudes associated with Si Mbark ou Mbarek. When applying the McElhinny (1964) fold test on the combined data set (N = 23, k_1 = 16, k_2 = 19.5, Table 2.1) we obtain a ratio of k_2/k_1 = 1.22 < 1.68 yielding a barely negative result. Notably, the Fisher parameters now improve upon untilting despite the larger data size. The negative outcome of the parametric fold tests thus needs to be treated with caution and can also be interpreted as inconclusive given the limitations of the field data and potential errors associated with them.

***Table 2.1**: Summary of important site characteristics and paleomagnetic results from the basin of Argana (ARG) for the high-stability component (Component B). All in all, 58 specimens from 10 sites have been used. Below this study's data set, paleomagnetic results and site characteristics reported in Kent et al. (2021) are also given as a reference, i.e. 26A – 28C from the Si Mbark Ou Mbarek locality close to the sampling area of this study, PT2Ma – PT2P from the Sanaga locality and PT2A-PT2L from the locality of Ida Ou Kess Issar. Finally, an overall mean direction integrating both data sets is calculated and as well given in bold characters. For details see text and caption of Table 1.1.*

	Site characteristics							In situ (geographic)				Tectonic (bedding corrected)			
Name	n/N	Age [Ma]	Lithology	Dip Dir. [°]	Dip [°]	GLat [°N]	GLon [°E]	Dec [°]	Inc [°]	a95 [°]	k	Dec [°]	Inc [°]	a95 [°]	k
ARG1	6/6	274.37 – 251.9	Red beds	313	34	30.853335	-8.996807	148.1	-51.5	11	38.2	142.8	-18.2	11	38.2
ARG2	6/6	274.37 – 251.9	Red beds	305	35	30.854256	-8.997195	157.8	-45.7	7.6	78.7	148	-14.4	7.6	78.7
ARG3	6/6	274.37 – 251.9	Red beds	300	28	30.857418	-9.005574	138.5	-53.1	3.7	332	132.3	-26	3.7	332
ARG4	6/7	274.37 – 251.9	Red beds	340	42	30.862820	-9.016545	144.9	-30.7	14.6	22.1	146.9	10.1	14.6	22.1
ARG5	6/6	274.37 – 251.9	Red beds	305	19	30.862849	-9.016906	122.8	-38.9	14.1	23.7	123.2	-19.9	14.1	23.7
ARG6	5/6	274.37 – 251.9	Red beds	300	12	30.862965	-9.016955	177.1	-40	4.7	263	169.9	-32.8	4.7	263
ARG7	7/7	274.37 – 251.9	Red beds	325	21	30.865418	-9.022039	127.4	-25.1	10.9	31.6	129.1	-4.9	10.9	31.6
ARG8	6/6	274.37 – 251.9	Red beds	336	29	30.865165	-9.022514	145.7	-35.1	10.7	39.9	147.5	-6.5	10.7	39.9
ARG9	5/6	274.37 – 251.9	Red beds	269	32	30.825874	-9.088108	110.1	-1.5	10.3	55.7	113.1	28.1	10.3	55.7
ARG10*	5/5	274.37 – 251.9	Red beds	275	18	30.826029	-9.087568	150.7	-31.3	17.6	19.9	143.8	-20.2	17.6	19.9
Mean*	**9/10**	**274.37 – 251.9**	**-**	**-**	**-**	**30.85**	**350.97**	**139.8**	**-37.5**	**14.8**	**13.1**	**139.1**	**-10**	**16.1**	**11.1**
26A	2/?	267 – 251.9	Red beds	303.5	33	30.8635	-9.0133	128.5	-41.4	?	88.5	127.3	-8.4	?	88.5
26B	2/?	267 – 251.9	Red beds	315.5	32	30.8640	-9.0130	144.7	-30.9	?	20.8	143.4	0.8	?	20.8
26C	3/?	267 – 251.9	Red beds	313.5	33	30.8623	-9.0117	152.2	-44.6	?	21.4	145.8	-12.3	?	21.4
26D	3/?	267 – 251.9	Red beds	324.5	24	30.8623	-9.0117	137.7	-38.1	?	27.5	130.9	-14.9	?	27.5
26E	2/?	267 – 251.9	Red beds	345.5	13	30.8655	-9.0207	131.8	-27.7	?	200	134.6	-16.7	?	200
28A	2/?	267 – 251.9	Red beds	302.5	14	30.8647	-9.0242	121.3	-28.4	?	237.6	121.4	-14.4	?	237.6
28B*	1/?	267 – 251.9	Red beds	298.5	22	30.8667	-9.0255	106.6	-49.8	?	-	109.9	-28.2	?	-
28C	3/?	267 – 251.9	Red beds	309.5	27	30.8665	-9.0277	117.2	-50.2	?	30.5	119.6	-21.2	?	30.5
$PT2Ma^N$	4/?	267 – 251.9	Red beds	25.5	27	30.7292	-9.1040	309	35.6	?	29	324.2	25.6	?	29
$PT2Mb^N$	3/?	267 – 251.9	Red beds	142.5	26	30.7293	-9.1040	330.8	-12.3	?	183.4	330.8	13.5	?	183.4
$PT2N^N$	5/?	267 – 251.9	Red beds	333.5	35	30.7290	-9.1040	328	42.5	?	84	329.4	7.6	?	84
$PT2P^N$	2/?	267 – 251.9	Red beds	305.5	41	30.7295	-9.1048	318.3	61.8	?	49.6	311.9	21.2	?	49.6
$PT2A^N$	6/?	267 – 251.9	Red beds	322.5	27	30.6465	-9.1877	321.3	39.7	?	12.9	321.6	12.7	?	12.9
$PT2B^N$	4/?	267 – 251.9	Red beds	341.5	21	30.6503	-9.1845	311.7	31.8	?	58.6	315.7	13.2	?	58.6
$PT2L^N$	2/?	267 – 251.9	Red beds	334.5	33	30.6475	-9.1878	350.8	35.5	?	56.9	347.7	3.6	?	56.9
Mean all	**23/25**	**269.9 – 251.9**	**-**	**-**	**-**	**30.81**	**350.94**	**139.3**	**-36.9**	**7.8**	**16**	**139.5**	**-12.3**	**7.0**	**19.5**

2.2 Souss (Ida Ou Ziki - ZIKI - and Ida Ou Zal - ZAL)

The late Pennsylvanian submontaneous Souss basin is located about 50 km east of Agadir and represents the southwestern-most occurrence of late Paleozoic continental clastic sediments in the WHA reaching a maximum thickness of 1800 m (Figs. 2.1, 2.2). It consists of two sub-basins, namely Ida Ou Ziki (ZIKI) and Ida Ou Zal (ZAL), which originally formed as a single basin and were tectonically separated after the early Stephanian (Kasimovian) and before the late middle Permian (potentially Capitanian) by sinistral shearing along the west branch of the Tizi N'Test Fault at the end of the Mauritanid phase of the Variscan orogeny in Morocco. The late Pennsylvanian deposits of both sub-basins directly rest on the Variscan deformed and metamorphized basement and are unconformably overlain by the Ikakern formation, mid-late Permian continental red beds of the Argana basin (Fig. 2.2; Belahmira et al., 2019; Hmich et al., 2006; Lagnaoui et al., 2018; Saber and El Wartiti, 1996; Saber et al., 2007; Werneburg et al., 2019).

The late Carboniferous sedimentary succession of the Souss basin includes basal fining-upward conglomerates of the Tajgaline formation in ZIKI and of the Ikhourba formation in ZAL which are overlain by more than 1200 m of thick gray, braidplain sediments comprising lacustrine black shales, fluvial sandstones and up to decimeter thick coal seams (Fig. 2.2). These are represented by the Oued Issene formation in ZIKI and the El Menizla formation in ZAL, respectively cropping out in 5 x 15 km and 2 x 6 km large areas (Fig. 2.6; Belahmira et al., 2019; Hmich et al., 2006; Lagnaoui et al., 2018; Werneburg et al., 2019).

The Oued Issene formation and the El Menizla formation contain a diverse assemblage of fossil biotic remains, such as invertebrates, insects, plants, small actinopterygian fish and tetrapod footprints (Belahmira et al., 2015; Belahmira et al., 2019; Hmich et al., 2006; Lagnaoui et al., 2018; Werneburg et al., 2019). By means of biostratigraphy of the preserved entomofauna, Hmich et al. (2006) determined the age of the fossiliferous strata of these formations as Stephanian A/B of the West European Regional Scale and were able to directly correlate these with a late Kasimovian to middle Gzhelian age, i.e. roughly 305 – 301 Ma (Aretz et al., 2020).

In the ZIKI sub-basin, we recovered 42 cores from seven sites of the Oued Issene formation close to Tanamert village (41 could be paleomagnetically measured) whereas in the ZAL sub-basin, 51 cores at nine sites from the El Menizla formation could be extracted at the mountain road from El Menizla to Agadir Ou Anzizen (Fig. 2.6, Tables 2.2, 2.3). Because no radioisotopic age constraint is available so far and the Stephanian age of the Oued Issene and El Menizla formations was recently confirmed by Lagnaoui et al. (2018), a late Kasimovian to middle Gzhelian age is assumed for all samples taken in the Souss basin (Tables 2.2, 2.3).

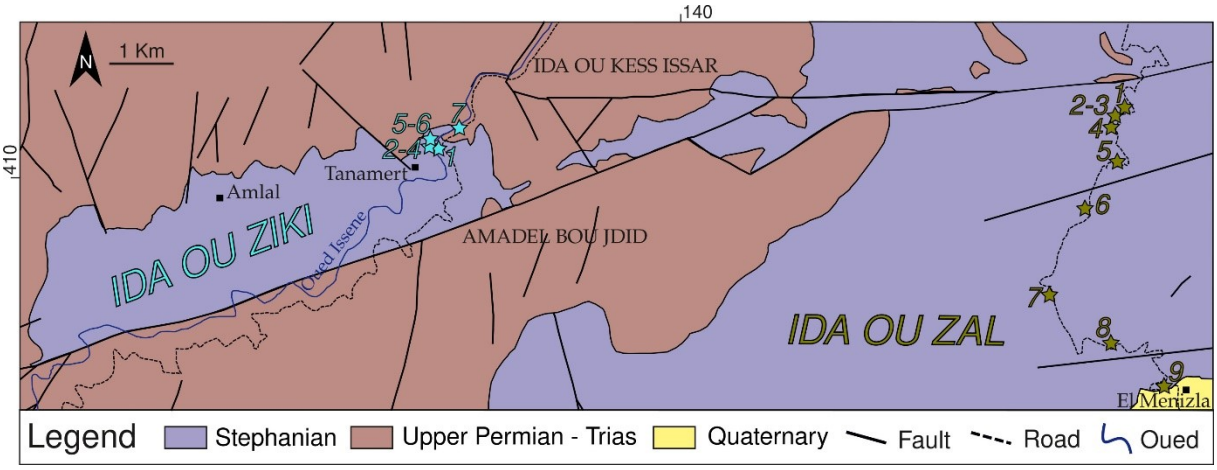

Figure 2.6: Simplified geological map of the Souss basin resp. the two sub-basins Ida Ou Ziki (ZIKI) and Ida Ou Zal (ZAL), based on the geological map of Morocco – sheet Argana / Western High Atlas (1/100000), model completed in 1971 and published in 1974 after Abdelkader Benslimane (1974). Light blue (brown) stars specify this work's paleomagnetic site positions from Ida Ou Ziki (Ida Ou Zal). Numbering of samples correlate with Tables 2.2 (ZIKI) and 2.3 (ZAL). For further explanations see legend.

For the subbasin of ZIKI, all of the well-defined site-mean directions cluster around the recent geomagnetic field of Morocco (D = 358.4°, I = 44.1°; using the IGRF2020 model like in Fig. 1.15) in geographic coordinates which disperse when rotated into tectonic coordinates (Fig. 2.7a) also associated with a significant deterioration of the Fisher parameters (Table 2.2). For the subbasin of ZAL, a distinct directional scatter is observed for both the in situ and the bedding corrected reference frame (Fig. 2.7b), which is why no reliable basin-mean direction can be calculated (Table 2.3). The magnetic signal from the Souss basin is therefore interpreted to be of secondary origin and will be not discussed further.

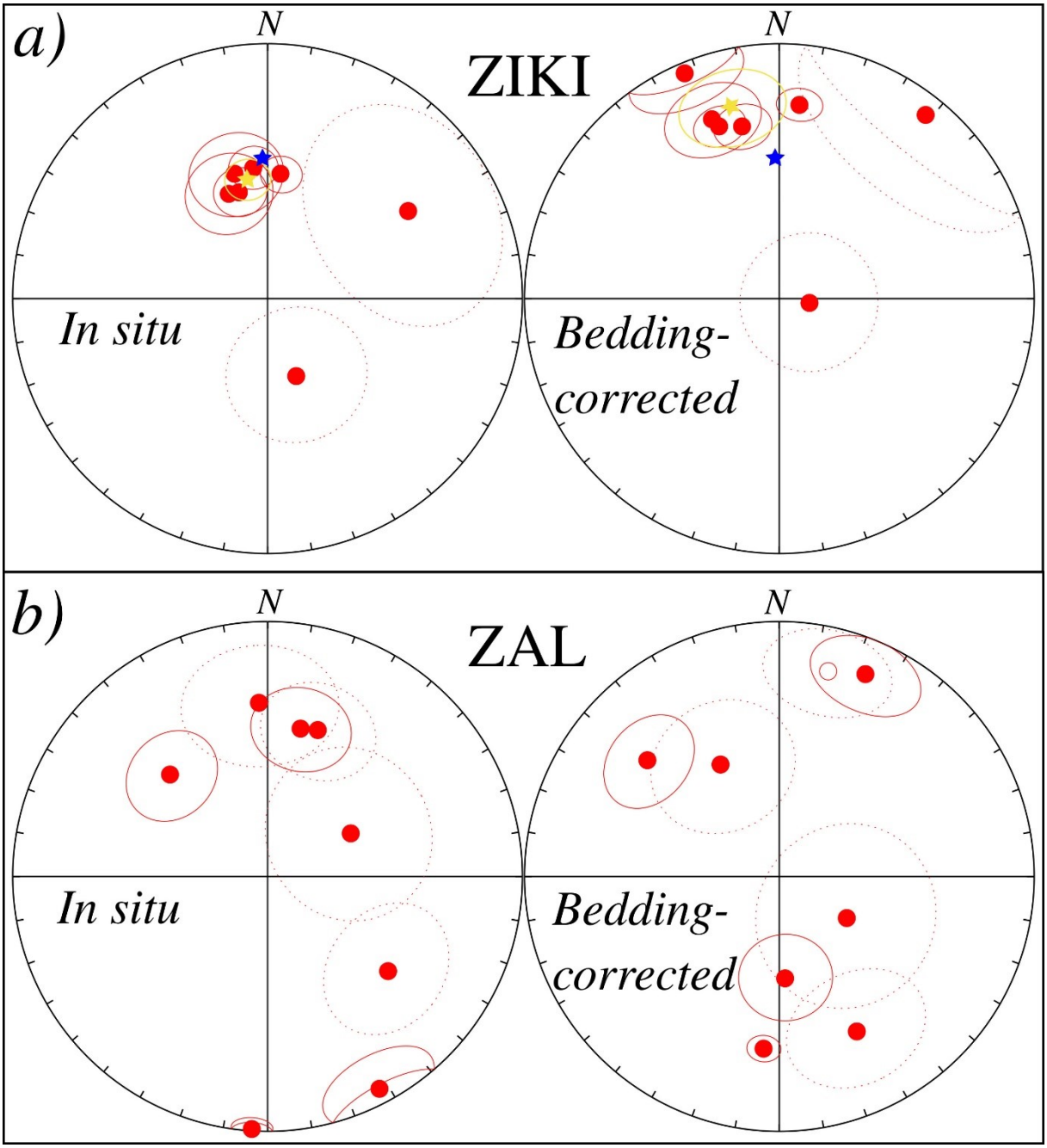

Figure 2.7: Stereographic equal-area projection of site-mean (circles) and basin-mean (stars) directions from the Ida Ou Ziki (ZIKI) subbasin (a) and the Ida Ou Zal (ZAL) subbasin (b) within the Souss basin in geographic (in situ) and tectonic (bedding-corrected) coordinates. Blue star in (a) specifies the paleomagnetic direction of the referential present-day field (PDF) for the sampling area in Morocco (D = 358.4°, I = 44.1°) following Fig. 1.15. Numerical values for the shown data can be found in Table 2.2 (ZIKI) and Table 2.3 (ZAL). Due to the large scatter of the site-mean data for ZAL, no basin-mean direction is shown in (b). Conventions as in Fig. 1.16.

***Table 2.2**: Summary of important site characteristics and paleomagnetic results from the (sub)basin of Ida Ou Ziki (ZIKI) within the Souss basin. All in all, 36 specimens from 7 sites have been used. For details see text and caption of Table 1.1.*

	Site characteristics							In situ (geographic)				Tectonic (bedding corrected)			
Name	n/N	Age [Ma]	Lithology	Dip Dir. [°]	Dip [°]	GLat [°N]	GLon [°E]	Dec [°]	Inc [°]	a95 [°]	k	Dec [°]	Inc [°]	a95 [°]	k
ZIKI1[1]	6/6	305 – 301	Siltstone	5	25	30.640867	-9.192002	6.4	49.4	6.2	116.5	5.98	24.5	6.2	116.5
ZIKI2	6/6	305 – 301	Siltstone	339	28	30.641265	-9.193366	339.8	53.7	13.5	25.7	339.6	25.7	13.5	25.7
ZIKI3	4/5	305 – 301	Siltstone	353	23	30.641006	-9.193273	345.6	54.4	8.2	127.9	348	31.5	8.2	127.9
ZIKI4[1]	6/6	305 – 301	Siltstone	305	24	30.640767	-9.193119	353.8	47.1	7.4	84.1	340.9	29.1	7.4	84.1
ZIKI5[1]	6/6	305 – 301	Siltstone	321	46	30.641944	-9.193383	345.8	48.1	14.2	23.2	337.3	4.7	14.2	23.2
ZIKI6*	4/6	305 – 301	Siltstone	1	24	30.641999	-9.193241	159.2	63.3	22.1	18.2	96.9	80.3	22.1	18.2
ZIKI7*	4/6	305 – 301	Siltstone	347	52	30.642742	-9.189538	58.3	34.9	33.5	8.5	38.7	8.3	33.5	8.5
Mean	**5/7**	**305 – 301**	**-**	**-**	**-**	**30.64**	**350.81**	**350.6**	**50.9**	**6.9**	**123.2**	**346.1**	**23.5**	**14.5**	**28.8**

***Table 2.3**: Summary of important site characteristics and paleomagnetic results from the (sub)basin of Ida Ou Zal (ZAL) within the Souss basin. All in all, 36 specimens from 9 sites have been used. For details see text and caption of Table 1.1.*

	Site characteristics							In situ (geographic)				Tectonic (bedding corrected)			
Name	n/N	Age [Ma]	Lithology	Dip Dir. [°]	Dip [°]	GLat [°N]	GLon [°E]	Dec [°]	Inc [°]	a95 [°]	k	Dec [°]	Inc [°]	a95 [°]	k
ZAL1[1]*	6/7	305 – 301	Siltstone	225	32	30.648978	-9.088810	357.5	32.4	22.2	10.1	332.8	49.1	22.2	10.1
ZAL2[1]*	0/6	305 – 301	Siltstone	243/002	44/16	30.647955	-9.090067	-	-	-	-	-	-	-	-
ZAL3*	3/6	305 – 301	Siltstone	219	34	30.647562	-9.089979	127.9	39.7	20.4	37.7	153.2	32.5	20.4	37.7
ZAL4[1]	5/6	305 – 301	Siltstone	287	14	30.644900	-9.090060	316.4	44.3	14.4	29.1	311.4	31.8	14.4	29.1
ZAL5	5/6	305 – 301	Siltstone	56	32	30.641352	-9.089821	12.9	40.2	14.7	28.1	23.4	14.6	14.7	28.1
ZAL6	6/6	305 – 301	Siltstone	355	32	30.636084	-9.093964	183.5	1	4.8	197.8	185.1	32.6	4.8	197.8
ZAL7	6/6	305 – 301	Siltstone	308	60	30.623999	-9.098974	152.2	6.2	14.4	22.7	176.5	57.1	14.4	22.7
ZAL8*	3/6	305 – 301	Siltstone	190/189	28/32	30.617671	-9.089660	62.4	59.7	27.3	21.4	120.8	64.3	29.3	18.7
ZAL9*	2/2	305 – 301	Siltstone	349	63	30.612773	-9.082029	19.3	39	16.9	219.4	13.4	-18.2	16.9	219.4
Mean*	**4/9**	**305 – 301**	**-**	**-**	**-**	**30.64**	**350.91**	**172.6**	**67.1**	**-**	**1.3**	**283.1**	**82**	**116**	**1.7**

2.3 Ourika (OUR)

In the Oukaimeden-Ourika valley, located in a Central High Atlas basin about 40 km SE of Marrakech, continental fluvial-dominated Permian and Triassic sediments are well exposed in an active-rift setting (Figs. 2.1; Baudon et al., 2009; Biron and Courtinat, 1982).

The Permo-Triassic series in the Central High Atlas has been divided into six formations, based on lithology and the identification of major discontinuities (Figs. 2.2, 2.8; Benaouiss et al., 1996; Biron and Courtinat, 1982; Mattis, 1977). Due to a lack of an angular unconformity between Permian and Triassic rocks, and limited dating of this dominantly continental succession (Beauchamp, 1988), the age of the series is only poorly constrained by available paleontological (e.g., Dutuit, 1976; Jalil and Janvier, 2005), palynological (Cousminer and Manspeizer, 1976; Olsen et al., 2000) and radiometric data (Van Houten, 1977).

Formations F1 (Anrar Conglomerate) and F2 (Cham-El-Houa Siltstone) are more than 500 meter-thick and comprise mainly conglomerates and red beds which were dated as Permian in age (Biron, 1983; Dutuit, 1976; Van Houten, 1977). A new and diverse ichnoassemblage (vertebrate and invertebrate) from the Permian of Zat Valley in Marrakech High Atlas was recently described by Moreau et al. (2020). The new tracksite was found in the Tighadwiyn region, in the middle late Permian of the Cham-El-Houa Siltstone formation (F2). This ichnoassemblage shares strong similarities with those reported by Hminna et al. (2012) from the T2 member of the Ikakern Formation (see chapter 2.1). Perez et al. (2019) recently performed Pb/U LA-ICP-MS datings of the formations F1 and F2 in the south-western part of the Ourika-Zat anticline, about 20 km west from the Moreau et al. (2020) tracksite: the calculated ages of both F1 and F2 are mostly from the middle Permian, possibly late Permian for the youngest zircons.

Early or Middle Triassic sediments have not yet been recorded in the Central High Atlas Basin (Cousminer and Manspeizer, 1976). Formations F3 to F6 have been dated as Late Triassic in age (Biron and Courtinat, 1982; Cousminer and Manspeizer, 1976). In the Oukaimeden-Ourika Valley, they rest with a major angular unconformity onto Palaeozoic basement rocks, which were strongly deformed by the Hercynian orogeny (Baudon et al., 2009).

In the valley of OUR, we drilled 36 cores at six sites of the F1 formation at the road between the villages Anrar and Asguine near the Ourika river (Fig. 2.8, Table 2.4). Taking all available age constraints into consideration, we assume a middle to late Permian age of F1 (and

F2) and hence ascribe our samples an age of 274.37 – 251.9 Ma following Henderson et al. (2020).

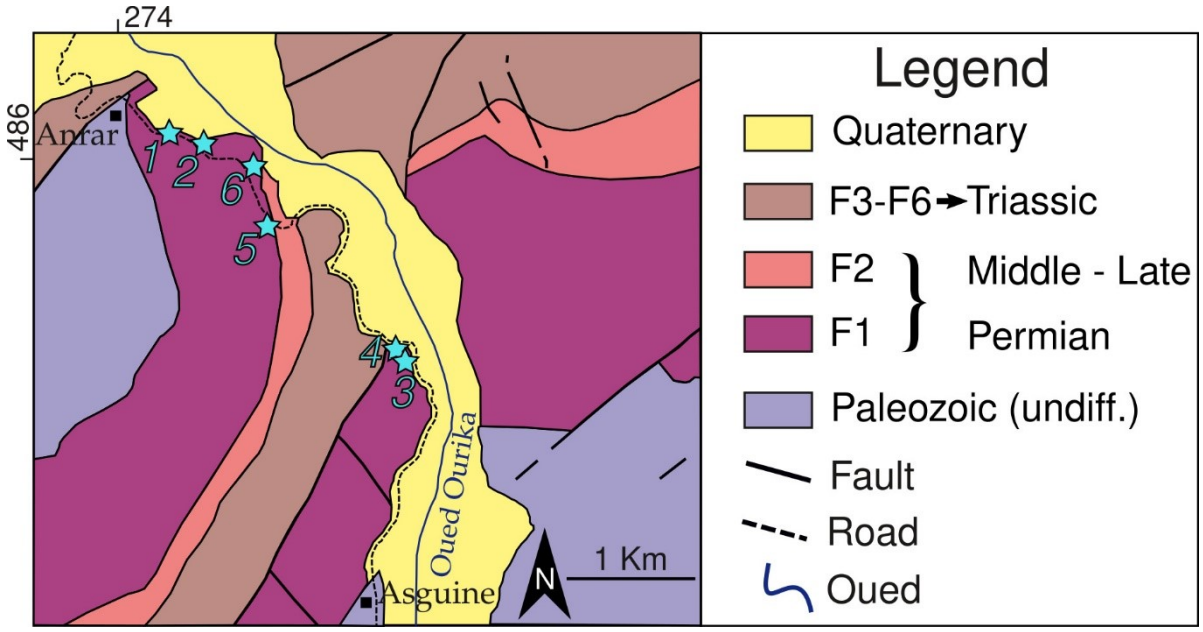

Figure 2.8: Simplified geological map of the Ourika basin (OUR), based on the geological map of Morocco – sheet Tahanaoute (1/50000), model completed in 2002 and published in 2016 after Angoud (2016a), modified in accordance with Perez et al. (2019). Light blue stars specify this work's paleomagnetic site positions. Numbering of samples correlate with Table 2.4. For further explanations see legend and text.

The paleomagnetic data from the Ourika basin appears erratic before and after field correction (Fig. 2.9) and no significant common mean direction can be calculated (Table 2.4). Hence, no primary signal has been preserved within the samples and the data is discarded.

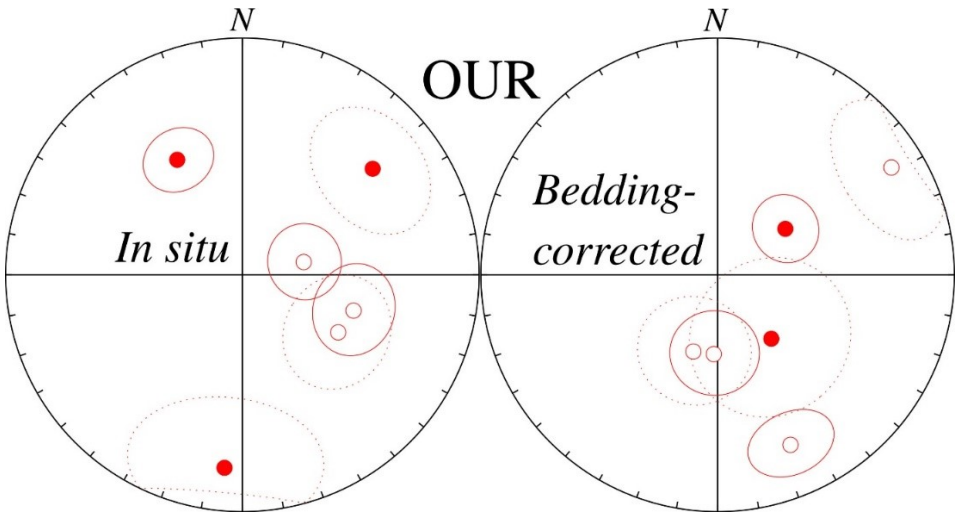

Figure 2.9: Stereographic equal-area projection of site-mean directions (circles) from the Ourika basin (OUR) in geographic (in situ) and tectonic (bedding-corrected) coordinates. Numerical values for the shown data can be found in Table 2.4. Due to the large scatter of the site-mean data, no basin-mean direction is shown. Conventions as in Fig. 1.16.

***Table 2.4**: Summary of important site characteristics and paleomagnetic results from the Ourika (OUR) basin for the high-stability component (Component B). All in all, 34 specimens from 6 sites have been used. For details see text and caption of Table 1.1.*

	Site characteristics							In situ (geographic)				Tectonic (bedding corrected)			
Name	n/N	Age [Ma]	Lithology	Dip Dir. [°]	Dip [°]	GLat [°N]	GLon [°E]	Dec [°]	Inc [°]	a95 [°]	k	Dec [°]	Inc [°]	a95 [°]	k
OUR1[1]	6/6	274.37 – 251.9	Red beds	0	70	31.356136	-7.771651	78	-68	12.8	28.2	156.4	-23	12.8	28.2
OUR2*	4/6	274.37 – 251.9	Red beds	35	60	31.355404	-7.769727	185.2	19.1	27.7	12	140	60.9	27.7	12
OUR3[1]*	6/6	274.37 – 251.9	Red beds	80	45	31.344562	-7.756240	121.1	-50.9	19.1	13.2	197.1	-62.2	19.1	13.2
OUR4*	6/6	274.37 – 251.9	Red beds	105	65	31.345079	-7.756945	50.8	29.7	20.9	11.2	58.3	-14.6	20.9	11.2
OUR5	6/6	274.37 – 251.9	Red beds	116	56	31.351315	-7.765097	330.9	43.5	11.5	34.8	55.8	61.4	11.5	34.8
OUR6[1]	6/6	274.37 – 251.9	Red beds	68	46	31.354302	-7.766852	107.4	-48.8	15	21	182.2	-62.7	15	21
Mean	**3/6**	**274.37 – 251.9**	**-**	**-**	**-**	**31.35**	**352.23**	**51.3**	**-50.3**	**-**	**1.2**	**144.1**	**-17.4**	**-**	**1.2**

***Table 2.5**: Summary of important site characteristics and paleomagnetic results from the Sebt Brikiyne massif (BRI) for the high-stability component (Component B). All in all, 40 specimens from 7 sites have been used. For details see text and caption of Table 1.1.*

	Site characteristics							In situ (geographic)			
Name	n/N	Age [Ma]	Lithology	Dip Dir. [°]	Dip [°]	GLat [°N]	GLon [°E]	Dec [°]	Inc [°]	a95 [°]	k
BRI1[1]	5/5	271.1 ± 9.1	Granite	0	0	32.358054	-8.131960	173.1	-43.3	6	163.5
BRI2	6/6	271.1 ± 9.1	Granite	0	0	32.325873	-8.089297	126	35.2	15.5	19.7
BRI3[1]	6/7	271.1 ± 9.1	Granite	0	0	32.287793	-8.052953	167.1	-40.5	2.6	666.8
BRI4	6/6	271.1 ± 9.1	Granite	0	0	32.297934	-8.013609	123.2	1.4	7.8	75.9
BRI5*	6/6	271.1 ± 9.1	Granite	0	0	32.360463	-8.145164	136.3	-29.4	22.7	9.7
BRI6*	6/6	271.1 ± 9.1	Granite	0	0	32.359437	-8.145189	138.9	27.3	29.6	6.1
BRI7*	5/7	271.1 ± 9.1	Granite	0	0	32.362887	-8.132791	142.6	-30.4	34.8	5.8
Mean*	**4/7**	**280.2 – 262**	**-**	**-**	**-**	**32.32**	**351.93**	**144.8**	**-13.6**	**58.2**	**3.5**

2.4 Sebt Brikiyne (BRI)

The Sebt Brikiyne granite is an about 250 km^2 large circular-shaped plutonite constituting a topographic depression in the southern part of the Rehamna massif NW of Ben Guerir city (Figs. 2.1, 2.10). It protrudes the Early-Middle Cambrian sediments of the coastal block/western Rehamna and the central Rehamna as well as the sedimentary metamorphic units of the Visean-Ordovician (e.g. Chopin et al., 2014). The vast recent quaternary cover masks a significant part of the massif (around 25%) which is predominantly cropping out in the eroded banks of valleys and respective slops near the road (Diot, 1989).

Radioistopic dating for BRI provided Rb/Sr ages of 278 ± 2 Ma (Tisserant (1977) in Hoepffner (1982)) and 268 ± 6 Ma (Mrini, 1985; Mrini et al., 1992) as well as a recent $^{40}Ar/^{39}Ar$ age of 274.8 ± 5.4 Ma (Chopin et al., 2014). BRI is therefore interpreted to be a "late- to post-orogenic", granitic massif for the western Meseta with an age comparable to that of Oulmès or Ment, or even to the two micas facies of Zaer in the Central massif (Chopin et al., 2014; Diot, 1989; Diot and Bouchez, 1991).

In sum, 43 cores from seven sites in the BRI massif were taken (Fig. 2.10, Table 2.5). Due to the fact, that the given absolute age constraints are not all fulfilling modern laboratory standards but nevertheless agree well, we calculated an arithmetic mean emplacement age for BRI (and thus for our samples) at 271.1 ± 9.1 Ma (Fig. 2.2).

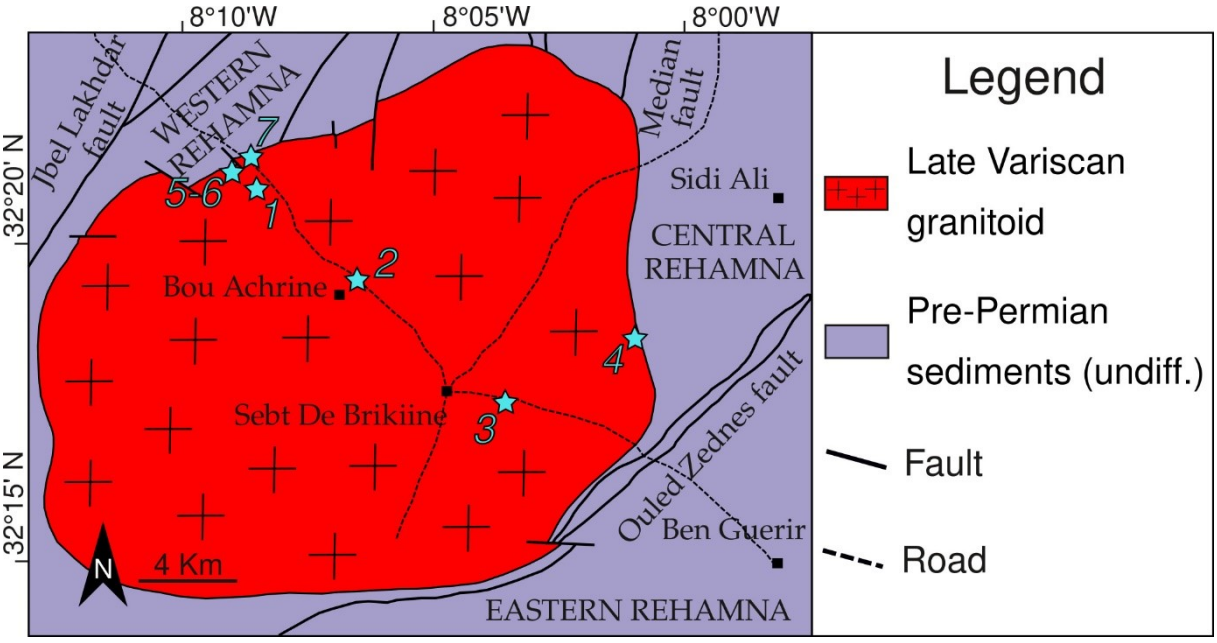

Figure 2.10: Simplified geological map of the sampled area in the Sebt Brikiyne massif (BRI), redrawn and modified from Diot (1989) after Chopin et al. (2014). Light blue stars specify paleomagnetic site positions of this work. Numbering of samples correlate with Table 2.5. For further explanations see legend.

The acquired paleomagnetic directions from the BRI massif plot in the SE quadrant and straddle the horizontal with both moderate positive and negative inclinations (Fig. 2.11). However, most of the site-mean data is characterized by a large scatter which is why no well-defined mean direction can be determined for the BRI massif, albeit individual sites (e.g., BRI4) plot close to the expected paleomagnetic direction of the late Paleozoic (Table 2.5). Even though the BRI data set in its entirety is not suited to be further discussed in the course of this thesis, its results shall act as an encouragement to enlarge the available data set in further studies.

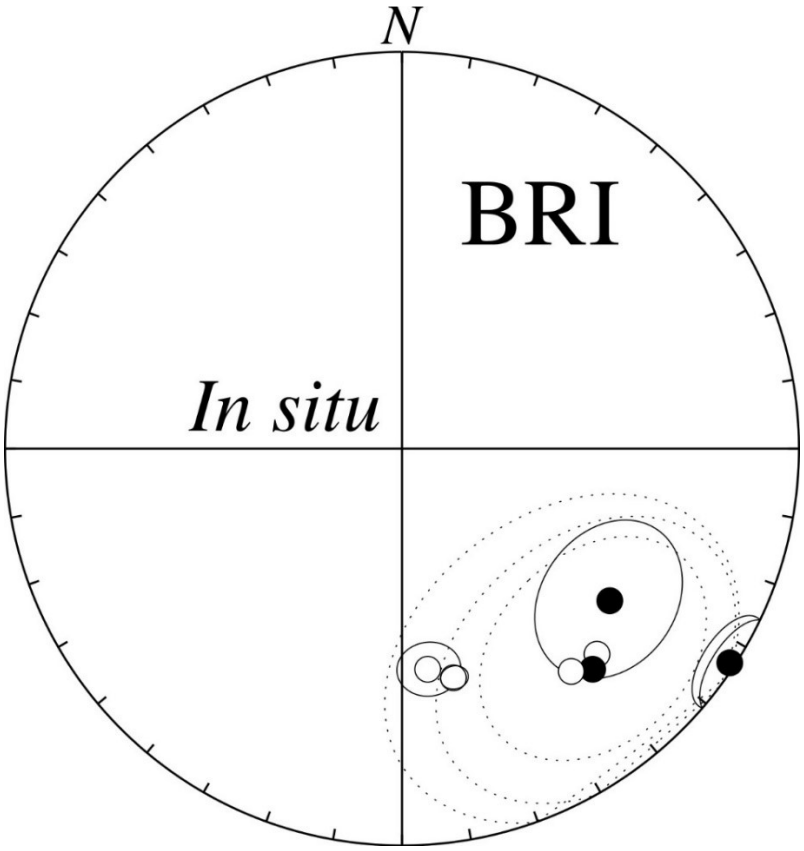

Figure 2.11: Stereographic equal-area projection of in-situ site-mean (circles) directions from the Sebt Brikiyne massif (BRI). Numerical values for the shown data can be found in Table 2.5. Due to the large scatter of the site-mean data, no BRI-mean direction is shown. Conventions as in Fig. 1.16.

2.5 Zaer (ZAE)

The Hercynian Zaer granite represents the major magmatic intrusive body of the Central Massif with an elongated ellipsoidal shape in the NE-SW direction. It protrudes the prevalent, weakly metamorphized Ordovician-Devonian sedimentary layers and schists covering a surface area of 400 km^2 (Figs. 2.1, 2.12; Diot, 1989; Haïmeur et al., 2004).

The Zaer pluton is made up of two granitic units, distinguished as external and internal according to their emplacement age. The older, external unit cropping out in an NE-SW elongated, ~ 220 km^2 large area displays a heterogenous, biotite-rich granitoid character with an abundance of enclaves, while the younger, internal unit intruded in the former and consists of two-micas leucogranites with enclave-free and homogeneous affinities covering a subcircular area of ~ 180 km^2. The external unit can further be partitioned into two facies, with strongly hybrid granodiorite-tonalites (including large-preserved xenoliths and mafic microgranular enclaves) being predominant in the SW and comparatively homogeneous, more differentiated monzogranite-granodiorites (with many small, evolved xenoliths and mafic microgranular enclaves) dominating in the NE of ZAE (Fig. 2.12; Diot, 1989; Haïmeur et al., 2004).

According to the petrogenetic model of Haïmeur et al. (2004), the emplacement of the Zaer massif has happened in three temporally separated episodes. Initially, the external unit formed by the intrusion of the granodiorite-tonalite in the SW closely followed by the monzogranite-granodiorites in the NE. After a long magma storage with significant mixing processes, the homogeneous leucogranites of the internal unit were finally injected into the external unit covering the central and southeastern parts of ZAE.

The first radiometric studies on ZAE yielded averaged ages ranging from 298 ± 3 Ma to 284 ± 15 Ma (Giuliani, 1982; Giuliani et al., 1989; Haïmeur et al., 2004). Whole-rock Rb/Sr dating by Mrini (1985) and Mrini et al. (1992) yielded emplacement ages of 303 ± 13 Ma for the external unit and 279 ± 11 Ma for the internal unit. From the leucogranites of the internal unit, we were only able to collect twelve samples at two sites in the SE of ZAE due to the difficult drilling conditions in the field (Fig. 2.12). Because of the temporal correlation of BRI (assigned age range: 271.1 ± 9.1 Ma, cf. chapter 2.4) with the leucogranites of ZAE, we utilize the temporally closest available age constraint and ascribe our samples an age of 279 ± 11 Ma (Table 2.6).

Apart from one directionally dispersed site (ZAE1), ZAE2 exhibits a well-defined site-mean direction pointing towards the SE and shallowly down (Fig. 2.13) close to the reliable site BRI4 from the Sebt Brikiyne massif which is also ascribed a similar emplacement age (Tables 2.5 and 2.6). Due to the sparse available data set from ZAE (N = 1), no valid conclusions can be drawn for ZAE within the scope of this thesis. However, further paleomagnetic data acquisition within the Zaer massif seems promising for future studies.

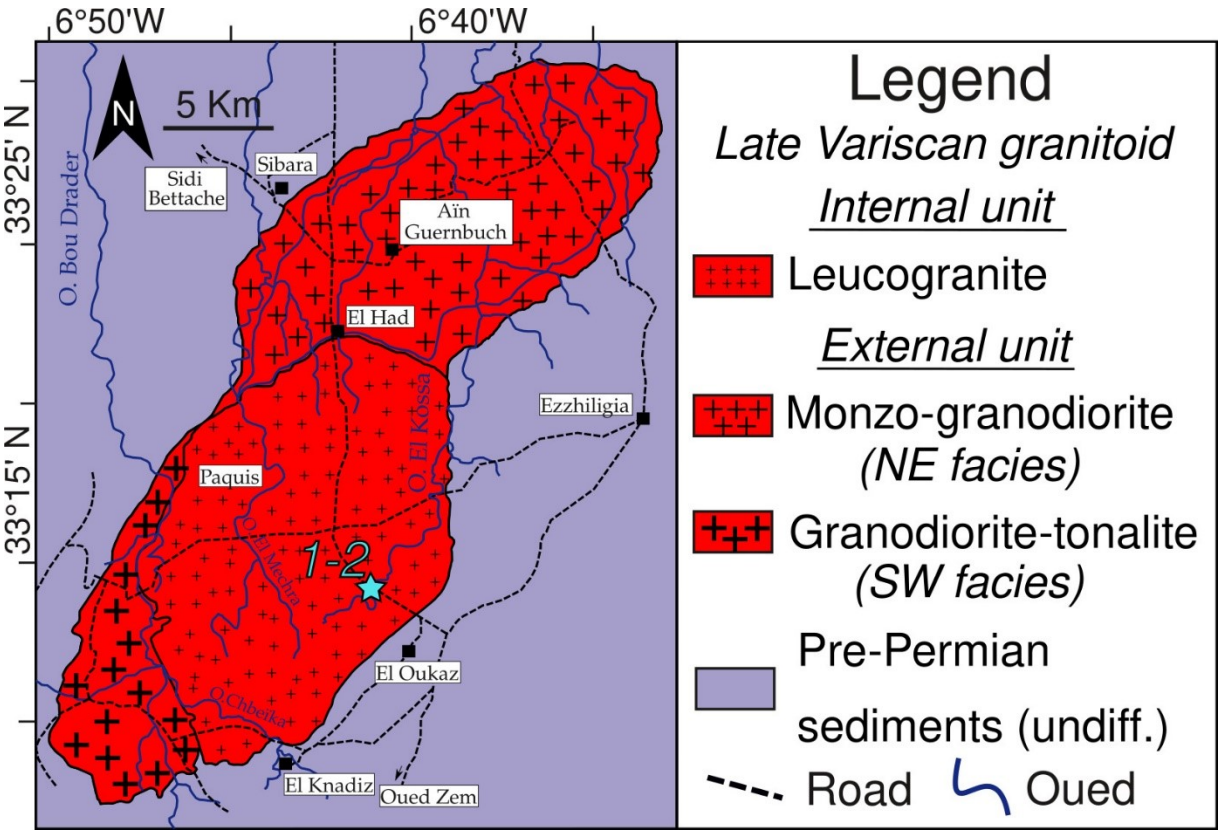

Figure 2.12: Simplified geological map of the sampled Zaer massif (ZAE), redrawn and modified from Haïmeur et al. (2004). Light blue stars specify paleomagnetic site positions of this work. Numbering of samples correlate with Table 2.6. For further explanations see legend.

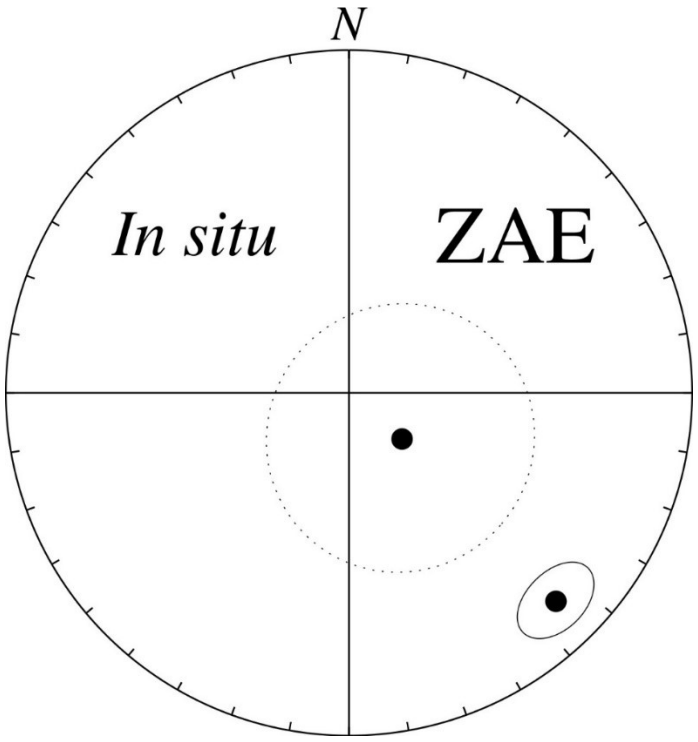

Figure 2.13: Stereographic equal-area projection of in-situ site-mean directions (circles) from the Zaer massif (ZAE). Numerical values for the shown data can be found in Table 2.6. Due to the low number of reliable sites (N = 1 < 3), no ZAE-mean direction is shown. Conventions as in Fig. 1.16.

***Table 2.6**: Summary of important site characteristics and paleomagnetic results from the Zaer granite (ZAE) for the high-stability component (Component B). All in all, 9 specimens from 2 sites have been used. For details see text and caption of Table 1.1.*

			Site characteristics					In situ (geographic)			
Name	n/N	Age [Ma]	Lithology	Dip Dir. [°]	Dip [°]	GLat [°N]	GLon [°E]	Dec [°]	Inc [°]	a95 [°]	k
ZAE1*	3/6	279 ± 11	Leucogranite	0	0	33.242671	-6.676403	131.3	73.1	32.1	15.8
ZAE2	6/6	279 ± 11	Leucogranite	0	0	33.242671	-6.676403	135.2	15.4	8.6	61.5
Mean*	**1/2**	**290 – 268**	**-**	**-**	**-**	**32.24**	**353.32**	**135.2**	**15.4**	**8.6**	**61.5**

***Table 2.7**: Summary of important site characteristics and paleomagnetic results from the Sidi Kassem basin (KASS) for the high-stability component (Component B). All in all, 38 specimens from 7 sites have been used. For details see text and caption of Table 1.1.*

			Site characteristics					In situ (geographic)				Tectonic (bedding corrected)			
Name	n/N	Age [Ma]	Lithology	Dip Dir. [°]	Dip [°]	GLat [°N]	GLon [°E]	Dec [°]	Inc [°]	a95 [°]	k	Dec [°]	Inc [°]	a95 [°]	k
KASS1	5/6	323.4 – 307.02	Sandstone	255	20	33.312902	-6.472207	145.6	35.1	3.9	388.5	160.7	39.3	3.9	388.5
KASS2*	4/6	323.4 – 307.02	Sandstone	280	12	33.315549	-6.466416	145.5	4.6	16.4	32.4	146.9	12.9	16.4	32.4
KASS3^{O}*	5/6	323.4 – 307.02	Sandstone	295	5	33.315351	-6.467149	57.4	57.8	0.9	6608.9	50.1	60.2	0.9	6608.9
KASS4	6/6	323.4 – 307.02	Sandstone	233	13	33.320040	-6.461774	140.8	36.6	13.4	25.8	150.4	36	13.4	25.8
KASS5 ^{O}*	6/6	323.4 – 307.02	Sandstone	155	50	33.326497	-6.470610	3.8	46.7	1.6	1850.6	92.3	68.2	1.6	1850.6
KASS6 ^{O}*	6/6	323.4 – 307.02	Sandstone	168	42	33.326812	-6.471620	7.4	52.6	4.1	262.5	105.6	76.8	4.1	262.5
KASS7*	6/6	323.4 – 307.02	Sandstone	98	8	33.325246	-6.476332	174.1	-3.4	22	10.2	174.6	-5.2	22	10.2
Mean*	**2/7**	**323.4 – 307.02**	**-**	**-**	**-**	**33.32**	**353.53**	**143.2**	**35.9**	**9.1**	**755.5**	**155.4**	**37.8**	**19.3**	**170**

2.6 Sidi Kassem (KASS)

The Pennsylvanian Sidi Kassem Basin crops out about 100 km SE of Rabat in the Central Massif in an NE-SW elongated shape of approximately 30 km length and 6 km width and is the only limnic basin of Westphalian age in Morocco consisting exclusively of continental sediments. KASS formed as an intramontane depression of the Mauretanide segment of the Variscides in the main phase (= Pennsylvanian) of the Hercynian orogeny (Figs. 2.1, 2.14; Lagnaoui et al., 2014).

It has long been known for Paleozoic macrofloral remains (Pruvost and Termier, 1949; Termier, 1936). Its mainly red siliciclastic rocks unconformably rest on the strongly deformed basement of Ordovician to Devonian age. The basin fill is represented by a cumulatively 1,250 m thick succession of alluvio-fluvial to lacustrine deposits of conglomerates, sandstones and mudstones with thin coal seams and freshwater limestones. Recent exploration for fossil tetrapod footprints in floodplain-deposits of the basin revealed a moderately diverse vertebrate ichnofauna (Lagnaoui et al., 2014).

Bensahal (2001) proposed a subdivision of the Westphalian succession (or Sidi Kassem Group *sensu* Razin (2001) into three units. These are from base to top: (1) The Al Keskas formation (~700 m), is volumetrically dominated by red conglomerates with minor amounts of sandstone and mudstone as well as rare intercalations of lacustrine limestones at the top of the unit. The Galmous formation (>300 m), covering most parts of the Sidi Kassem Basin, is composed of greenish, fine-grained to conglomeratic sandstones interbedded with siltstones, claystones and thin coal seams as well as a few lacustrine limestones in the lower part of the unit (Fig. 2.2). The Lgtob Lahmar formation (≥250 m) is restricted to the central part of the basin and overlies the Galmous Formation with still unclear sedimentary or tectonic contact. It is composed of reddish-brown, poorly sorted conglomerates with significant amounts of muddy matrix that have been interpreted as debris flows and mudflows on alluvial fans (Lagnaoui et al. (2014) and references therein).

In the southwestern part of KASS, we recovered 42 drill cores from seven sites of the Galmous formation (Figs. 2.2, 2.14, Table 2.7). The tetrapod ichnofauna of the Sidi Kassem basin suggests a most likely early to mid-Pennsylvanian (Bashkirian-Moscovian) age for the fossiliferous horizons of the Galmous formation (Lagnaoui et al., 2014), i.e. 323.4 – 307.02 Ma (Aretz et al., 2020).

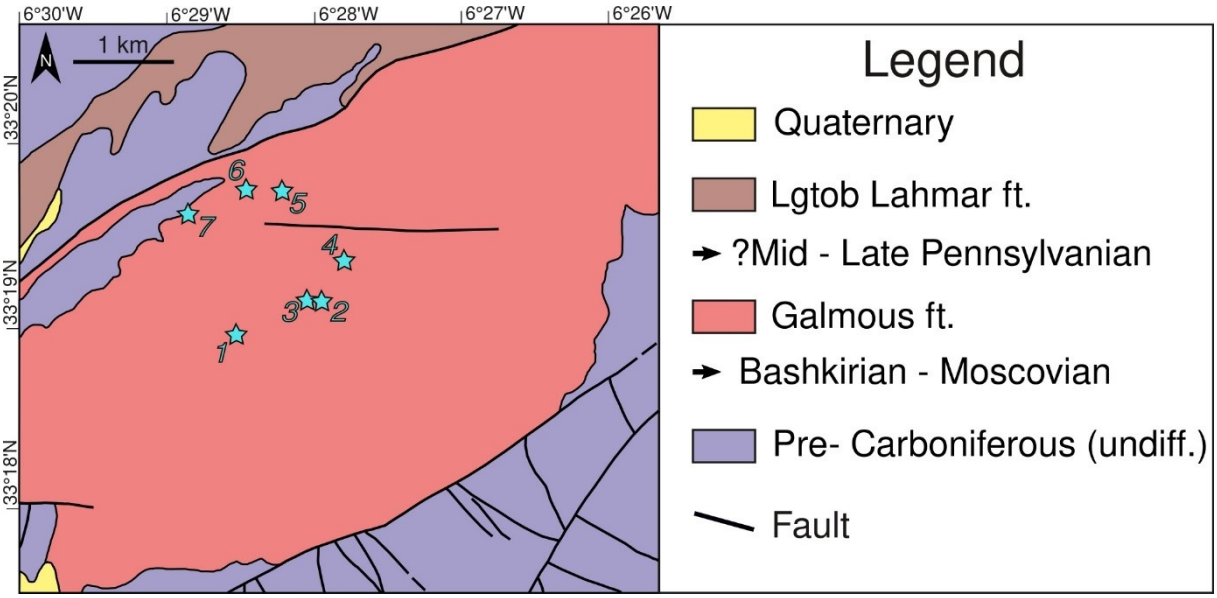

Figure 2.14: Simplified geological map of the southwestern part of the Sidi Kassem basin (KASS), based on the geological map of Morocco – sheet Sidi Matla' Ech Chams (1/50000), model completed in 2000 and published in 2001 after Razin (2001). Light blue stars specify this work's paleomagnetic site positions from Sidi Kassem. Numbering of samples correlate with Table 2.7. For further explanations see legend.

The characteristic remanent magnetization for KASS displays a binary distribution when plotted on a stereographic projection (Fig. 2.15). The first group encompasses the very well-defined site-mean directions of KASS3, KASS5 and KASS6. While KASS3 can be interpreted as an outlier, KASS5 and KASS6 cluster closely to the recent geomagnetic field (see Fig. 1.15) in geographic coordinates while they scatter upon untilting. Because of their strikingly low α_{95} and high k, their magnetic signal is interpreted to be of secondary origin, potentially resulting from an IRM imparted by lightning strokes. The second group (KASS1, KASS2, KASS4, KASS7) plots in the (expected) southeastern quadrant with moderately positive to sub-horizontal inclinations. While KASS1 needs to be treated with caution due to its conspicuously well-defined Fisher parameters (Table 2.7), KASS2 and KASS7 are associated with large uncertainties and thus are discarded. Ultimately, only KASS4 fulfills modern reliability standards. Even if KASS1 is taken into account as well, the low number of sites (N = 2) prevents the determination of a reliable basin-mean direction for KASS (Fig. 2.15). As a consequence, the findings of KASS will not be treated further.

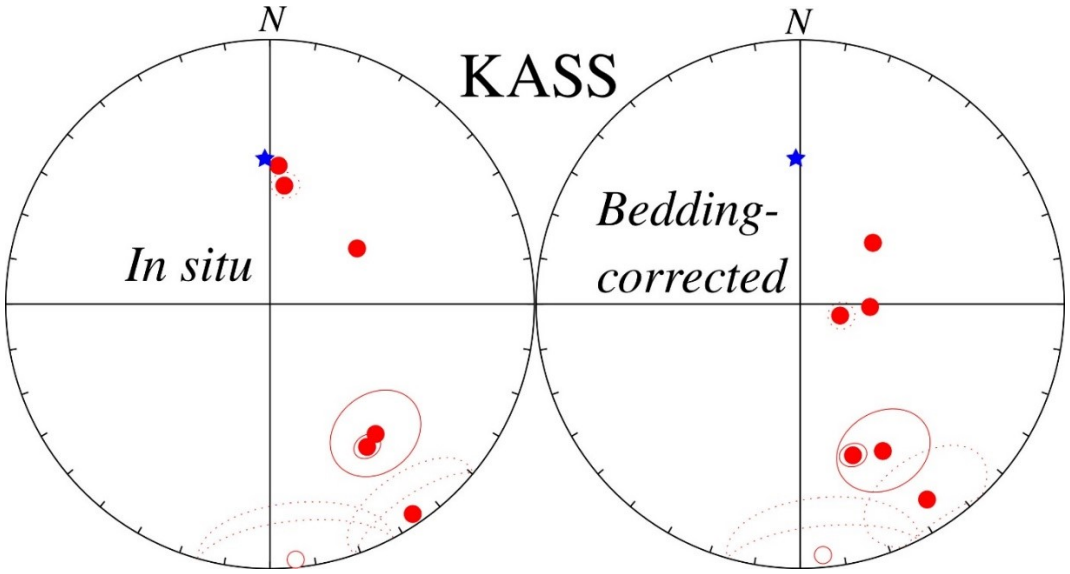

Figure 2.15: Stereographic equal-area projection of site-mean directions (circles) from the Sidi Kassem basin (KASS) in geographic (in situ) and tectonic (bedding-corrected) coordinates. Blue star specifies the paleomagnetic direction of the referential present-day field (PDF) for the sampling area in Morocco (D = 358.4°, I = 44.1°) following Fig. 1.15. Due to the low number of reliable sites (N = 2 < 3), no basin-mean direction is shown. Numerical values for the shown data can be found in Table 2.7. Conventions as in Fig. 1.16.

2.7 Bouterhella (BOUT)

This small, E-W elongated, basin crops out in the north of the Central Massif, with a synclinal structure (Figs. 2.1, 2.16; El Wartiti, 1993). It's about 80 m-thick succession lies unconformably over the Visean-Namurian basement and is made up of fine to coarse-grained reddish clastics which show similarities with those in the Tiddas (Broutin et al., 1987; El Wartiti, 1981; El Wartiti et al., 1986) and Bou Achouch (Termier, 1936) basins. The conglomerates are formed by badly classified pebbles of mainly siliceous, seldom calcareous, silty and rhyolitic nature, poorly organized and typical of proximal parts of an alluvial fan with braided rivers. Sandstone bodies are rare and are associated with more frequent silty-muddy strata which show reddish color and good lateral continuity. A horizon of black claystones, very rich in organic matter provided an early Permian sporomorph association (El Hadi et al., 2014; El Wartiti, 1993), i.e. 298.89 – 274.37 Ma following Henderson et al. (2020).

The Bouterhella basin is intruded by highly altered rhyolites, dolerites, micrograbbros and dacite veins (2 to 4 m thick) which interstratify with the detrital layers (El Hadi et al., 2014; El Wartiti, 1993) and therefore are also assigned a Cisuralian age (Table 2.8). From accessible doleritic dikes outcropping near the road, we recovered 42 samples at seven different sites (Fig. 2.16, Table 2.8).

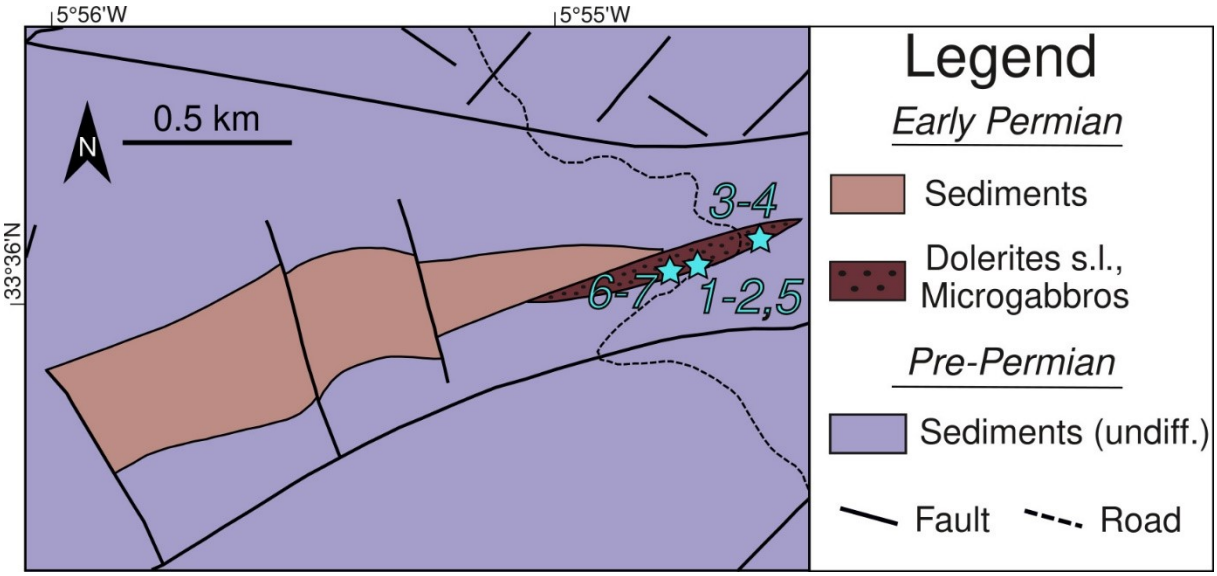

Figure 2.16: Simplified geological map of the Bouterhella basin (BOUT), redrawn from the geological map of Morocco – sheet Bouqachmir (1/50000), model completed in 2000 and published in 2001 after Izart (2001). Light blue stars specify this work's paleomagnetic site positions from Bouterhella. Numbering of samples correlate with Table 2.8. For further explanations see legend.

The samples from the (highly altered) dolerite dikes of BOUT point to the SE quadrant with steeply negative to steeply positive inclinations which are streaked along a girdle after tectonic correction (Fig. 2.17). Due to the erratic behavior between (and within) the sites, a reliable basin-mean direction could not be calculated (Table 2.8). Although some sites (e.g., BOUT7) exhibit promising results close to referential values, the overall scatter entails excluding the data set from further discussion in this study.

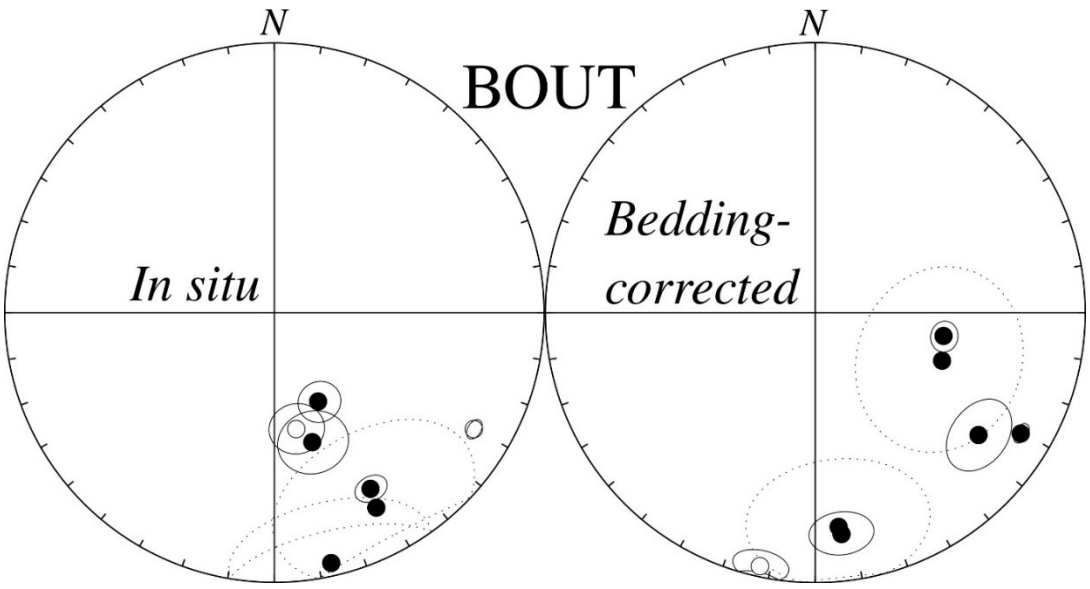

Figure 2.17: Stereographic equal-area projection of site-mean (circles) and basin-mean (stars) directions from the Bouterhella basin (BOUT) in geographic (in situ) and tectonic (bedding-corrected) coordinates. Numerical values for the shown data can be found in Table 2.8. Due to the large scatter of the site-mean data, no basin-mean direction is shown. Conventions as in Fig. 1.16.

Table 2.8: *Summary of important site characteristics and paleomagnetic results from the Bouterhella basin (BOUT) for the high-stability component (Component B). All in all, 36 specimens from 7 sites have been used. For details see text and caption of Table 1.1.*

	Site characteristics							In situ (geographic)				Tectonic (bedding corrected)			
Name	n/N	Age [Ma]	Lithology	Dip Dir. [°]	Dip [°]	GLat [°N]	GLon [°E]	Dec [°]	Inc [°]	a95 [°]	k	Dec [°]	Inc [°]	a95 [°]	k
BOUT1[1]	6/6	298.89 – 274.37	Dolerite	17	60	33.597053	-5.911940	151.2	26.4	4.4	236.4	100.5	49.8	4.4	236.4
BOUT2*	4/6	298.89 – 274.37	Dolerite	17	60	33.597077	-5.911711	152.1	19.6	26.7	12.9	110.7	48.2	26.7	12.9
BOUT3*	4/6	298.89 – 274.37	Dolerite	290	32	33.598517	-5.908032	167	5.3	23.1	16.8	173.8	21.4	23.1	16.8
BOUT4[1]	4/6	298.89 – 274.37	Dolerite	308	28	33.598669	-5.907799	120.3	-15.2	2.5	1344.2	120.4	12.5	2.5	1344.2
BOUT5	6/6	298.89 – 274.37	Dolerite	0	73	33.597032	-5.911590	169.1	-53.8	8	72.1	173.2	18.6	8	72.1
BOUT6	6/6	298.89 – 274.37	Dolerite	220	82	33.596662	-5.912776	153.2	59.6	6.3	114.6	192.2	-4.5	6.3	114.6
BOUT7	6/6	298.89 – 274.37	Dolerite	80	50	33.596720	-5.912970	163.4	48.3	10.1	45.4	126.8	24.9	10.1	45.4
Mean*	**5/7**	**298.89 – 274.37**	**-**	**-**	**-**	**33.60**	**354.09**	**148.6**	**15.9**	**56**	**2.82**	**145.6**	**23.8**	**41.8**	**4.3**

2.8 Rock Magnetic Results

Due to the uniform rock magnetic behavior and lithology throughout the visited basins/massifs, we categorize the 55 sampled sites into four groups (Fig. 2.18). Group I encompasses 23 sites from the sedimentary basins ARG, OUR and KASS, group II summarizes the 16 siltstone sites from the Souss basin (ZIKI and ZAL) whereas the seven sampled doleritic dikes from BOUT and the nine sites from the granitic massifs of BRI and ZAE are represented by group III and IV, respectively.

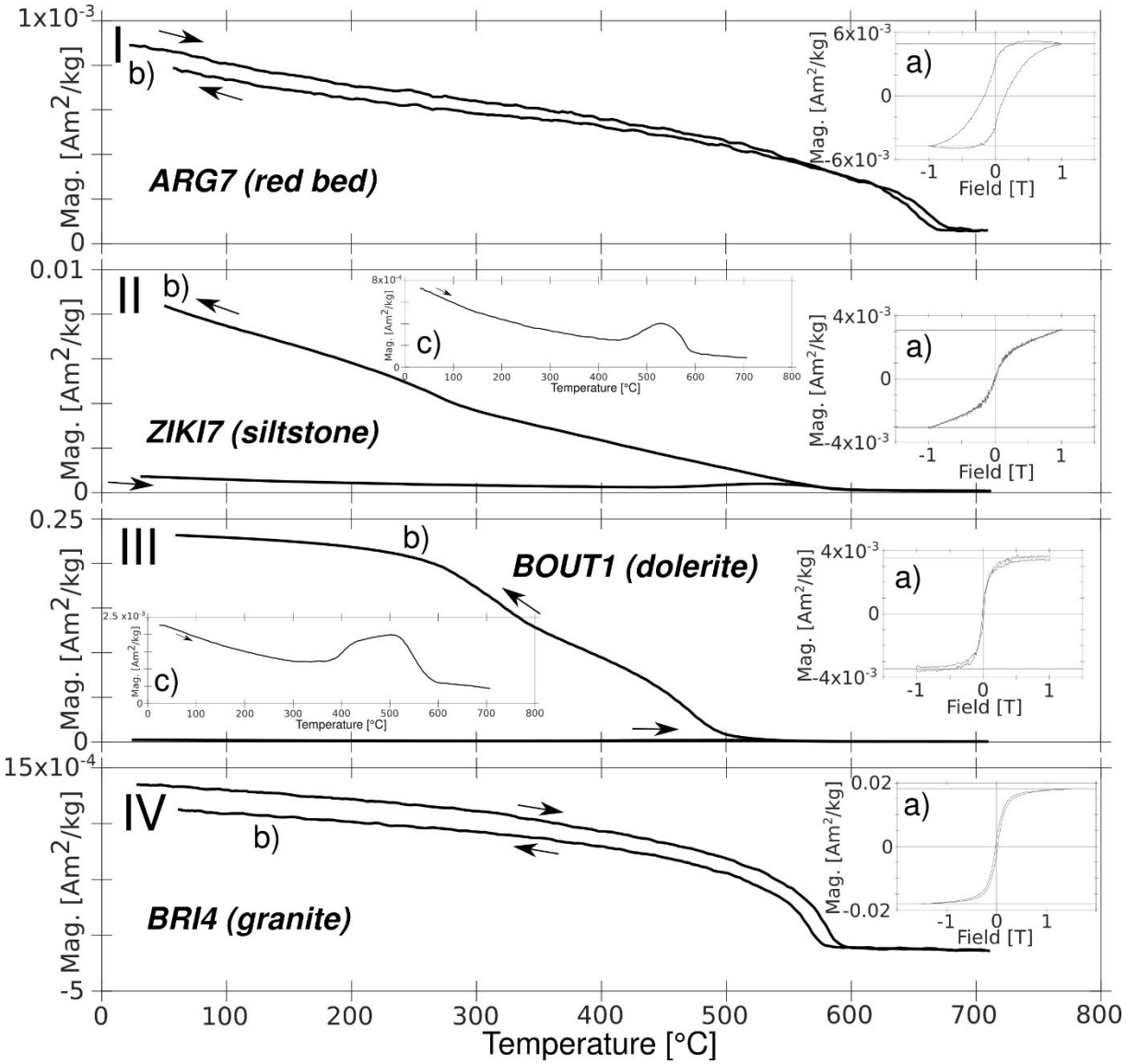

Figure 2.18: Representative rock magnetic results subdivided according to lithology, where groups I-II were derived from sedimentary samples, group III encompasses the dolerites of BOUT and group IV emanates from plutonic samples of the granitic massifs. For each category, hysteresis loops (a) and thermomagnetic curves with heating and cooling branches (b) are provided whereas the thermomagnetic curves with just the heating branches (c) are shown for those groups where magnetization upon cooling dominates the magnetic signal upon heating, which is subsequently masked in (a). Arrows specify heating and cooling cycles of thermomagnetic curves.

Within the group I, broadly shouldered hysteresis loops with high coercivities (Fig. 2.18 Ia) and reversible thermomagnetic curves with a distinct inflection around Tc ~ 660°C (Fig. 2.18 Ib) are prevalent which is diagnostic for hematite as the main mineralogical carrier of the magnetic signal for the basins of ARG, OUR and KASS. Kent et al. (2021) report similar findings for their rock-magnetic results in the Argana basin.

The siltstones of the Souss basin (group II) and the dolerite dikes of BOUT (group III) are characterized by (ill-resolved) sharp-shouldered, superparamagnetic hysteresis loops with low remanence (Fig. 2.18 IIa and IIIa). Corresponding thermomagnetic curves are irreversible with the cooling branch clearly dominating the heating branch below 560°C (Fig. 2.18 IIb, IIIb). Removing the cooling branch reveals a pronounced increase in magnetization when heating between 450°C and 530°C (Fig. 2.18 IIc), resp. 400° and 500°C (Fig. 2.18 IIIc), followed by a marked magnetization loss reaching maximal values at Tc ~ 580°C (Fig. 2.18 IIc), resp. Tc ~ 560°C (Fig. 2.18 IIIc). Since many samples were strongly weathered (e. g. dolerites, cf. chapter 2.7) and given the unblocking intervals, it is most likely that maghemite is the predominant magnetic mineral, which formed as a secondary mineral by chemical alteration processes. Due to heating beyond 530°C with associated oxidation in the laboratory oven, maghemite converts to magnetite and finally demagnetizes at its characteristic Curie temperature of Tc ~ 560 – 580°C. Upon cooling, the newly formed magnetite acquires a strong magnetization evident by the marked dominance of the cooling branches and the irreversible behavior of the thermomagnetic curves. The secondary origin of the magnetic carrier within the samples of ZIKI, ZAL and BOUT also explains associated paleomagnetic directions to be either erratic or parallel to the recent geomagnetic field (Fig. 2.7 and 2.17).

Finally, group IV representing the plutonic massifs of BRI and ZAE exhibits narrow-shouldered, PSD-shaped hysteresis loops with low coercivities (Fig. 2.18 IVa) as well as reversible thermomagnetic curves with an unblocking temperature at Tc ~ 580°C (Fig. 2.18 IVb) indicative of magnetite as the dominant magnetic mineral.

3 Anisotropy of Magnetic Susceptibility (AMS)

In order to complement the field data on the tectonic attitude of volcanic and plutonic rocks from this study and thus to better constrain the paleohorizontal, the Anisotropy of Magnetic Susceptibility (AMS; Hrouda, 1982) was measured on a pioneer set of 222 igneous samples from 35 sites stemming from eight basins (BOUA, BOUH, BOUT, CHO, KHE, MEC, NL and TID) and one plutonic massif (BRI) by means of an AGICO-KLY-2 Kappabridge (Jelinek, 1980), applying the 15 position measurement scheme of Jelinek (1977). Resulting data sets were processed using the program PmagPy from Tauxe et al. (2016).

Figure 3.1 displays the mean susceptibility k_{mean} for the nine localities studied, with conspicuous differences in magnitude. The volcanics of NL, BOUH and CHO show a strong susceptibility signal (~ 10^{-2}-10^{-4} SI units) with a pronounced variability between their respective sites (Figs. 3.1b, 3.1d-e). While the northernmost basins of TID, BOUT and BOUA are characterized by a mean susceptibility of 100-500*10^{-6} with comparable results on site-level (Figs. 3.1g-i), the weakest susceptibility (~ 20 – 200*10^{-6}) was measured at BRI, MEC and KHE with marked site-specific differences (Figs. 3.1a, 3.1c, 3.1f) suggesting to treat AMS data from these sites with caution. A greater structural trend in susceptibility (i.e., north-south gradient) is not visible.

To be able to quantify the cooling planes and thus the structural attitude of the sampled volcanics supplementing field measurements on their tectonic orientation, the magnetic fabric needs to be characterized by the shape of corresponding AMS ellipsoids, i.e. the relationship of the relative magnitudes of the maximal (k_{max}), intermediate (k_{int}) and minimal (k_{min}) eigenvalues must be determined. In case the three eigenvalues are statistically indistinct from each other ($k_{max} \approx k_{int} \approx k_{min}$), there is no anisotropy present and the shape of the ellipsoid resembles a sphere. If $k_{max} \approx k_{int} > k_{min}$, it is oblate (resembling a disc), for $k_{max} > k_{int} \approx k_{min}$ it is prolate (cigar-shaped) and for $k_{max} > k_{int} > k_{min}$, it is triaxial within confidence bounds (Tarling and Hrouda, 1993; Tauxe, 2010).

The site-specific AMS ellipsoid shapes of this study can be categorized into four groups which are completely independent of their provenance (Fig. 3.2, Table 3.1). First of all, five sites are associated with eigenvectors that plot as a blurred cloud where no preferred direction can be defined (Figs. 3.2a-b). Confidence bounds of corresponding eigenvalues are overlapping, suggesting that k_{max}, k_{int} and k_{min} are indistinguishable and no specific anisotropy of the magnetic susceptibility could be identified (Fig. 3.2c). The AMS ellipsoids are therefore

of spherical shape. Secondly, four sites are characterized by a well-defined k_{max} with k_{int} and k_{min} being strung out along a girdle perpendicular to k_{max} (Figs. 3.2d-e). Accordingly, the k_{max} distribution is separate from the statistically indistinguishable bootstrapped set of minimal and intermediate eigenvalues implying a prolate-style magnetic fabric, although the confidence bounds are quite large (Fig. 3.2f). The largest group of studied sites (14) show a tight clustering of all eigenvectors (Figs. 3.2g-h) and distinct eigenvalues at 95% confidence level (Fig. 3.2i) typical for triaxial AMS ellipsoids. Finally, twelve sites exhibit fairly well-grouped k_{min} eigenvectors whereas k_{max} and k_{int} are distributed along a great circle perpendicular to k_{min} (Figs. 3.2j-k). The minimal eigenvalue is statistically distinct from the overlapping confidence bounds of the bootstrapped intermediate and maximal eigenvalues hence indicating an oblate shape of respective AMS ellipsoids. Notably, data clustering in Fig. 3.2 does not correlate with the magnitude of the mean susceptibility (Fig. 3.1).

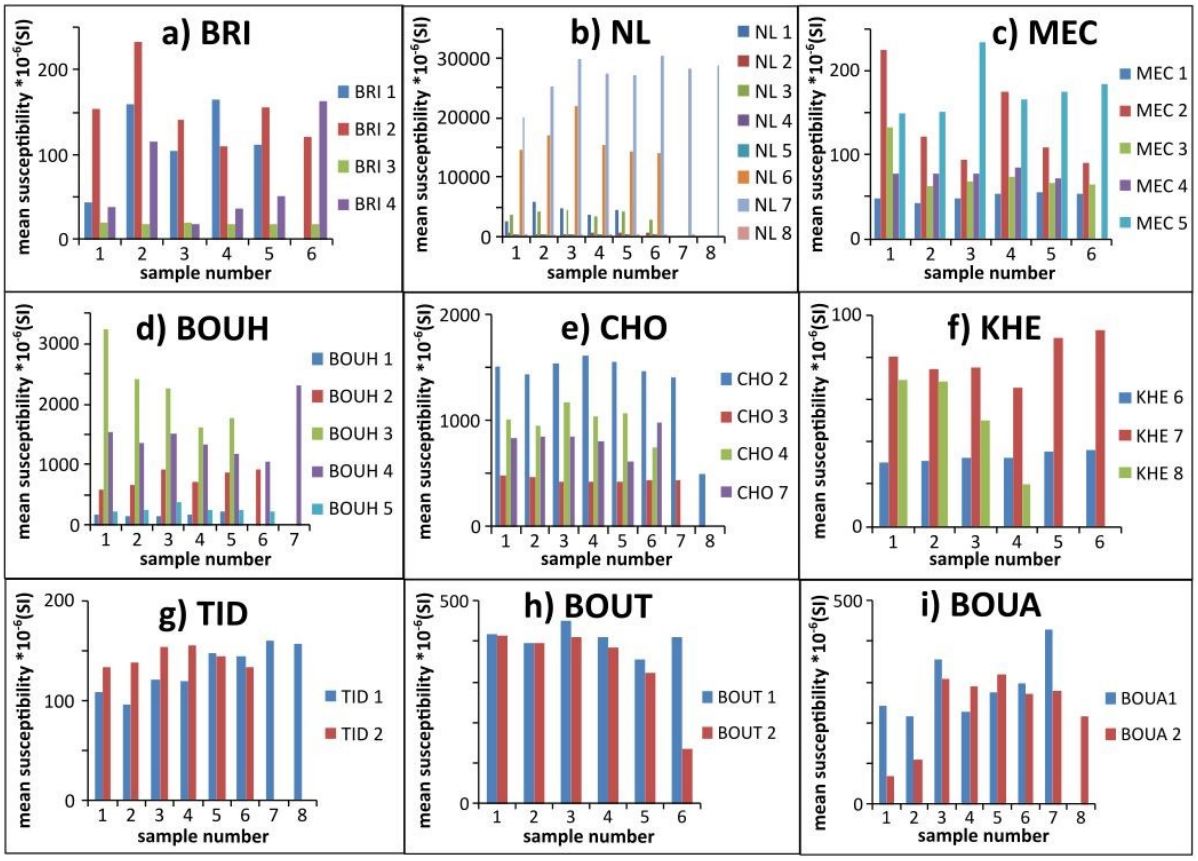

Figure 3.1: Column diagrams for studied localities sorted from south to north, where the mean susceptibility k_{mean} (in SI-units) is drawn against the number of samples taken for each site (color-coded, see legend).

A more intuitive way to visualize the shape of the AMS ellipsoids is the Jelinek (1981) diagram, where the shape factor T is plotted against the "corrected" degree of anisotropy P' (Fig. 3.3). P' values range from 1 (= 0% anisotropy, i.e., spherical) to 1.3 (= 30% anisotropy) for extreme cases (=BRI), which must be treated with caution due to the low k_{mean} value of BRI

(Fig. 3.1a). Most of the studied samples are characterized by a degree of anisotropy < 5% (mean P' value: 1.0407, i.e., 4,07% anisotropy). T ranges from 0.976 (CHO2) to -0.782 (NL3).

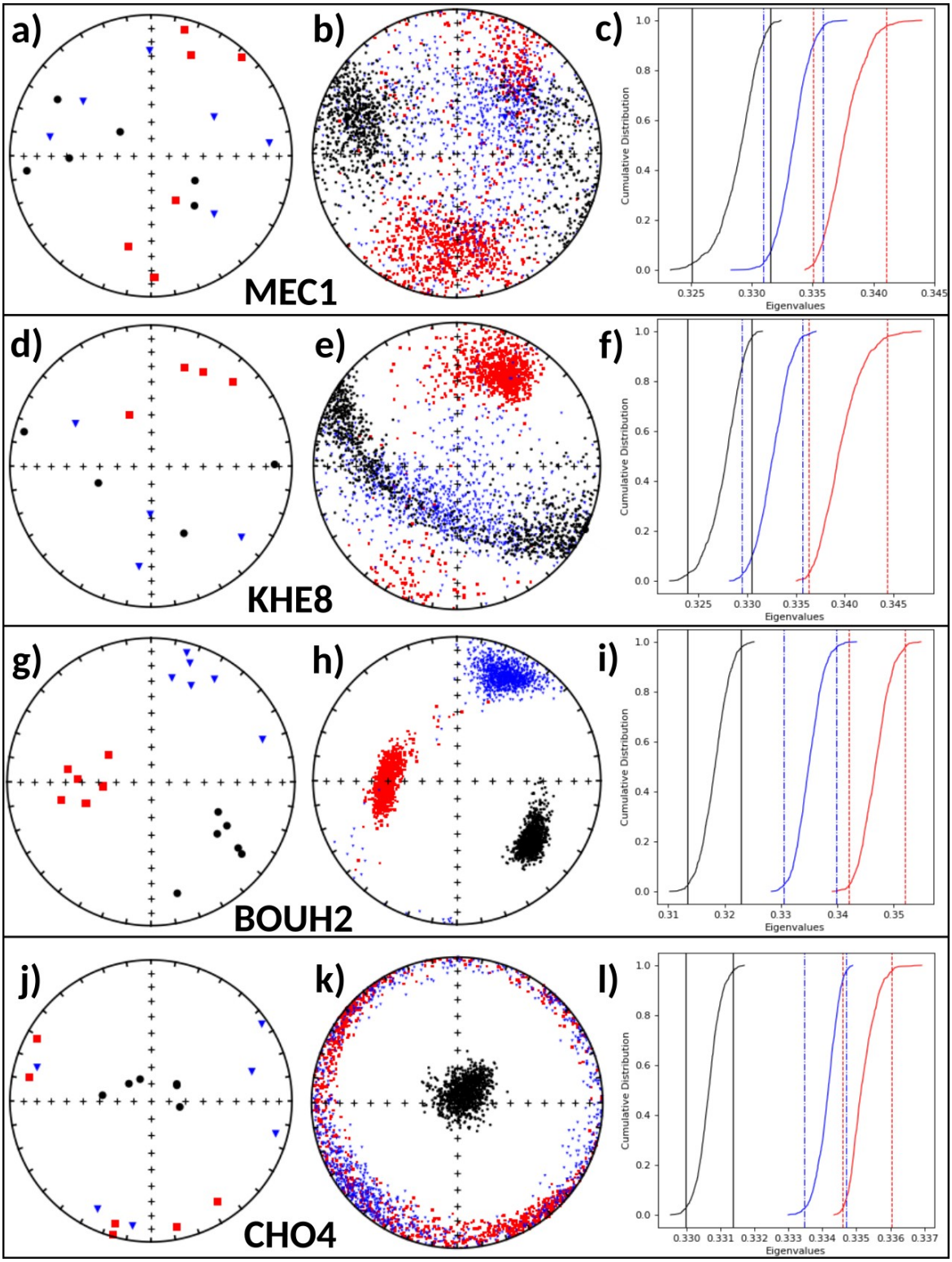

Figure 3.2: Illustration of representative site-mean AMS data of this study in geographic coordinates. Left column [(a), (d), (g), (j)]: Equal area projections of k_{max} (red squares), k_{int} (blue triangles) and k_{min} (black dots) in the lower hemisphere. Middle column [(b), (e), (h), (k)]: Parametric bootstrapped pseudo-samples of the left column. Right column [(c), (f), (i), (l)]: Cumulative distribution of the bootstrapped eigenvalues with 95% confidence bounds shown as vertical lines (color code as in left and middle column).

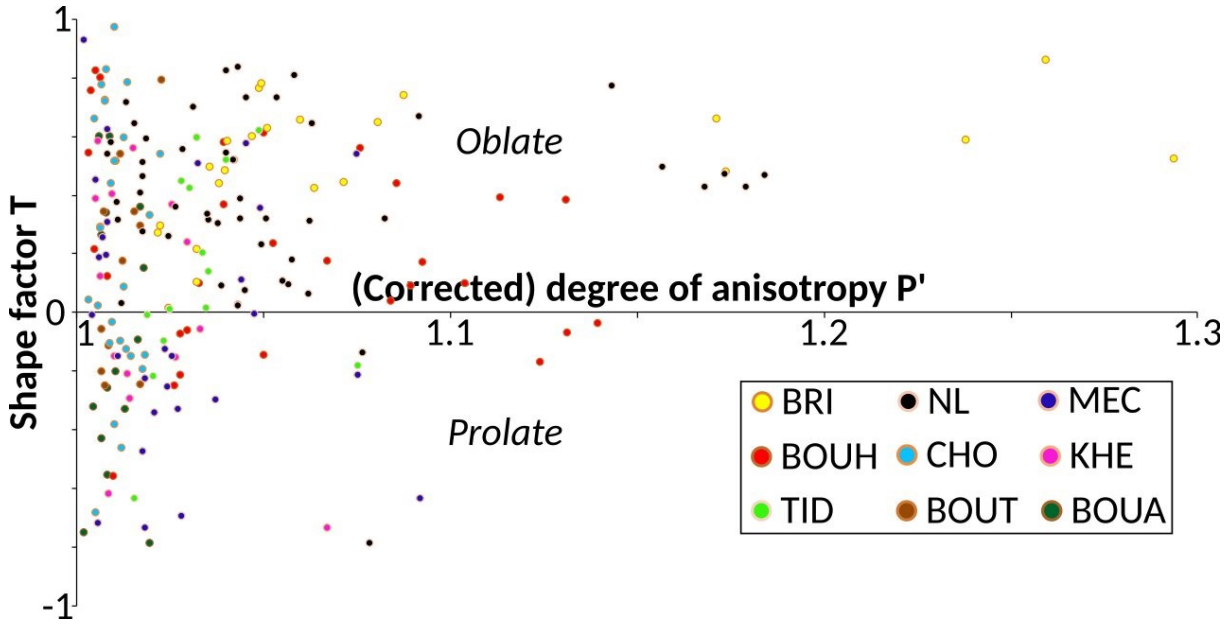

Figure 3.3: Diagram after Jelinek (1981) with the shape factor T drawn against the (corrected) degree of anisotropy P'. AMS ellipsoids with an oblate shape plot along a zone near the T axis in the range $0 < T \leq 1$ whereas prolate shapes can be found in the proximity of ordinate values of $-1 \leq T < 0$. Spherical shapes can be found around the origin, whereas the triaxial case becomes dominant in distant regions from the plot's axes. P' ranges from 1 (isotropic case) to infinity. Different color-coding for each sampled location on sample level (see inset).

As expected, a significant portion of the AMS data plots in the "oblate" part of the diagram, with increasing distances to the ordinate reflecting a stronger predominance of triaxial shapes. Domeier et al. (2021) also conducted AMS measurements on samples of NL, MEC, BOUH, KHE, TID and BOUA (their Figure 6) and documented predominantly normal oblate fabrics (e.g., KHE, MEC and NL) in rare alternation with potential inverse fabrics (e.g., their site BA1). Since k_{min} is often found perpendicular to flow surfaces within volcanic rocks with an oblate AMS ellipsoid (Butler, 1992) and we assume volcanic cooling planes to be initially horizontal, we deduce the AMS-related tectonic attitudes (dip direction and dip) by manually rotating the geographic k_{min} pole to the vertical (Table 3.1).

For the plutonic massif of BRI, mean values of the eigenvectors are associated with large errors, probably due to the weak absolute susceptibility signal k_{mean} (Fig. 3.1a). Tectonic correction derived from AMS is further deteriorating the (already ill-defined) paleomagnetic data. Furthermore, it is highly likely that – due to the size of the massif and minor tilting activity since the late Paleozoic – BRI has intruded sub-vertically and is still in situ. Thus, we prefer to assume that post-intrusional tilting is absent and do not apply the AMS derived tectonic correction (Table 2.5).

Table 3.1: *Results from site-averaged AMS measurements from this study using the AGICO-KLY-2 Kappabridge and from Domeier et al. (2021) using the more modern AGICO MFK1-FA Kappabridge (taken from their Table S2 and shown for comparison). Mean principal directions (D = Declination, I = Inclination) of the minimal (k_{min}), intermediate (k_{int}) and maximal (k_{max}) eigenvectors are calculated by applying parametric bootstrapping (Tauxe et al., 2016) on site-specific data. As a degree of uncertainty, the half-angles of corresponding Kent (1982) ellipses (ζ and η) are also provided. The resulting shape of the site-mean AMS ellipsoids is listed as their magnetic fabric. Dip Direction (Dip Dir.) and Dip represent the estimated orientation of the paleohorizontal plane as measured in the field and as a result of manual correction of k_{min} towards the vertical. Ordering of sites from south to north in accordance with Figure 3.1.*

	Mean k_{min}		Mean k_{int}		Mean k_{max}			Field measurements		AMS (k_{min})		
Site	D/I [°]	ζ/η [°]	D/I [°]	ζ/η [°]	D/I [°]	ζ/η [°]	Fabric	Dip dir. [°]	Dip [°]	Dip dir. [°]	Dip [°]	Reference
BRI1	318.9/59.6	31.6/61.0	58.8/5.8	288.2/166.8	152.2/29.7	36.2/69.3	spherical	0	0	138.9	30.4	This study
BRI2	126.2/57.8	9.4/10.7	275.7/28.5	10.4/34.1	13.3/13.8	10.8/36.9	triaxial	0	0	306.2	32.2	This study
BRI3	115.4/63.6	34.7/38.1	246.9/18.2	97.5/197.0	343.2/18.4	59.6/178.4	oblate	0	0	295.4	26.4	This study
BRI4	340.4/76.1	14.6/20.5	214.0/8.4	43.7/146.0	122.4/11.1	25.6/113.1	oblate	0	0	160.4	13.9	This study
NL1	58.5/38.3	61.5/107.0	315.1/16.3	167.6/134.4	206.7/47.2	47.7/83.8	spherical	173	45	238.5	51.7	This study
NL2	186.1/8.5	64.9/44.6	282.6/37.3	136.6/38.6	85.2/51.4	121.0/32.3	oblate	190	48	6.1	81.5	This study
NL3	234.2/40.4	17.0/9.9	53.4/49.6	16.0/18.9	143.9/0.4	96.2/-	triaxial	173	45	54.2	49.6	This study
NL4	308.5/43.1	6.6/5.2	131.2/46.9	6.8/45.6	39.8/1.3	21.3/-	triaxial	173	45	128.5	46.9	This study
NL5	162.1/22.8	33.0/17.3	351.8/66.9	30.4/39.0	253.6/3.5	351.4/53.4	triaxial	173	45	342.1	67.2	This study
NL6	234.9/82.9	15.3/15.0	125.8/2.3	72.4/306.4	35.5/6.7	50.5/210.6	oblate	245	25	54.9	7.1	This study
NL7	160.6/25.1	176.5/50.9	342.3/64.9	119.4/53.8	250.9/0.7	132.5/-	prolate	173	45	340.6	64.9	This study
NL8	82.1/62.8	7.2/12.8	210.5/17.7	14.1/56.3	307.2/20.0	8.5/54.0	triaxial	173	45	262.1	27.2	This study

NE1	57.5/42.6	9.2/3.2	303.8/23.6	11.0/5.9	193.7/38.2	9.9/6.1	oblate	261.4	31.8	237.5	47.4	Domeier et al. (2021)
NE2	356.8/50.2	11.8/4.9	145.1/35.4	12.2/4.0	246.8/15.9	6.0/3.6	oblate	166.9	37.1	-	-	Domeier et al. (2021)
NE3	331.8/17.4	13.2/8.1	230.2/32.6	34.5/12.4	85.4/51.9	34.3/8.3	oblate	154.4	65.3	-	-	Domeier et al. (2021)
MEC1	288.4/21.3	157.6/82.7	53.4/55.7	103.7/98.8	187.6/25.4	150.6/76.5	spherical	340	35	108.4	68.7	This study
MEC2	273.2/59.5	20.0/38.8	10.6/4.3	324.2/146.2	103.1/30.1	19.6/47.7	triaxial	340	35	93.2	30.5	This study
MEC3	260.9/4.3	-/149.0	166.0/48.4	132.2/64.3	354.6/41.2	145.7/52.0	oblate	245	26	80.9	85.7	This study
MEC4	346.6/74.4	28.5/38.0	209.2/11.6	138.7/219.7	117.1/10.3	79.0/184.0	oblate	355	45	166.6	15.6	This study
MEC5	297.9/26.1	21.9/12.5	63.6/50.1	26.4/20.9	192.9/27.9	26.2/12.8	triaxial	355	45	117.9	63.9	This study
MB2	99.5/31.6	32.6/9.0	3.1/10.2	32.9/12.5	257.3/56.4	17.1/6.0	oblate	295.3	47.2	-	-	Domeier et al. (2021)
MB3	127.9/23.9	9.6/5.8	296.5/65.7	21.4/4.9	36.0/4.3	20.1/5.6	oblate	321.4	35.5	307.9	66.1	Domeier et al. (2021)
MB5	208.7/25.4	72.9/27.4	107.2/22.8	72.9/17.3	340.8/54.7	29.2/13.2	spherical	310.4	41.5	-	-	Domeier et al. (2021)
BOUH1	91.8/49.6	7.4/22.6	219.0/27.3	22.3/14.8	324.4/27.3	8.9/14.5	triaxial	180	27	271.8	40.4	This study
BOUH2	129.1/33.5	9.4/18.4	24.9/20.4	25.8/19.2	269.3/49.3	9.0/24.8	triaxial	185	20	309.1	56.6	This study
BOUH3	209.9/54.9	25.9/13.2	63.9/30.2	26.8/28.0	324.2/16.2	13.1/27.5	triaxial	185	20	29.9	35.1	This study
BOUH4	296.9/8.2	269.1/108.0	69.8/78.1	103.6/97.2	205.7/8.6	247.0/101.6	spherical	185	8	116.9	81.8	This study
BOUH5	85.1/26.7	12.2/14.4	211.6/49.8	15.5/79.9	339.8/27.6	106.1/18.3	oblate	80	20	265.1	63.3	This study
TZ1	272.7/55.0	14.7/9.0	30.4/18.0	20.8/11.5	130.7/28.8	19.6/7.5	oblate	162.8	31.8	92.7	35	Domeier et al. (2021)
CHO2	123.3/60.0	13.3/15.6	261.3/23.3	17.1/66.1	359.3/17.9	17.8/76.2	triaxial	0	0	303.3	30	This study
CHO3	71.6/37.3	4.9/14.7	161.7/0.1	-/164.7	251.7/52.7	4.6/16.3	triaxial	0	0	251.6	52.7	This study

CHO4	39.0/82.8	20.9/15.2	231.3/7.1	80.5/220.1	141.1/1.5	80.7/355.3	oblate	0	0	219	7.2	This study
CHO7	132.8/54.1	106.2/52.6	297.5/34.9	146.8/116.1	32.6/7.3	264.8/125.8	spherical	350	20	312.8	35.9	This study
KHE6	213.4/26.0	60.0/38.9	73.2/57.6	58.6/100.5	312.5/18.0	162.2/49.3	oblate	5	62	33.4	64	This study
KHE7	259.5/62.1	53.2/133.9	101.2/26.2	80.3/172.6	6.8/8.9	193.6/102.7	prolate	210	52	79.5	27.9	This study
KHE8	116.4/0.2	56.5/252.2	206.8/62.8	58.8/100.7	26.3/27.2	57.1/38.2	prolate	210	52	296.4	89.8	This study
TA1	299.5/23.6	7.6/5.2	107.0/65.9	13.7/5.0	207.5/4.7	14.1/6.3	oblate	27.3	11	299.5	23.6	Domeier et al. (2021)
TG1	141.1/80.3	8.6/3.4	49.3/0.3	9.7/7.6	319.3/9.7	9.1/3.4	oblate	154	10.3	-	-	Domeier et al. (2021)
TG2	47.4/23.7	12.9/6.7	227.5/66.3	13.0/6.1	137.5/0.0	8.6/3.2	oblate	114.3	9.7	47.4	23.7	Domeier et al. (2021)
TM1	77.5/52.0	4.5/3.8	194.5/19.5	28.6/4.0	296.9/31.1	28.7/3.1	oblate	268.2	33.1	-	-	Domeier et al. (2021)
TID1	332.7/29.1	25.9/19.2	120.9/56.8	29.5/73.1	234.4/14.6	209.7/39.5	oblate	145	22	152.7	60.9	This study
TID2	84.6/11.6	41.0/37.5	177.1/12.3	175.6/48.4	312.5/73.0	32.0/117.9	oblate	145	22	264.6	78.4	This study
SA1	108.7/22.0	25.3/11.2	292.9/67.9	50.4/18.2	199.3/1.5	50.4/21.4	oblate	0	0	108.7	22	Domeier et al. (2021)
BOUT1	171.8/34.3	19.5/8.2	314.3/49.3	18.8/27.0	68.1/19.2	30.8/11.1	triaxial	17	60	351.8	55.7	This study
BOUT2	215.1/25.2	21.7/24.5	122.1/6.2	53.1/242.2	19.2/64.0	25.1/101.9	oblate	17	60	35.1	64.8	This study
BOUA1	60.7/67.6	56.2/23.7	223.4/21.4	146.6/101.2	315.8/6.0	68.9/187.7	prolate	0	0	240.7	22.4	This study
BOUA2	152.3/56.7	30.0/14.2	318.0/32.5	31.7/35.2	52.2/6.6	28.4/104.2	triaxial	0	0	332.3	33.3	This study
BA1	160.3/25.6	28.7/17.9	59.1/22.2	38.7/21.1	293.5/55.0	37.9/18.5	prolate	90	18.7	-	-	Domeier et al. (2021)
BA2	3.8/67.0	26.0/10.7	117.2/9.6	25.8/18.7	210.9/20.7	19.6/10.2	oblate	-	-	-	-	Domeier et al. (2021)

The AMS derived dip directions and dips for NL are significantly deviating from the rather uniform tectonic attitudes measured in the field. Again, reconstructing the tectonic coordinates via AMS data (which are themselves quite scattered) decreases the grouping of paleomagnetic data. Even though the results are similar for some sites (e.g., NL4), we keep the field measurements to restore the structural orientation of our sites (Table 1.4). Although the dip direction and dip pairs of Domeier et al. (2021) are much better in accordance, no significant improvement of fisher parameters was observed, which is why they also did not apply their AMS correction on the paleomagnetic data.

The same rationale holds true for MEC, BOUH and CHO. High uncertainties accompany the eigenvectors yielding bedding corrections completely unrelated to respective field measurements and displaying more steeply inclined dips, which is also observed by Domeier et al. (2021). However, applying the new AMS correction data is not improving the paleomagnetic outcome and because the field data of this work and Domeier et al. (2021) are quite similar, they are esteemed more reliable than the dip directions and dips from the AMS measurements, except for the site TZ1, where the AMS correction is applied for ameliorating the fisher parameters (Tables 1.5 - 1.7)

For KHE, the direction of eigenvectors is poorly defined compared to the results of Domeier et al. (2021), probably due to the very low absolute susceptibility (Fig. 3.1f) which cannot be as well resolved by the old AGICO-KLY-2 Kappabridge compared to the more modern AGICO MFK1-FA Kappabridge utilized by Domeier et al. (2021). Our AMS results are therefore discarded for not being reliable and we restore the paleohorizontal via observations from the field (Table 1.8).

AMS results for TID suggest strong tilting and therefore a need for a high degree of structural correction. This is in contrast with the observations in the field proposing that just moderate tectonic tilting happened. Since paleomagnetic grouping increases when using the dip directions and dips from the field (Table 1.9) and also Domeier et al. (2021) claim that the volcanics have probably not been severely tilted after emplacement, the correction using k_{min} is rejected.

For the (paleomagnetically scattered) samples of BOUT, both types of correction are quite similar with comparable outcomes. Because of the good outcrop conditions, we prefer to utilize the field data for tectonic correction (Table 2.8). Finally, fisher parameters deteriorate for BOUA when using the AMS tilt correction. Since the sampled volcanics flows were assessed to be horizontal in the field we did not apply any correction (Table 1.10).

In sum, our field data are superior for restoring the paleohorizontal compared to AMS-derived correctional data. The mostly weak susceptibility signal k_{mean} together with measuring with an outdated AGICO-KLY-2 Kappabridge not fulfilling modern laboratory standards has produced highly scattered AMS data, which need to be treated with caution. Furthermore, predominantly clear outcrop conditions and minor to moderate tilting processes since the late Paleozoic have mostly permitted to obtain a realistic understanding of the paleohorizontal in the field, which is underpinned by well-defined Fisher parameters after bedding correction at most of the localities studied. Therefore, the acquired AMS data will not be considered in this work from here on anymore.

4 Conclusions

The paleomagnetic data set acquired in the course of this work encompasses 944 samples from 152 sites from the Moroccan Meseta as well as the Western High Atlas and represents one of the biggest recent additions to the sparse late Paleozoic database for Gondwana. By providing well constrained age models for the sampled localities by means of geochronology (Table A.1), stratigraphy and paleontology (chapters 1.3, 2.1 – 2.7) this thesis lays the foundation to refine the tectonic understanding for NW Africa for the late Paleozoic and thus significantly contributes to ongoing paleogeographic debates regarding Pangea and beyond.

For the basins of ZAL, ZIKI, OUR, KASS and BOUT, paleomagnetic results rendered either erratic or are assessed to be of secondary nature (directions parallel to the present-day field). This is most likely due to either chemical alteration processes replacing the original magnetic carrier by maghemite or due to loss of the primary signal by overprinting, e.g., an IRM due to lightning strokes. Owing to difficult outcrop conditions in the field, the number of well-defined sites for the plutonic massifs ZAE and BRI were too low to draw strong conclusions from. However, the high quality of the Fisher parameters from some sites in combination with prevalence of stable rock-magnetic properties caused by magnetite provide promising starting points for further studies.

While ZAT is characterized by negative fold tests and is interpreted to be remagnetized in the late Permian, all residual basins display at least one positive outcome for one type of fold test, which in combination with matching paleolatitudes within given age models advocates a primary magnetization acquisition for JEB, MTA, NL, MEC, CHO, BOUH, KHE, TID and BOUA. Moreover, an effect of inclination shallowing can be widely excluded because all samples display paleolatitudes close to the paleoequator independent of sedimentary and igneous provenance. For the ARG basin, the negative status of the bulk fold tests needs to be treated with caution because differences within respective bedding correction field data are minor. Furthermore, basin-mean directional data from this study are statistically indistinct from the primary paleomagnetic collection (supported by a positive local fold test) of Kent et al. (2021) reinforcing their conclusion about the validity of Pangea A at around ~260 Ma and underpinning the primary character of our data from ARG. Within the basins of MTA, CHO and BOUH three reversals are also documented which can be ascribed to the late-Artinskian CI2n normal magnetochron (281.24 ± 2.3 Ma) within the Kiaman reversed superchron hence confirming the primary character of the ChRM.

The VGPs are streaked along a small NE-SW trending circle band about a rotation point in Morocco and intersect the early Permian segment of the APWP of Gondwana plotting on both sites of the APWP, with an emphasis rather to the SW suggesting mainly CW vertical axis rotations within the study area. The vertical axis rotations within the Moroccan Meseta endorse the existence of a major intra Pangea shear zone and support the validity of Pangea B as suggested by Aubele et al. (2014).

Due to the dearth of reliable late Paleozoic paleomagnetic data directly from Gondwana, Adria has repeatedly been treated as a tectonically coherent African promontory. By this, the available paleomagnetic information on Gondwana can be expanded to better contribute to ongoing controversies regarding the plate tectonic reconstruction of the assembly of Pangea, i.e., to substantiate the validity of Pangea B for the early Permian. Since the data set of this study directly stems from NW Africa (i.e. Gondwana), it is compared with a 280 Ma mean paleopole incorporating all available early Permian information of Gondwana and Adria (Channell et al., 2022). The latter is shifted ~10° towards higher values just barely beyond confidence bounds thus rendering the coherence of Adria and Gondwana questionable.

Applying our Moroccan paleopoles to state-of-the-art continental reconstruction models confirms previous Pangea A findings of Domeier et al. (2021). Accordingly, in contrast to our results on declinational variations, the paleolatitudinal results do not support Pangea B and thus do not require a large continental overlap for ~ 280 Ma. For the late Carboniferous to earliest Permian, however, the small number of sites cannot reliably address the Pangea debate.

Finally, to expand our paleogeographic understanding of the assembly of Pangea we have to ultimately decide upon the plate tectonic role of Adria and hence the legitimacy of inclusion/exclusion of paleomagnetic data from Adria in the Gondwana database. It is strongly recommended to further unravel Adria's paleogeographic past and its coherence with Gondwana, test possible models of Adria as an independent microplate and integrate this terrane in the global plate tectonic mosaic.

References

Aassoumi, H., Broutin, J., Youbi, N., El Wartiti, M. and Galtier, J., 1992. Découverte de Scleromedulloxylon cf. aveyronense, bois fossile de coniférophyte dans le complexe volcanique Permien du Bassin de Khenifra (Maroc Central). OFP Informations.

Aassoumi, H. and Vozenin-Serra, C., 1996. Sur un bois silicifie a moelle conservee du Permien du Bassin de Tiddas (Maroc Central), Mesopityoxylon tiddasense gen. et sp. nov.--Interets phylogenetique et paleoclimatique. Review of Palaeobotany and Palynology, 1(94): 57-73.

Abdelkader Benslimane, S.E.M., Saadi, M., Hilali, E.A. and Lamtahri, F., 1974. Carte Géologique et Minéralisations du couloir D'Argana - Haut Atlas Occidental (1/100000). Editions du Service Géologique du Maroc, Notes et Mémoires, N° 205.

Angoud, M., Atik, M., Benchra, M., Cherifi, A., Daimi, A., Driouiche, H., El Houari, N., El Khlifi, A., El Maoukour, A., El Mouatani, A., Essafi, M., Labriki, M., Mimet, A. and Yahyaoui, L., 2016a. Carte gèologique Du Maroc (1/50000): feuille Tahanaoute. Éditions du Service Géologique du Maroc, Notes et Mèmoires N° 446.

Angoud, M., Atik, M., Benchra, M., Cherifi, A., Daimi, A., Driouiche, H., El Houari, N., El Khlifi, A., El Maoukour, A., El Mouatani, A., Essafi, M., Labriki, M., Mimet, A. and Yahyaoui, L., 2016b. Carte gèologique Du Maroc (1/50000): feuille Arbi'a Tighadwiyn, . Éditions du Service Géologique du Maroc, Notes et Mèmoires N° 446.

Aretz, M., Herbig, H.-G., Wang, X., Gradstein, F., Agterberg, F. and Ogg, J., 2020. The carboniferous period, Geologic Time Scale 2020. Elsevier, pp. 811-874.

Arthaud, F. and Matte, P., 1977. Late Paleozoic strike-slip faulting in southern Europe and northern Africa: Result of a right-lateral shear zone between the Appalachians and the Urals. Geological society of America bulletin, 88(9): 1305-1320.

Aubele, K., Bachtadse, V., Muttoni, G., Ronchi, A. and Durand, M., 2012. A paleomagnetic study of Permian and Triassic rocks from the Toulon-Cuers Basin, SE France: Evidence for intra-Pangea block rotations in the Permian. Tectonics, 31(3).

Aubele, K., Bachtadse, V., Muttoni, G. and Ronchi, A., 2014. Paleomagnetic data from Late Paleozoic dykes of Sardinia: Evidence for block rotations and implications for the intra-Pangea megashear system. Geochemistry, Geophysics, Geosystems, 15(5): 1684-1697.

Bachtadse, V., Aubele, K., Muttoni, G., Ronchi, A., Kirscher, U. and Kent, D.V., 2018. New early Permian paleopoles from Sardinia confirm intra-Pangea mobility. Tectonophysics, 749: 21-34.

Barbero, L., Jabaloy, A., Gomez-Ortiz, D., Perez-Pena, J.V., Rodriguez-Peces, M.J., Tejero, R., Estupinan, J., Azdimousa, A., Vazquez, M. and Asebriy, L., 2011. Evidence for surface uplift of the Atlas Mountains and the surrounding peripheral plateaux: Combining apatite fission-track results and geomorphic indicators in the Western Moroccan Meseta (coastal Variscan Paleozoic basement). Tectonophysics, 502(1-2): 90-104.

Baudon, C., Fabuel-Perez, I. and Redfern, J., 2009. Structural style and evolution of a Late Triassic rift basin in the Central High Atlas, Morocco: controls on sediment deposition. Geological Journal, 44(6): 677-691.

Beauchamp, J., 1988. Triassic sedimentation and rifting in the High Atlas (Morocco), Developments in geotectonics. Elsevier, pp. 477-497.

Becker, T.P., Thomas, W.A., Samson, S.D. and Gehrels, G.E., 2005. Detrital zircon evidence of Laurentian crustal dominance in the lower Pennsylvanian deposits of the Alleghanian clastic wedge in eastern North America. Sedimentary Geology, 182(1-4): 59-86.

Belahmira, A., Hmich, D., Schneider, J., Saber, H., Lagnaoui, A. and Hminna, A., 2015. Evidence of insect-plant interaction in the Late Carboniferous Oued Issene Formation, Souss basin (Western High Atlas Mountains, Morocco). Arabian Journal of Earth Sciences, special Issue ICCI-2015, 2(3): 16-17.

Belahmira, A., Schneider, J.W., Scholze, F. and Saber, H., 2019. Phyloblattidae and Compsoblattidae (Insecta, Blattodea) from the late carboniferous Souss basin, Morocco. Journal of Paleontology, 93(5): 945-965.

Benaouiss, N., Courel, L. and Beauchamp, J., 1996. Rift-controlled fluvial/tidal transitional series in the OukaiĻmeden Sandstones, High Atlas of Marrakesh (Morocco). Sedimentary Geology, 107(1-2): 21-36.

Bensahal, A., 2001. Structure hercynienne de l'anticlinorium Khouribga-Oulmès entre Ez Zehiliga et Tiddas (Maroc central hercynien). Structure du socle ordovicien-dévonien; formation et déformation de sa couverture carbonifère: le bassin de Sidi Kassem, Thèse de doctorat, Univ. Mohammed V, Agdal, Rabat.

Biron, P.-E., 1983. Le Permo-Trias de la région de l'Ourika, Haut Atlas de Marrakech, Maroc.

Biron, P. and Courtinat, B., 1982. Contribution palynologique à la connaissance du Triasdu Haut-Atlas de Marrakech, Maroc. Geobios, 15(2): 231-235.

Boutsougame, A., Ouazzani, H., El Hadi, H. and Eddif, A., 2016. Volcanisme Permien Du Massif De Chougrane-El Had Des Bouhsoussène (Maroc Central, Maroc). European Scientific Journal, 12(27): 81-92.

Broutin, J., El Wartiti, M., Freytet, F., Heyler, D., Larhrib, M. and Morel, J., 1987. Nouvelles découvertes paléontologiques dans le bassin détritique carbonaté permien de Tiddas (Maroc central). Comptes rendus de l'Académie des sciences. Série 2, Mécanique, Physique, Chimie, Sciences de l'univers, Sciences de la Terre, 305(2): 143-148.

Broutin, J., Aassoumi, H., El Wartiti, M., Freytet, P. and Kerp, H., 1998. The Permian basins of Tiddas, Bou Achouch and Khenifra (central morocco). Biostratigraphic and palaeophytogeographic implications. Mémoires du Muséum national d'histoire naturelle (1993), 179: 257-278.

Brown, R.H., 1980. Triassic rocks of Argana Valley, southern Morocco, and their regional structural implications. AAPG Bulletin, 64(7): 988-1003.

Butler, R.F., 1992. Paleomagnetism: magnetic domains in geological terranes. Blackwell, Boston, 319-319 pp.

Cailleux, Y., Gonord, H., Le Guern, M. and Sauvage, M., 1983. Taphrogenèse et magmatisme permien dans le Maroc central.

Channell, J.E.T., Muttoni, G. and Kent, D.V., 2022. Adria in Mediterranean paleogeography, the origin of the Ionian Sea, and Permo-Triassic configurations of Pangea. Earth-Science Reviews, 230: 104045.

Charif, A., Ribeiro, M.L., Ferreira, P., Moreira, E., Ezzouhairi, H. and Ait Ayad, N., 1998. Pétrogenèse des vulcanites autuniènnes de Nzalt-Lararcha des Rehamna orientaux (Méséta centrale, Maroc).

Chopin, F., Corsini, M., Schulmann, K., El Houicha, M., Ghienne, J.F. and Edel, J.B., 2014. Tectonic evolution of the Rehamna metamorphic dome (Morocco) in the context of the Alleghanian-Variscan orogeny. Tectonics, 33(6): 1154-1177.

Cousminer, H.L. and Manspeizer, W., 1976. Triassic pollen date Moroccan High Atlas and the incipient rifting of Pangea as middle Carnian. Science, 191(4230): 943-945.

Daly, L. and Pozzi, J.P., 1976. Resultats paleomagnetiques du Permien inferieur et du Trias marocain; comparaison avec les donnees africaines et sud americaines. Earth and Planetary Science Letters, 29: 71-80.

Damotte, R., El Wartiti, M., Freytet, P., Khounch, H., Lethiers, F. and Totin-Morin, N., 1993. Le bassin de Mechraa Ben Abbou (Rehamna, maroc): son insertion dans le contexte permien du Maroc central et mésétien, 118ème Congr. nat. Soc. hist. scient., 4ème Colloque Géologie africaine, Bassins sédimentaires africains, Paris (ed. Comité Trav. Hist. Scientif.), pp. 53-72.

Delchini, S., Lahfid, A., Plunder, A. and Michard, A., 2016. Applicability of the RSCM geothermometry approach in a complex tectono-metamorphic context: The Jebilet massif case study (Variscan Belt, Morocco). Lithos, 256: 1-12.

Delchini, S., Lahfid, A., Lacroix, B., Baudin, T., Hoepffner, C., Guerrot, C., Lach, P., Saddiqi, O. and Ramboz, C., 2018. The Geological Evolution of the Variscan Jebilet Massif, Morocco, Inferred From New Structural and Geochronological Analyses. Tectonics, 37(12): 4470-4493.

Diot, H., 1989. Mise en place des granitoïdes hercyniens de la Meseta marocaine, Étude structurale des massifs de Sebt de Brikine (Rehamna), de Zaër et d'Oulmès (Massif Central) et d'Aouli-Boumia (Haute Moulouya). Implications géodynamiques, Université Paul Sabatier-Toulouse III.

Diot, H. and Bouchez, J.-L., 1991. Structure des massifs granitiques de la Méséta marocaine, marqueurs géodynamiques: Aouli-Bou-Mia (Haute Moulouya), Zaër (Massif Central) et Sebt de Brikiine (Rehamna). Géologie Méditerranéenne, 18(1): 81-97.

Doblas, M., Oyarzun, R., Lopez-Ruiz, J., Cebria, J.M., Youbi, N., Mahecha, V., Lago, M., Pocovi, A. and Cabanis, B., 1998. Permo-Carboniferous volcanism in Europe and northwest Africa: a superplume exhaust valve in the centre of Pangaea? Journal of African Earth Sciences, 26(1): 89-99.

Domeier, M., Voo, R.V.d. and Torsvik, T.H., 2012. Paleomagnetism and Pangea: The road to reconciliation. Tectonophysics, 514-517: 14-43.

Domeier, M., Font, E., Youbi, N., Davies, J., Nemkin, S., Van der Voo, R., Perrot, M., Benabbou, M., Boumehdi, M.A. and Torsvik, T.H., 2021. On the Early Permian shape of Pangea from paleomagnetism at its core. Gondwana Research, 90: 171-198.

Doubinger, J. and Roy-Dias, C., 1985. La paléoflore du Stéphanien de l'Oued zat (Haut-Atlas de Marrakech—versant nord—Maroc). Geobios, 18(5): 573-593.

Dutuit, J.-M., 1976. Découverte d'amphibiens lépospondyles dans la série inférieure de la Formation rouge d'Argana (Atlas occidental marocain). Comptes Rendus de l'Academie des Sciences, Paris(283): 1733-1734.

Dutuit, J.-M., 1988. Diplocaulus minimus n. sp.(Amphibia: Nectridea), lépospondyle de la formation d'Argana, dans l'Atlas occidental marocain. Comptes rendus de l'Académie des sciences. Série 2, Mécanique, Physique, Chimie, Sciences de l'univers, Sciences de la Terre, 307(7): 851-854.

Edel, J.B., Schulmann, K., Lexa, O. and Lardeaux, J.M., 2018. Late Palaeozoic palaeomagnetic and tectonic constraints for amalgamation of Pangea supercontinent in the European Variscan belt. Earth-science reviews, 177: 589-612.

El Hadi, H., Tahiri, A., El Maidani, A., Saddiqi, O., Simancas, F., González Lodeiro, F., Azor, A., Martinez-Poyatos, D., Tahiri, M. and De La Rosa Diaz, J., 2014. Geodynamic setting context of the Permian and Triassic volcanism in the northwestern Moroccan Meseta from petrographical and geochemical data.

El Kamel, F., 1987. Géologie du paléozoïque des Rehamna nord-orientaux, Maroc. Évolution sédimentaire et structuration hercynienne d'un bassin dévono-carbonifère. Sédimentation et déformation des molasses post-orogénique, Université Paul Cézanne-Aix-Marseille III.

El Wartiti, M., 1981. Les Terrains Permo-Carbonifères et Leur Couverture dans la Zone de Tiddas-Souk es Sebt (Bordure Nord-Ouest de la Méséta Marocaine. Nord du Maroc Central), Mohamed V Rabat, Morocco, 193 pp.

El Wartiti, M., Broutin, J. and Freytet, P., 1986. Premières découvertes paléontologiques dans les séries rouges carbonatées permiennes du bassin de Tiddas (Maroc Central). Comptes rendus de l'Académie des sciences. Série 2, Mécanique, Physique, Chimie, Sciences de l'univers, Sciences de la Terre, 303(3): 263-268.

El Wartiti, M., Jebrak, M., Cabanis, B., Toutin-Morin, N. and Youbi, N., 1992. 7ès Journèe Thèmatiques de l'Assoc. Geologues du Permien, Paris, vol. des rèsumes: p.7.

El Wartiti, M., 1993. Les Series Permiennes de Bouterhella (Maroc Central septentrional). Gaia, 6: 26-29.

El Wartiti, M., 1996. Synthèse sur le Permien du Maroc. F. Medina (éd.), Le Permien et le Trias du Maroc: état des connaissances. Editions PUMAG: 1-17.

El Wartiti, M.E., Broutin, J., Freytet, P., Larhrib, M. and Toutin-Morin, N., 1990. Continental deposits in Permian basins of the Mesetian Morocco, geodynamic history. Journal of African Earth Sciences (and the Middle East), 10(1-2): 361-368.

Elter, F.M., Gaggero, L., Mantovani, F., Pandeli, E. and Costamagna, L.G., 2020. The Atlas-East Variscan -Elbe shear system and its role in the formation of the pull-apart Late Palaeozoic basins. International Journal of Earth Sciences, 109(3): 739-760.

Enkin, R.J. and Watson, G.S., 1996. Statistical analysis of palaeomagnetic inclination data. Geophysical Journal International, 126: 495-504.

Essaifi, A. and Hibti, M., 2008. The hydrothermal system of Central Jebilet (Variscan Belt, Morocco): A genetic association between bimodal plutonism and massive sulphide deposits? Journal of African Earth Sciences, 50(2-4): 188-203.

Evans, M., Pavlov, V., Veselovsky, R. and Fetisova, A., 2014. Late Permian paleomagnetic results from the Lodève, Le Luc, and Bas-Argens Basins (southern France): Magnetostratigraphy and geomagnetic field morphology. Physics of the Earth and Planetary Interiors, 237: 18-24.

Fisher, N.I., Lewis, T. and Embleton, B.J., 1993. Statistical analysis of spherical data. Cambridge university press.

Fisher, R., 1953. Dispersion on a sphere. Proceedings of the Royal Society of London A: Mathematical, Physical and Engineering Sciences, 217(1130): 295-305.

Fluteau, F., Besse, J., Broutin, J. and Ramstein, G., 2001. The Late Permian climate. What can be inferred from climate modelling concerning Pangea scenarios and Hercynian range altitude? Palaeogeography, Palaeoclimatology, Palaeoecology, 167(1-2): 39-71.

Foner, S., 1959. Versatile and sensitive vibrating-sample magnetometer. Review of Scientific Instruments, 30: 548-557.

Gigout, M., 1951. Etudes géologiques sur la Méséta marocaine occidentale (arrière-pays de Casablanca, Mazagan et Safi). Notes et Mèmoires du Service-Géologique du Maroc, 86. Maroc Matin, Rabat.

Giuliani, G., 1982. Contribution à la géologie du massif granitique des zaër (Maroc central): Etude des minéralisations à W-Sn-Mo associés, éditeur inconnu.

Giuliani, G., Cheilletz, A. and Zimmermann, J., 1989. The emplacement, geochemistry and petrogenesis of two central Morocco Hercynian granites. Geotectonic implications. Journal of African Earth Sciences (and the Middle East), 9(3-4): 617-629.

Gordon, R.G., 1998. The plate tectonic approximation: Plate nonrigidity, diffuse plate boundaries, and global plate reconstructions. Annual Review of Earth and Planetary Sciences, 26(1): 615-642.

Gradstein, F.M., Ogg, J.G., Schmitz, M.D. and Ogg, G.M., 2020. Geologic Time Scale 2020. Elsevier.

Guiraud, R., Bosworth, W., Thierry, J. and Delplanque, A., 2005. Phanerozoic geological evolution of Northern and Central Africa: An overview. Journal of African Earth Sciences, 43(1-3): 83-143.

Hadimi, I., Ait Lahna, A., Assafar, H., Tassinari, C.C.G., Youbi, N., Boumehdi, M.A., Bensalah, M.K., Gaggero, L., Mata, J., Doblas, M., Basei, M.A.S., Sato, K., L., R.M., Charif, A., El Aarab, M., Ben Abbou, M., Zouita, F. and Khounch, H., 2018. The Post-Collisional Hercynian Volcanism of Rehamna, Western Meseta, Morocco. Mineral Chemistry, Petrology and U-Pb dating. 2eme Congres International sur le Permien et le Trias, Casablanca 25-27 aprile, 2018, Abstract book.

Hadimi, I., Youbi, N., Lahna, A.A., Bensalah, M.K., Moutbir, O., Mata, J., Doblas, M., Tassinari, C.C.G., Gaggero, L., Basei, M.A.S., Sato, K., El Moume, W. and Boumehdi, M.A., 2021. U-Pb Zircon Geochronological and Petrologic Constraints on the Post-Collisional Variscan Volcanism of the Tiddas-Souk Es-Sebt des Ait Ikko Basin (Western Meseta, Morocco). Minerals, 11(10).

Haïmeur, J., El Hassani, I.-E.E.A. and Chabane, A., 2004. Pétrologie et géochimie des granitoïdes calco-alcalins de Zaër (Maroc central): modèle pétrogénétique. Bulletin de l'Institut Scientifique, Rabat, Section Sciences de la Terre(2004): 27-48.

Henderson, C., Shen, S., Gradstein, F. and Agterberg, F., 2020. The permian period, Geologic Time Scale 2020. Elsevier, pp. 875-902.

Hmich, D., Schneider, J., Saber, H. and El Wartiti, M., 2005. Spiloblattinidae (Insecta, Blattida) from the Carboniferous of Morocco. The Nonmarine Permian: Bulletin 30, 30: 111.

Hmich, D., Schneider, J., Saber, H., Voigt, S. and El Wartiti, M., 2006. New continental Carboniferous and Permian faunas of Morocco: implications for biostratigraphy,

palaeobiogeography and palaeoclimate. Geological Society, London, Special Publications, 265(1): 297-324.

Hminna, A., Voigt, S., Saber, H., Schneider, J.W. and Hmich, D., 2012. On a moderately diverse continental ichnofauna from the Permian Ikakern Formation (Argana Basin, Western High Atlas, Morocco). Journal of African Earth Sciences, 68: 15-23.

Hoepffner, C., 1982. Le magmatisme pré-et post-orogénique hercynien dans le Paléozoïque des Rehamna. Notes du service géologique du Maroc(303): 150-163.

Hoepffner, C., Soulaimani, A. and Pique, A., 2005. The Moroccan Hercynides. Journal of African Earth Sciences, 43(1-3): 144-165.

Hoepffner, C., Houari, M.R. and Bouabdelli, M., 2006. Tectonics of the North African variscides (Morocco, Western Algeria): an outline. Comptes Rendus Geoscience, 338(1-2): 25-40.

Hounslow, M., 2006. PMagTools version 4.2-a tool for analysis of 2-D and 3-D directional data.

Hounslow, M.W. and Balabanov, Y.P., 2018. A geomagnetic polarity timescale for the Permian, calibrated to stage boundaries. In: S.G. Lucas and S.Z. Shen (Editors), Permian Timescale. Geological Society Special Publication, pp. 61-103.

Hounslow, M.W., 2022. A geomagnetic polarity timescale for the Carboniferous. Geological Society, London, Special Publications, 512(1): 141-195.

Hrouda, F., 1982. Magnetic anisotropy of rocks and its application in geology and geophysics. Geophysical Surveys, 5: 37-82.

Huvelin, P., 1977. Etude Geologique et Gitologique Du Massif Hercynien Des Jebilet (Maroc Occidental). Notes et Mèmoires du Sérvice Gèologique du Maroc, 232 bis: 307 pp.

Irving, E., 1977. Drift of Major Continental Blocks since Devonian. Nature, 270(5635): 304-309.

Irving, E. and Morel, P., 1978. Paleozoic Continental-Drift. Transactions-American Geophysical Union, 59(4): 263-263.

Irving, E., 2013. The Case for Pangea B, and the Intra-Pangean Megashear. In: J.E.T. Channell, D.V. Kent, W. Lowrie and J.G. Meert (Editors), Geophysical Monograph Series. American Geophysical Union, Washington, D. C., pp. 13-27.

Izart, A., Tahiri, A., El Boursoumi, A. and Chèvremont, P., 2001. Carte géologique Maroc (1/50000), feulle Bouqachmir. Notes et Mémoires Serv. Géol. Maroc N° 411.

Jalil, N.-E. and Dutuit, J.-M., 1996. Permian captorhinid reptiles from the Argana Formation, Morocco. Palaeontology, 39(4): 907-918.

Jalil, N.-E., 1999. Continental Permian and Triassic vertebrate localities from Algeria and Morocco and their stratigraphical correlations. Journal of African Earth Sciences, 29(1): 219-226.

Jalil, N.-E. and Janvier, P., 2005. Les pareiasaures (Amniota, Parareptilia) du Permien supérieur du Bassin d'Argana, Maroc. Geodiversitas, 27(1): 35-132.

Jebrak, M., 1985. Contribution a l'histoire naturelle des filons(F, Ba) du domaine varisque francais et marocain: essai de caracterisation structurale et geochimique des filons en extension et en decrochement, Universite d'Orleans.

Jelinek, V., 1977. The statistical theory of measuring anisotropy of magnetic susceptibility of rocks and its application. Geophyzika, Brno.

Jelinek, V., 1980. Kappabridge KLY-2. A precision laboratory bridge for measuring magnetic susceptibility of rocks (including anisotropy). Leaflet, Geofyzika Brno.

Jelinek, V., 1981. Characterization of the magnetic fabric of rocks. Tectonophysics, 79: T63--T67.

Jones, D.F., 1975. Stratigraphy, environments of deposition, petrology, age and provenance of the basal red beds of the Argana Valley, western High Atlas Mountains, Morocco, New Mexico Institute of Mining and Technology.

Kent, D.V. and Muttoni, G., 2020. Pangea B and the late paleozoic ice age. Palaeogeography, Palaeoclimatology, Palaeoecology, 553: 109753.

Kent, D.V., Olsen, P.E., Muttoni, G. and Et-Touhami, M., 2021. A Late Permian paleopole from the Ikakern Formation (Argana basin, Morocco) and the configuration of Pangea. Gondwana research, 92: 266-278.

Kent, J.T., 1982. The Fisher-Bingham distribution on the sphere. Journal of the Royal Statistical Society: Series B (Methodological), 44(1): 71-80.

Kerp, H., Broutin, J., Lausberg, S. and Aassoumi, H., 2001. Discovery of latest Carboniferous–Early Permian radially symmetrical peltaspermaceous megasporophylls from Europe

and North Africa. Comptes Rendus de l'Académie des Sciences-Series IIA-Earth and Planetary Science, 332(8): 513-519.

King, R., 1955. The remanent magnetism of artificially deposited sediments. Geophysical Supplements to the Monthly Notices of the Royal Astronomical Society, 7(3): 115-134.

Kirscher, U., Aubele, K., Muttoni, G., Ronchi, A. and Bachtadse, V., 2011. Paleomagnetism of Jurassic carbonate rocks from Sardinia: No indication of post-Jurassic internal block rotations. Journal of Geophysical Research-Solid Earth, 116.

Kirscher, U., Bilardello, D., Mikolaichuk, A. and Bachtadse, V., 2014. Correcting for inclination shallowing of early Carboniferous sedimentary rocks from Kyrgyzstan-indication of stable subtropical position of the North Tianshan Zone in the mid-late Palaeozoic. Geophysical Journal International, 198(2): 1000-1015.

Kirschvink, J.L., 1980. The least-squares line and plane and the analysis of palaeomagnetic data. Geophysical Journal of the Royal Astronomical Society, 62(3): 699-718.

Klein, H., Voigt, S., Hminna, A., Saber, H., Schneider, J. and Hmich, D., 2010. Early Triassic archosaur-dominated footprint assemblage from the Argana Basin (western High Atlas, Morocco). Ichnos, 17(3): 215-227.

Klein, H., Voigt, S., Saber, H., Schneider, J.W., Hminna, A., Fischer, J., Lagnaoui, A. and Brosig, A., 2011. First occurrence of a Middle Triassic tetrapod ichnofauna from the Argana Basin (western High Atlas, Morocco). Palaeogeography, Palaeoclimatology, Palaeoecology, 307(1-4): 218-231.

Klootwijk, C., 2023. Matching mid-to-latest Carboniferous pole path segments for eastern Australia and northern Armorica indicate a late Carboniferous Pangea-B configuration and a mid Carboniferous inertial interchange true polar wander event. Earth-Science Reviews: 104521.

Kodama, K.P., 2012. Paleomagnetism of sedimentary rocks: Process and interpretation. John Wiley & Sons.

Koymans, M., van Hinsbergen, D., Pastor-Galán, D., Vaes, B. and Langereis, C., 2020. Towards FAIR paleomagnetic data management through Paleomagnetism. org 2.0. Geochemistry, Geophysics, Geosystems, 21(2): e2019GC008838.

Koymans, M.R., Langereis, C.G., Pastor-Galán, D. and van Hinsbergen, D.J.J., 2016. Paleomagnetism.org: An online multi-platform open source environment for paleomagnetic data analysis.

Krása, D., Petersen, K. and Petersen, N., 2007. Variable field translation balance. In: D. Gubbins and E. Herrero-Bervera (Editors). Springer, Dordrecht, The Netherlands, pp. 97-99.

Lagnaoui, A., Klein, H., Voigt, S., Hminna, A., Saber, H., Schneider, J.W. and Werneburg, R., 2012. Late Triassic tetrapod-dominated ichnoassemblages from the Argana Basin (Western High Atlas, Morocco). Ichnos, 19(4): 238-253.

Lagnaoui, A., Voigt, S., Saber, H. and Schneider, J.W., 2014. First occurrence of tetrapod footprints from Westphalian strata of the Sidi Kassem Basin, Central Morocco. Ichnos, 21(4): 223-233.

Lagnaoui, A., Klein, H., Saber, H., Fekkak, A., Belahmira, A. and Schneider, J.W., 2016. New discoveries of archosaur and other tetrapod footprints from the Timezgadiouine Formation (Irohalene Member, Upper Triassic) of the Argana Basin, western High Atlas, Morocco–Ichnotaxonomic implications. Palaeogeography, Palaeoclimatology, Palaeoecology, 453: 1-9.

Lagnaoui, A., Voigt, S., Belahmira, A., Saber, H., Klein, H., Hminna, A. and Schneider, J.W., 2018. Late Carboniferous tetrapod footprints from the Souss Basin, Western High Atlas Mountains, Morocco. Ichnos, 25(2-3): 81-93.

Lanari, R., Faccenna, C., Fellin, M.G., Essaifi, A., Nahid, A., Medina, F. and Youbi, N., 2020. Tectonic Evolution of the Western High Atlas of Morocco: Oblique Convergence, Reactivation, and Transpression. Tectonics, 39(3).

Larhrib, M., 1988. Les Formations Permiennes et Triasico-Mio-Quaternaires des Régions de Tiddas, Maaziz et Sebt Aït Ikko (NW du Maroc Central). Stratigraphie, Sédimentologie et Reconstitution des Paléoenvironnements Sédimentaires, Ecole Normale Supérieure Rabat, Morocco, Rabat.

Larhrib, M., 1996. Flore fossile et séquences des formations rouges fluviatiles du bassin autunien de Tiddas-Sebt Aït Ikkou (nord-ouest du Maroc central), Le Permien et le Trias du Maroc: état des connaissances. Presses Universitaires du Maghreb, Marrakech, pp. 19-29.

Martin, D.L., Nairn, A.E.M., Noltimier, H.C., Petty, M.H. and Schmitt, T., 1978. Palaeozoic and Mesozoic palaeomagnetic results from Morocco. Tectonophysics, 44: 91-114.

Mattis, A.F., 1977. Nonmarine Triassic sedimentation, Central High Atlas Mountains, Morocco. Journal of Sedimentary Research, 47(1): 107-119.

McElhinny, M., 1964. Statistical significance of the fold test in palaeomagnetism. Geophysical Journal International, 8(3): 338-340.

Merdith, A.S., Williams, S.E., Collins, A.S., Tetley, M.G., Mulder, J.A., Blades, M.L., Young, A., Armistead, S.E., Cannon, J. and Zahirovic, S., 2021. Extending full-plate tectonic models into deep time: Linking the Neoproterozoic and the Phanerozoic. Earth-Science Reviews, 214: 103477.

Michard, A., 1976. Eléments de Géologie marocaine. Notes et Mèmoires du Sérvice Gèologique du Maroc, 252: 408 pp.

Michard, A., 1982. Le massif paléozoïque des Rehamna (Maroc) stratigraphie, tectonique et petrogenese d'un segment de la chaine varisque. Notes et Mèmoires du Sérvice Gèologique du Maroc(303): 108p.

Michard, A., Saddiqi, O., Chalouan, A. and de Lamotte, D.F., 2008. Continental Evolution: The Geology of Morocco: Structure, Stratigraphy, and Tectonics of the Africa-Atlantic-Mediterranean Triple Junction. Springer Berlin Heidelberg.

Michard, A., Ouanaimi, H., Hoepffner, C., Soulaimani, A. and Baidder, L., 2010a. Comment on Tectonic relationships of Southwest Iberia with the allochthons of Northwest Iberia and the Moroccan Variscides by JF Simancas et al. C. R. Geoscience 341 (2009) 103-113. Comptes Rendus Geoscience, 342(2): 170-174.

Michard, A., Soulaimani, A., Hoepffner, C., Ouanaimi, H., Baidder, L., Rjimati, E.C. and Saddiqi, O., 2010b. The South-Western Branch of the Variscan Belt: Evidence from Morocco. Tectonophysics, 492(1-4): 1-24.

Mitchell, R.N., Zhang, N., Salminen, J., Liu, Y., Spencer, C.J., Steinberger, B., Murphy, J.B. and Li, Z.-X., 2021. The supercontinent cycle. Nature Reviews Earth & Environment, 2(5): 358-374.

Moreau, J.-D., Benaouiss, N., Tourani, A., Steyer, J.-S., Laurin, M., Peyer, K., Béthoux, O., Aouda, A. and Jalil, N.-E., 2020. A new ichnofauna from the Permian of the Zat Valley

in the Marrakech High Atlas of Morocco. Journal of African Earth Sciences, 172: 103973.

Morel, P. and Irving, E., 1981. Paleomagnetism and the evolution of Pangea. Journal of Geophysical Research: Solid Earth, 86(B3): 1858-1872.

Morel, P., Irving, E., Daly, L. and Moussine-Pouchkine, A., 1981. Paleomagnetic results from Permian rocks of the northern Saharan craton and motions of the Moroccan Meseta and Pangea. Earth and Planetary Science Letters, 55(1): 65-74.

Mrini, Z., 1985. Âge et origine des granitoïdes hercyniens du Maroc: apport de la géochronologie et de la géochimie isotopique, Sr, Nd, Pb, Impr. UER Sci.

Mrini, Z., Rafi, A., Duthou, J.-L. and Vidal, P., 1992. Chronologie Rb-Sr des granitoides hercyniens du Maroc; consequences. Bulletin de la Société géologique de France, 163(3): 281-291.

Müller, R.D., Cannon, J., Qin, X., Watson, R.J., Gurnis, M., Williams, S., Pfaffelmoser, T., Seton, M., Russell, S.H. and Zahirovic, S., 2018. GPlates: building a virtual Earth through deep time. Geochemistry, Geophysics, Geosystems, 19(7): 2243-2261.

Muttoni, G., Kent, D.V., Garzanti, E., Brack, P., Abrahamsen, N. and Gaetani, M., 2003. Early Permian Pangea `B' to Late Permian Pangea `A'. Earth and Planetary Science Letters, 215(3-4): 379-394.

Muttoni, G., Gaetani, M., Kent, D.V., Sciunnach, D., Angiolini, L., Berra, F., Garzanti, E., Mattei, M. and Zanchi, A., 2009. Opening of the neo-Tethys Ocean and the Pangea B to Pangea A transformation during the Permian. GeoArabia (Manama), 14(4): 17-48.

Muttoni, G., Dallanave, E. and Channell, J.E.T., 2013. The drift history of Adria and Africa from 280 Ma to Present, Jurassic true polar wander, and zonal climate control on Tethyan sedimentary facies. Palaeogeography Palaeoclimatology Palaeoecology, 386: 415-435.

Muttoni, G. and Kent, D.V., 2019. Adria as promontory of Africa and its conceptual role in the Tethys Twist and Pangea B to Pangea A transformation in the Permian.

Olsen, P.E., Kent, D.V., Fowell, S.J., Schlische, R.W., Withjack, M.O. and LeTourneau, P.M., 2000. Implications of a comparison of the stratigraphy and depositional environments of the Argana (Morocco) and Fundy (Nova Scotia, Canada) Permian-Jurassic basins.

Pastor-Galán, D., 2022. From supercontinent to superplate: Late Paleozoic Pangea's inner deformation suggests it was a short-lived superplate. Earth-Science Reviews, 226: 103918.

Perez, N.D., Teixell, A., Gomez-Gras, D. and Stockli, D.F., 2019. Reconstructing Extensional Basin Architecture and Provenance in the Marrakech High Atlas of Morocco: Implications for Rift Basins and Inversion Tectonics. Tectonics, 38(5): 1584-1608.

Pohl, F., Froitzheim, N., Obermüller, G., Tomaschek, F., Schröder, O., Nagel, T.J., Sciunnach, D. and Heuser, A., 2018. Kinematics and age of syn-intrusive detachment faulting in the Southern Alps: Evidence for Early Permian crustal extension and implications for the Pangea A versus B Controversy. Tectonics, 37(10): 3668-3689.

Pruvost, P. and Termier, H., 1949. Sur Lage de la Formation Houillere De Christian (Bled Zaer, Maroc). Comptes Rendus Hebdomadaires des Seances de L Academie des Sciences, 229(1): 7-9.

Razin, P., Baudin, T., Chèvremont, P., Andries, D., Youbi, N., Hœpffner, C., Thiéblemont, D. and Chihani, E., 2003. Carte géologique du Maroc au 1/50 000, feuille de Jebel Kharrou, Mémoire explicatif. Notes et Mémoires du Service Géologique, Rabat, 436: 1-105.

Razin, P., Janjou, D., Baudin, T., Bensahal, A., Hoepffner, C., Chenakeb, M. and Cailleux, Y., 2001. Carte gèologique Du Maroc (1/50000): feuille Sidi Matla' Ech Chams. Éditions du Service Géologique du Maroc, Notes et Mèmoires N° 412.

Rochette, P. and Vandamme, D., 2001. Pangea B: an artifact of incorrect paleomagnetic assumptions?

Saber, H. and El Wartiti, M., 1996. Late Hercynian sediment and tectonic history of the Oued Zat and Ida Ou Zal basins (western high Atlas, Morocco) - Transtensive strike-slip basins. Journal of African Earth Sciences, 22(3): 301-309.

Saber, H., El Wartiti, M., Hmich, D. and Schneider, J.W., 2007. Tectonic evolution from the Hercynian shortening to the Triassic extension in the Paleozoic sediments of the Western High Atlas (Morocco). Journal of Iberian Geology, 33(1): 31-40.

Saber, H., Hminna, A., Jouhari, A. and Rmich, A., 2014. Lithostratigraphy and evidence of an extensive tectonic of Lower Permian age in the continental deposits of M'tal (Western Rehamna, Morocco). Am Int J of Res in Form Appl & Nat Sci, 7: 81-87.

Saddiqi, O., El Haimer, F.Z., Michard, A., Barbarand, J., Ruiz, G.M.H., Mansour, E.M., Leturmy, P. and de Lamotte, D., 2009. Apatite fission-track analyses on basement granites from south-western Meseta, Morocco: Paleogeographic implications and interpretation of AFT age discrepancies. Tectonophysics, 475(1): 29-37.

Saidi, A., Tahiri, A., Brahim, L.A. and Saidi, M., 2002. Etats de contraintes et mécanismes d'ouverture et de fermeture des bassins permiens du Maroc hercynien. L'exemple des bassins des Jebilet et des Rehamna. Comptes Rendus Géoscience, 334(3): 221-226.

Silantiev, V., Marchetti, L., Ronchi, A., Schirolli, P., Scholze, F. and Urazaeva, M., 2022. Permian non-marine bivalves from the Collio and GunCina formations (southern alPs, italy): revised biostratiGraPhy and PalaeobioGeoGraPhy. Rivista Italiana di Paleontologia e Stratigrafia, 128(1).

Siravo, G., Speranza, F. and Mattei, M., 2023. Paleomagnetic evidence for pre-21 Ma independent drift of South Sardinia from North Sardinia-Corsica:"Greater Iberia" vs. Europe. Tectonics: e2022TC007705.

Skikra, H., Amrouch, K., Soulaimani, A., Leprêtre, R., Ouabid, M. and Bodinier, J.-L., 2021. The intracontinental High Atlas belt: geological overview and pending questions. Arabian Journal of Geosciences, 14(12): 1071.

Tarling, D. and Hrouda, F., 1993. Magnetic anisotropy of rocks. Springer Science & Business Media, London.

Tauxe, L. and Badgley, C., 1984. Transition stratigraphy and the problem of remanence lock-in times in the Siwalik red beds. Geophysical Research Letters, 11(6): 611-613.

Tauxe, L. and Watson, G.S., 1994. The fold test: an eigen analysis approach. Earth and Planetary Science Letters, 122: 331-341.

Tauxe, L. and Kent, D.V., 2004. A simplified statistical model for the geomagnetic field and the detection of shallow bias in paleomagnetic inclinations: Was the ancient magnetic field dipolar? Timescales of the Paleomagnetic Field, 145: 101-115.

Tauxe, L., 2005. Inclination flattening and the geocentric axial dipole hypothesis. Earth and Planetary Science Letters, 233(3-4): 247-261.

Tauxe, L., 2010. Essentials of paleomagnetism. Univ of California Press.

Tauxe, L., Shaar, R., Jonestrask, L., Swanson-Hysell, N., Minnett, R., Koppers, A., Constable, C., Jarboe, N., Gaastra, K. and Fairchild, L., 2016. PmagPy: Software package for

paleomagnetic data analysis and a bridge to the Magnetics Information Consortium (MagIC) Database. Geochemistry, Geophysics, Geosystems, 17(6): 2450-2463.

Termier, H., 1936. Etudes géologiques sur le Maroc central et le moyen-Atlas septentrional, Imprimerie officielle, 743 p. pp.

Tisserant, D., 1977. Les isotopes du strontium et l'histoire hercynienne du Maroc, Étude de quelques massifs atlasiques et mésétiens, Université Louis Pasteur-Strasbourg I.

Tixeront, M., 1973. Lithostratigraphie et minéralisations cuprifères et uranifères stratiformes, syngénétiques et familières des formations détritiques permo-triasiques du couloir d'Argana, Haut Atlas occidental (Maroc). Notes & Mém. Serv. géol. Maroc, 33(249): 147-177.

Todrani, A., Zhang, B., Speranza, F. and Chen, S., 2020. Paleomagnetism of the middle Cenozoic Mula Basin (East Tibet): Evidence for km-scale crustal blocks rotated by midlower crust drag. Geochemistry, Geophysics, Geosystems, 21(9): e2020GC009225.

Torcq, F., Besse, J., Vaslet, D., Marcoux, J., Ricou, L., Halawani, M. and Basahel, M., 1997. Paleomagnetic results from Saudi Arabia and the Permo-Triassic Pangea configuration. Earth and Planetary Science Letters, 148(3-4): 553-567.

Torsvik, T., Smethurst, M. and Pesonen, L., 2015. GMAP. Geographic Mapping and Palaeoreconstruction Package, Norwegian Geological Survey Report, 90.

Torsvik, T.H., Van Der Voo, R., Preeden, U., Mac Niocaill, C., Steinberger, B., Doubrovine, P.V., Van Hinsbergen, D.J.J., Domeier, M., Gaina, C., Tohver, E., Meert, J.G., McCausland, P.J.A. and Cocks, L.R.M., 2012. Phanerozoic polar wander, palaeogeography and dynamics. Earth-Science Reviews, 114(3-4): 325-368.

Torsvik, T.H., van der Voo, R., Doubrovine, P.V., Burke, K., Steinberger, B., Ashwal, L.D., Trønnes, R.G., Webb, S.J. and Bull, A.L., 2014. Deep mantle structure as a reference frame for movements in and on the Earth. Proceedings of the National Academy of Sciences, 111(24): 8735-8740.

Tourani, A., Lund, J., Benaouiss, N. and Gaupp, R., 2000. Stratigraphy of Triassic syn-rift deposition in Western Morocco. Zentralblatt für Geologie und Paläontologie, 9(10): 1193-1215.

Vai, G.B., 2003. Development of the palaeogeography of Pangaea from Late Carboniferous to Early Permian. Palaeogeography, Palaeoclimatology, Palaeoecology, 196(1-2): 125-155.

Van der Voo, R., 1990. The reliability of paleomagnetic data. Tectonophysics, 184: 1-9.

Van der Voo, R. and Torsvik, T.H., 2001. Evidence for late Paleozoic and Mesozoic nondipole fields provides an explanation for the Pangea reconstruction problems. Earth and Planetary Science Letters, 187: 71-81.

Van Hilten, D., 1964. Evaluation of some geotectonic hypotheses by paleomagnetism. Tectonophysics, 1(1): 3-71.

Van Houten, F., 1976. Late Variscan nonmarine basin deposits, northwest Africa: Record of Hercynotype orogeny, The Continental Permain in Central, West, and South Europe. Springer, Amsterdam, pp. 215-224.

Van Houten, F.B., 1977. Triassic-Liassic deposits of Morocco and eastern North America: comparison. AAPG bulletin, 61(1): 79-99.

Visser, J.N. and Praekelt, H.E., 1998. Late Palaeozoic crustal block rotations within the Gondwana sector of Pangea. Tectonophysics, 287(1-4): 201-212.

Voigt, S., Hminna, A., Saber, H., Schneider, J.W. and Klein, H., 2010. Tetrapod footprints from the uppermost level of the Permian Ikakern Formation (Argana basin, western High Atlas, Morocco). Journal of African Earth Sciences, 57(5): 470-478.

Voigt, S., Lagnaoui, A., Hminna, A., Saber, H. and Schneider, J.W., 2011a. Revisional notes on the Permian tetrapod ichnofauna from the Tiddas Basin, central Morocco. Palaeogeography, Palaeoclimatology, Palaeoecology, 302(3-4): 474-483.

Voigt, S., Saber, H., Schneider, J.W., Hmich, D. and Hminna, A., 2011b. Late Carboniferous-Early Permian Tetrapod Ichnofauna from the Khenifra Basin, Central Morocco. Geobios, 44(4): 399-407.

Wack, M.R. and Gilder, S.A., 2012. The SushiBar: An automated system for paleomagnetic investigations. Geochemistry, Geophysics, Geosystems, 13(3).

Watson, G.S. and Enkin, R.J., 1993. The fold test in paleomagnetism as a parameter estimation problem. Geophysical Research Letters, 20(19): 2135-2137.

Werneburg, R., Schneider, J.W., Voigt, S. and Belahmira, A., 2019. First African record of micromelerpetid amphibians (Temnospondyli, Dissorophoidea). Journal of African Earth Sciences, 159: 103573.

Wernert, P., Schulmann, K., Chopin, F., Stipska, P., Bosch, D. and El Houicha, M., 2016. Tectonometamorphic evolution of an intracontinental orogeny inferred from P-T-t-d paths of the metapelites from the Rehamna massif (Morocco). Journal of Metamorphic Geology, 34(9): 917-940.

Wessel, P., Luis, J., Uieda, L., Scharroo, R., Wobbe, F., Smith, W.H. and Tian, D., 2019. The generic mapping tools version 6. Geochemistry, Geophysics, Geosystems, 20(11): 5556-5564.

Westphal, M., Montigny, R., Thuizat, R., Bardon, C., Bossert, A., Hamzeh, R. and Rolley, J., 1979. Paléomagnétisme et datation du volcanisme permien, triasique et crétacé du Maroc. Canadian Journal of Earth Sciences, 16(11): 2150-2164.

Wu, L., Kravchinsky, V.A. and Potter, D.K., 2015. PMTec: A new MATLAB toolbox for absolute plate motion reconstructions from paleomagnetism. Computers & Geosciences, 82: 139-151.

Wu, L., Murphy, J.B., Quesada, C., Li, Z.-X., Waldron, J.W., Williams, S., Pisarevsky, S. and Collins, W.J., 2021. The amalgamation of Pangea: Paleomagnetic and geological observations revisited. GSA Bulletin, 133(3-4): 625-646.

Wu, L., Pisarevsky, S., Li, Z.-X., Murphy, J.B. and Liu, Y., 2024. A new reconstruction of Phanerozoic Earth evolution: Toward a big-data approach to global paleogeography. Tectonophysics: 230198.

Youbi, N., Cabanis, B., Chalot-Prat, F. and Cailleux, Y., 1995. Histoire volcano-tectonique du massif permien de Khénifra (Sud-Est du Maroc Central). Geodinamica Acta, 8(3): 158-172.

Youbi, N., 1998. Le volcanisme «post-collisionnel»: un magmatisme intraplaque relié à des panaches mantelliques. Etude volcanologique et géochimique. Exemples d‟ application dans le Néoprotérozoïque terminal (PIII) de l‟ Anti-Atlas et le Permien du Maroc, thèse d'État, université de Marrakech.

Youbi, N., Gaggero, L., Assafar, H., Hadimi, I., Boumehdi, M., Bensalah, M.K., Linnemann, U., Gärtner, A., Mata, J. and Doblas, M., 2018. U-Pb Zircon Geochronological and Petrologic Constraints on the Post-Collisional Variscan Volcanism of the Khenifra

Basin (Western Meseta, Morocco), 2nd International Congress on Permian and Triassic Stratigraphic and Petrogenetic Implications, pp. 53-54.

Zijderveld, J.D.A., 1967. A. C. demagnetization of rocks: Analysis of results. In: D.W. Collinson, K.M. Creer and S.K. Runcorn (Editors). Elsevier, Amsterdam, pp. 254-286.

Zouicha, A., Voigt, S., Saber, H., Marchetti, L., Hminna, A., El Attari, A., Ronchi, A. and Schneider, J.W., 2021. First record of permian continental trace fossils in the jebilet massif, Morocco. Journal of African Earth Sciences, 173.

Zouicha, A., Saber, H., Attari, A.E., Zouheir, T. and Ronchi, A., 2022. Late Hercynian tectonic evolution of the Jebilet Massif (Western Meseta, Morocco) based on tectono-sedimentary analyses of related Permian continental deposits. Journal of Iberian Geology: 1-27.

Zouine, E., 1986. Evolution structurale tardi-hercynienne de la bordure NW du Maroc central entre Tiddas et Jbel Tariona, Rabat, 131 pp.

Acknowledgements

This thesis has greatly profited from the help of several persons who shall be appreciated at this point. First and foremost, I would like to express my gratitude to Prof. Dr. Valerian Bachtadse, who has introduced me to the topic in the course of my bachelor and master theses. He subsequently encouraged me to continue my work on the Pangea debate by providing me a subject of dissertation in the same field, accompanied me through the whole study and backed me up in difficult and challenging private situations during the COVID pandemic and beyond. He gave me the unique opportunity to work in beautiful places in Germany (Saar-Nahe basin and Berchtesgaden) and abroad (Italy as well as Morocco) and to present my work at internationally renowned conferences like the EGU (European Geosciences Union – General Assembly) in Vienna or the ICCP (International Congress on the Carboniferous and Permian) in Cologne.

I am also indebted to Prof. Dr. Hafid Saber, who became an integral cornerstone of the whole project by providing valuable insights into the geology of Morocco and perfectly organized the highly professional field trips as local expert of the Moroccan geology. In the course of this, the geological expertise and motivating advises of Prof. Dr. Ausonio Ronchi also need to be addressed. Thanks for pushing me when necessary. Moreover, I want to acknowledge Dr. Uwe Kirscher for his critical review and instructive improvement suggestions for this thesis. Without your initiative, the fruitful discussions and ideas during our working conclave in Ulm would not have taken place and this thesis would not be completed in this form. Of course, I also thank all my co-authors for their contribution in the significant improvement of the scientific content of this thesis, it was a pleasure and honor to work with all of you.

Moreover, fellow students Dr. Sandra Hahn and Dr. Mandana Parsi shall be thanked for their helpful advises in the process of data acquisition in the laboratory, interpretation and writing procedure as well as insightful and challenging scientific discussions in the office and beyond. Your help was truly invaluable! I furthermore want to highlight the contribution of Aileen Rinnert and Susanne Ebeling for carrying out additional measurements in the paleomagnetic laboratories of Munich and Niederlippach. In this context, the help of Lennart Krüger is also appreciated, especially his participation in the second field campaign in Morocco and his assistance upon return to the laboratory of Munich in the Sushi bar. Here, the whole magnetism group of Prof. Dr. Stuart Gilder is thanked for the scientific input at our group meeting talks and the support in the laboratory. Of course, I want to say cheers to my office

colleagues Dr. Baha Eid and Dr. Justin Tonti-Filippini, for not only providing scientific input but also a pleasant work environment and good times after work.

I also want to express my gratitude to the Deutsche Forschungsgesellschaft (DFG) for funding the whole study by the project grant BA1210/24-1 and the Chair of Geophysics for providing infrastructure and all devices necessary for completing my studies. Finally, I would particularly like to thank my parents for their emotional support who have always cheered me up in frustrating situations and have backed me up the whole time.

Appendix

***Table A.1**: Summary of published absolute geochronological age data from late Paleozoic sampling areas of Morocco.*

Sampling area/Unit	Lithology	System	Best-estimated age [Ma]	Estimate type	Reference
Nzalt-Lararcha (NL)					
Sidi Bou Yahia dome	Rhyolite	$^{206}Pb/^{238}U$ on zircon	277.07 ± 0.61	Weighted mean	Domeier et al. (2021)
Mechraa Ben Abbou (MEC)					
Douar Ouled Said Ben Ali lavas	Andesite	$^{206}Pb/^{238}U$ on zircon	284.2 ± 4.6	Concordia	Domeier et al. (2021)
Bled Mekrach dome	Rhyolite	$^{206}Pb/^{238}U$ on zircon	285.3 ± 4.9	Concordia	Hadimi et al. (2018)
Dikes intruding Paleoz. basement	Microgranite	$^{206}Pb/^{238}U$ on zircon	285.4 ± 6.1	Concordia	Razin et al. (2003)
Douar Ouled Said Ben Ali lavas	Andesite	$^{206}Pb/^{238}U$ on zircon	294.63 ± 0.67	Weighted mean	Domeier et al. (2021)
Chougrane-El Had Bouhssoussene (CHO-BOUH)					
Bir El Gassaa	Andesite	$^{40}K/^{40}Ar$ whole rock	270 ± 17	Whole rock	Van Houten (1976)
Taztot lavas	Andesite	$^{206}Pb/^{238}U$ on zircon	295.6 ± 2.9 to 267.9 ± 3.9	Range of single Zr ages	Domeier et al. (2021)
Bir El Gassaa	Andesite	$^{206}Pb/^{238}U$ on zircon	307.8 ± 4 to 295.5 ± 3.4	Range of single Zr ages	Domeier et al. (2021)
Khenifra (KHE)					
Jbel Bou Hayati	Rhyolitic breccia	$^{40}K/^{40}Ar$ whole rock	264 ± 10	Whole rock	Jebrak (1985)
Upper Talat Mechtal lavas	Dacite	$^{206}Pb/^{238}U$ on zircon	280.3 ± 2.1	Concordia	Youbi et al. (2018)
Takarout intrusive neck	Andesite	$^{206}Pb/^{238}U$ on zircon	282.76 ± 2.19	Weighted mean	Domeier et al. (2021)
Sidi Tiri lavas	Hybrid lava	$^{206}Pb/^{238}U$ on zircon	287.9 ± 3.8	Concordia	Youbi et al. (2018)
Sidi Tiri lavas	Rhyolite	$^{206}Pb/^{238}U$ on zircon	290.3 ± 2.1	Concordia	Youbi et al. (2018)
Sidi Tiri pyroclastic fall	Pyroclastic fall	$^{206}Pb/^{238}U$ on zircon	290.6 ± 2.6	Concordia	Youbi et al. (2018)
Lower Taghat lavas	Dacite	$^{206}Pb/^{238}U$ on zircon	295.1 ± 2.9	Concordia	Youbi et al. (2018)
Talat Mechtal lavas	Andesite	$^{206}Pb/^{238}U$ on zircon	305.59 ± 2.68	Weighted mean	Domeier et al. (2021)
Tiddas (TID)					
Ari el Mahsar dome	Rhyolite	$^{206}Pb/^{238}U$ on zircon	286.4 ± 4.7	Concordia	Hadimi et al. (2021)
Bou Achouch (BOUA)					
Bou Achouch lava	Andesite	$^{206}Pb/^{238}U$ on zircon	301.50 ± 1.24	Weighted mean	Domeier et al. (2021)
Ourika (OUR)					
F1 formation	Conglomerate	$^{206}Pb/^{238}U$ on zircon	257.7 ± 1.7	Weighted mean	Perez et al. (2019)
F2 formation	Arkosic litharenite	$^{206}Pb/^{238}U$ on zircon	266.3 ± 3.9	Single Zr age	Perez et al. (2019)

Sebt Brikiyne (BRI)					
BRI massif	Granite	$^{87}Rb/^{87}Sr$ whole rock	268 ± 6	Whole rock	Mrini et al. (1992)
BRI massif	Granite	$^{40}Ar/^{39}Ar$ on biotite	274.8 ± 5.4	Single Bt age	Chopin et al. (2014)
BRI massif	Granite	$^{87}Rb/^{87}Sr$ whole rock	278 ± 2	Whole rock	Tisserant (1977)
Zaer (ZAE)					
ZAE massif	Granite	$^{87}Rb/^{87}Sr$ whole rock	279 ± 11	Whole rock	Mrini et al. (1992)
ZAE massif	Granite	$^{87}Rb/^{87}Sr$ whole rock	284 ± 15	Weighted mean	Haïmeur et al. (2004)
ZAE massif	Granite	$^{87}Rb/^{87}Sr$ whole rock	298 ± 3	Weighted mean	Haïmeur et al. (2004)
ZAE massif	Granite	$^{87}Rb/^{87}Sr$ whole rock	303 ± 13	Whole rock	Mrini et al. (1992)